AD-773 836

MULTIAXIAL RESPONSE OF ATJ-S GRAPHITE

Julius Jortner

McDonnell Douglas Astronautics Company

Prepared for:

Air Force Materials Laboratory

October 1973

DISCLAIMER NOTICE

THIS DOCUMENT IS BEST QUALITY PRACTICABLE. THE COPY FURNISHED TO DTIC CONTAINED A SIGNIFICANT NUMBER OF PAGES WHICH DO NOT REPRODUCE LEGIBLY.

NOTICE

When Government drawings, specifications, or other data are used for any
purpose other than in connection with a definitely related Government
procurement operation, the United States Government thereby incurs no
responsibility nor any obligation whatsoever; and the fact that the
government may have formulated, furnished, or in any way supplied the said
drawings, specifications, or other data, is not to be regarded by implication
or otherwise as in any manner licensing the holder or any other person
or corporation, or conveying any rights or permission to manufacture, use,
or sell any patented invention that may in any way be related thereto.

Copies of this report should not be returned unless return is required by
security considerations, contractual obligations, or notice on a specific
document.

MULTIAXIAL RESPONSE OF ATJ-S GRAPHITE

J. Jortner

McDonnell Douglas Astronautics Company

TECHNICAL REPORT AFML-TR-73-170

OCTOBER 1973

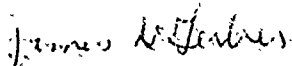Approved for Public Release; Distribution Unlimited

i d

JAMES D. GERBER, CAPT, USAF
Chief, Space & Missiles Branch
Systems Support Division
AF Materials Laboratory

ii

ABSTRACT

Experiments to explore the fracture and deformation of ATJ-S graphite under
multiaxial stresses are described. The program was a continuation to previous
efforts reported in AFML-TR-71-253. The program included additional fracture
tests in biaxial tension at 2000°F; an analytical evaluation of the applica-
bility and limitations of biaxial test data; tests at room temperature under
triaxial stress states to measure the effects of multiaxiality on strain; and
some biaxial experiments at room temperature to further explore the nature of
"biaxial softening" (the occurrence of unexpectedly large strains in biaxial
tension). The 2000°F fracture data suggest that biaxiality in tension causes
a relatively greater decrease of stress at failure at 2000°F than at room
temperature; however the results are clouded by the possibility that a defec-
tive billet was used in the tests. Based on analyses of stress and strain
gradients in the biaxial specimen, fracture data from the previous efforts
has been reviewed and revised summary plots of biaxial fracture stresses and
strains at 70°F and 2000°F are presented. The triaxial deformation tests
suggest that an ellipsoidal yield function and a "non-associated" flow rule
describe the measured strain responses of ATJ-S graphite better than some
alternate approaches. The triaxial data also illustrate the potentially
large effects that stress history (load-path) can have on strain. The biaxial
softening experiments demonstrate the existence of a negative incremental
Poisson's ratio in biaxial tension.

TABLE OF CONTENTS

Preceding page blank

LIST OF ILLUSTRATIONS

AD 773 836

DOCUMENT CONTROL DATA - R & D

(Security classification of title, body of abstract and indexing annotation must be entered when the overall report is classified)

1. ORIGINATING ACTIVITY (Corporate author)	2a. REPORT SECURITY CLASSIFICATION
McDonnell Douglas Astronautics Company Huntington Beach, California 92647	Unclassified
	2b. GROUP

3. REPORT TITLE

MULTIAXIAL RESPONSE OF ATJ-S GRAPHITE

4. DESCRIPTIVE NOTES (Type of report and inclusive dates)

Final Report - 1 July 1972 - 15 May 1973

5. AUTHOR(S) (First name, middle initial, last name)

Julius Jortner

6. REPORT DATE	7a. TOTAL NO. OF PAGES	7b. NO. OF REFS
October 1973	124	29

8a. CONTRACT OR GRANT NO.	9a. ORIGINATOR'S REPORT NUMBER(S)
F33615-72-C-2047	MDC G3581
b. PROJECT NO. 7381	
c. Task No. 738102	9b. OTHER REPORT NO(S) (Any other numbers that may be assigned this report)
d.	AFML-TR-73-170

10. DISTRIBUTION STATEMENT

Approved for Public Release: Distribution Unlimited.

11. SUPPLEMENTARY NOTES	12. SPONSORING MILITARY ACTIVITY
	Air Force Materials Laboratory Wright-Patterson Air Force Base, Ohio 45433

13. ABSTRACT

Experiments to explore the fracture and deformation of ATJ-S graphite under multiaxial stresses are described. The program was a continuation to previous efforts reported in AFML-TR-71-253. The program included additional fracture tests in biaxial tension at 2000°F; an analytical evaluation of the applicability and limitations of biaxial test data; tests at room temperature under triaxial stress states to measure the effects of multiaxiality on strain; and some biaxial experiments at room temperature to further explore the nature of "biaxial softening" (the occurrence of unexpectedly large strains in biaxial tension). The 2000°F fracture data suggest that biaxiality in tension causes a relatively greater decrease in stress at failure at 2000°F than at room temperature; however the results are clouded by the possibility that a defective billet was used in the tests. Based on analyses of stress and strain gradients in the biaxial specimen, fracture data from the previous efforts has been reviewed and revised summary plots of biaxial fracture stresses and strains at 70°F and 2000°F are presented. The triaxial deformation tests suggest that an ellipsoidal yield function and a "non-associated" flow rule describe the measured strain response of ATJ-S graphite better than some alternate approaches. The triaxial data also illustrate the potentially large effects that stress history (load-path) can have on strain. The biaxial softening experiments demonstrate the existence of a negative incremental Poisson's ratio in biaxial tension.

DD FORM 1473 1 NOV 65

1a

14. KEY WORDS	LINK A		LINK B		LINK C	
	ROLE	WT	ROLE	WT	ROLE	WT
Graphite						
ATJ-S Graphite						
Mechanical Behavior						
Multiaxial Stress						
Biaxial Stress						
Triaxial Stress						
Constitutive Relations						
Stress-Strain Response						

LIST OF TABLES

LIST OF SYMBOLS

Symbols Frequently Used

A .... cross-sectional area

a .... depth of flaw, in fracture mechanics calculations

a- and b- axis .... with-grain directions

c-axis .... across-grain direction

E .... Young's Modulus

e .... strain

$\bar{e}$ .... effective strain

K .... correction factor

K_t .... transverse sensitivity factor of strain gage

K_{IC} .... fracture toughness

L .... load applied to a specimen by means other than pressure

M_1 .... front-face magnification factor

M_2 .... back-face magnification factor

P .... pressure

r .... radius

t .... thickness of specimen wall

W .... work

ν .... Poisson's Ratio

ν_{ij} .... Poisson's Ratio, (first subscript refers to uniaxial load direction; second subscript refers to transverse strain direction).

σ .... stress

$\bar{\sigma}$ .... effective stress

Subscripts

A .... axial, along axis of cylindrical specimen

a, b .... with-grain

B or N .... referring to nickel bladder

c .... across-grain

H .... hoop, along hoop (circumferential) direction of cylindrical specimen

Subscripts (Cont'd)

i .... internal to hollow cylinder

i,j .... dummy indices, representing stress or strain directions

m .... mean value, or value calculated from thin-wall cylinder theory

o .... external to hollow cylinder

R .... radial, along radial direction in cylindrical specimen

1,2,3 .... principal stress directions

Superscripts

E .... elastic

P .... plastic

Section 1
INTRODUCTION

The rational design of all but the simplest thermostructurall -loaded graphite components requires a knowledge of the material's response to multiaxial stress states. Minimal requirements include a constitutive law relating stresses to strains and a fracture criterion.

The work described in this report is a continuation of previous efforts (References 1, 2, 3 and 4) to explore the deformation and fracture of ATJ-S graphite under multiaxial stress states. The main objectives of the current work were to:

A. Obtain additional fracture data in biaxial tension at 2000°F

B. Analyze the limitations of the biaxial test technique, which makes use of a thin-wall tubular specimen subjected to axial load and internal pressure, as an aid to interpreting the biaxial data obtained

C. Plan and conduct experiments at room temperature under biaxial and triaxial stress-states, to help define improved constitutive laws for use in stress analysis of graphite components.

Section 2
MATERIAL

Two billets of ATJ-S graphite, designated as numbers 12S1-3 and 21R1-6 by the manufacturer (the Union Carbide Corporation), were used in this program. Billet 12S1-3 was used for deformation studies (Sections 5 and 6). Billet 21R1-6 was used for the 2000°F biaxial fracture tests (Section 4).

The billets were selected from a normal product run of "cored" (special-process or WS-type) ATJ-S to have overall bulk densities between 1.85 and 1.86 g/cc. When received, the overall dimensions were measured, the overall bulk density was checked by comparing the weight in air to the weight immersed in water, and ultrasonic velocities were measured through the billet in the radial and axial directions. The results of these measurements are given in Table I.

The billets were inspected by X-ray radiography. Three shots were taken radially, 120 degrees apart. The radiographs showed no anomalies apart from the density gradients typical of this grade of graphite (see Reference 5, for example). That is, the material within about one inch of ends of the billet was discernibly denser than the remainder of the billet.

Ultrasonic pulse-echo inspection, recorded by C-scan, was also carried out. The ultrasonic beam was directed radially and the parameters were adjusted, with the aid of an ATJ-S test standard, to detect flat-bottom holes 1/32-inch in diameter. A few pulse-echo indications were found in each billet. However it was possible to excise the mechanical test specimens so that none of the detected pulse-echo anomalies were included in the gage sections.

Drawings showing the location of specimens within the two billets are presented in Figures 1 and 2. Figure 3 shows how solid cores were taken from the large

TABLE I

BILLET CHARACTERISTICS

| ATJ-s Billet No. | Approximate Dimensions, Inches | | | | Bulk Density g/cc | Acoustic Velocities, in/microsec | |
	Length	Outside Diameter	Hole Diameter	Hole Depth		Axial	Radial
12S1-3	10-5/8	7-1/4	2-1/2	6-1/4	1.86	0.0865 - 0.0871	0.1016 - 0.1032
21R1-6	10-1/2	7-1/4	2-1/2	6-1/4	1.85	0.0849 - 0.0861	0.1004 - 0.1032

NOTES: (1) Bulk Density from weight and volume; volume measured by immersion in water after applying waterproof vinyl coating (approximate thickness = 0.002 inch).

(2) Acoustic Velocities at 1 MHz. Axial Velocities measured at 5 inch diameter circle, six measurements. Radial Velocities measured at 2 inch intervals along length at six angular positions.

4
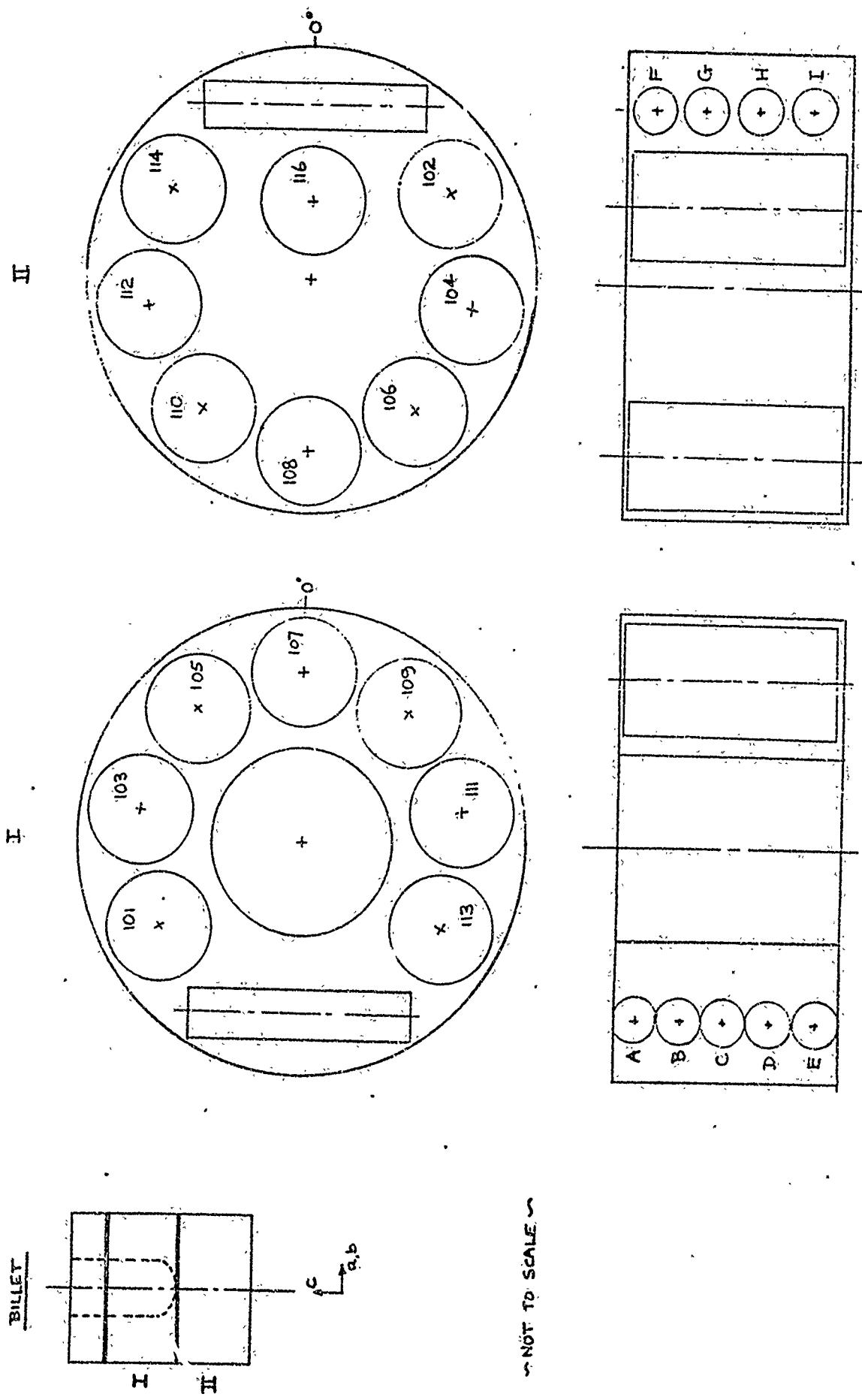
Figure 1. Sectioning Plan for Billet 21R1-6
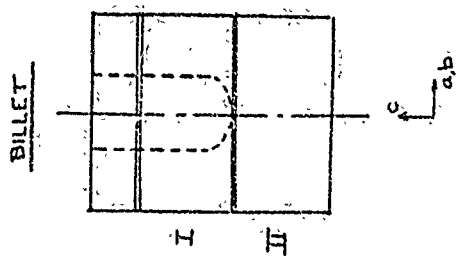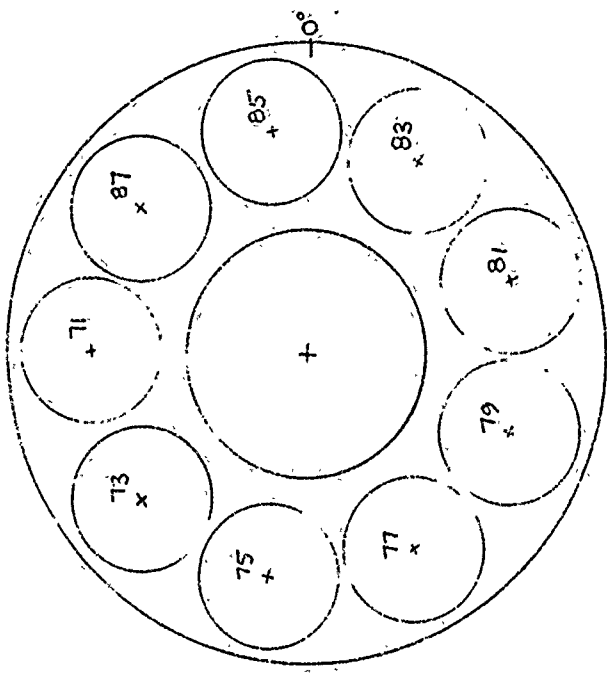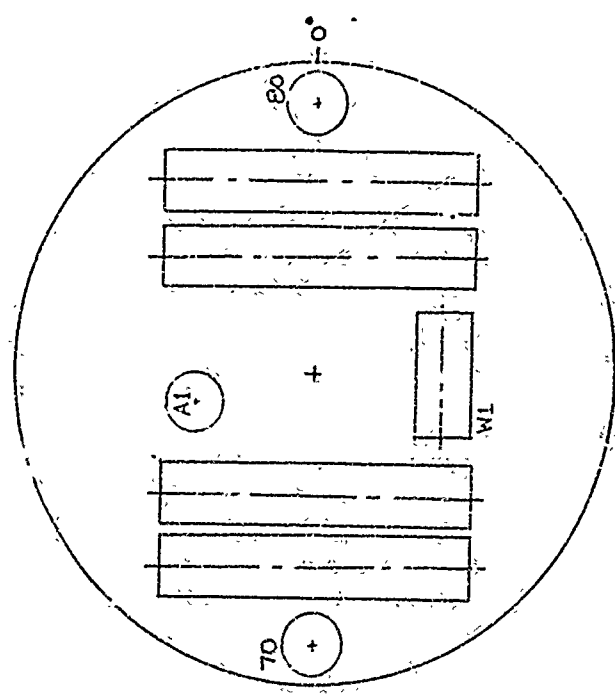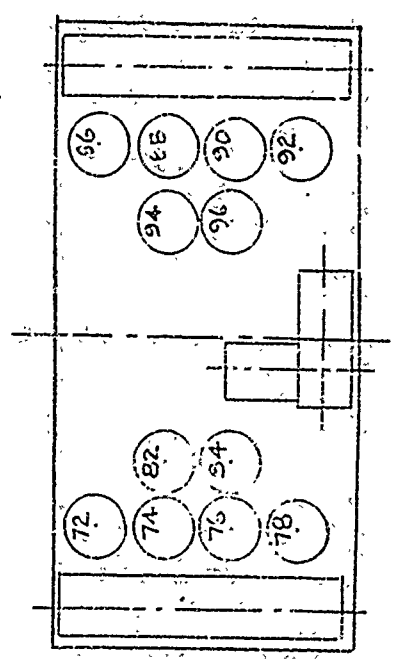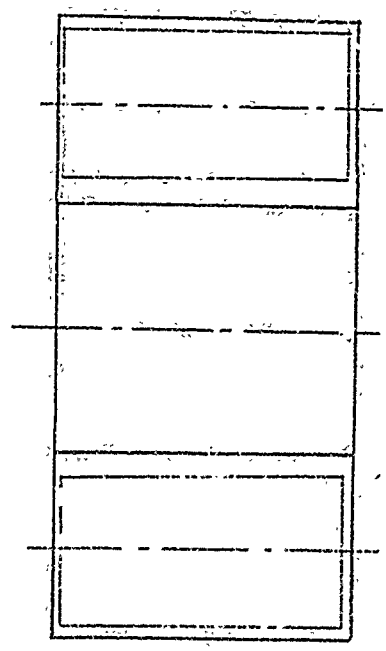
Figure 2. Sectioning Plan for Billet 12S1-3

6

PARENT BILLET

HOLLOW BLANK FOR BIAXIAL TEST

SOLID CORE (ACROSS-GRAIN)

WITH-GRAIN BLANK
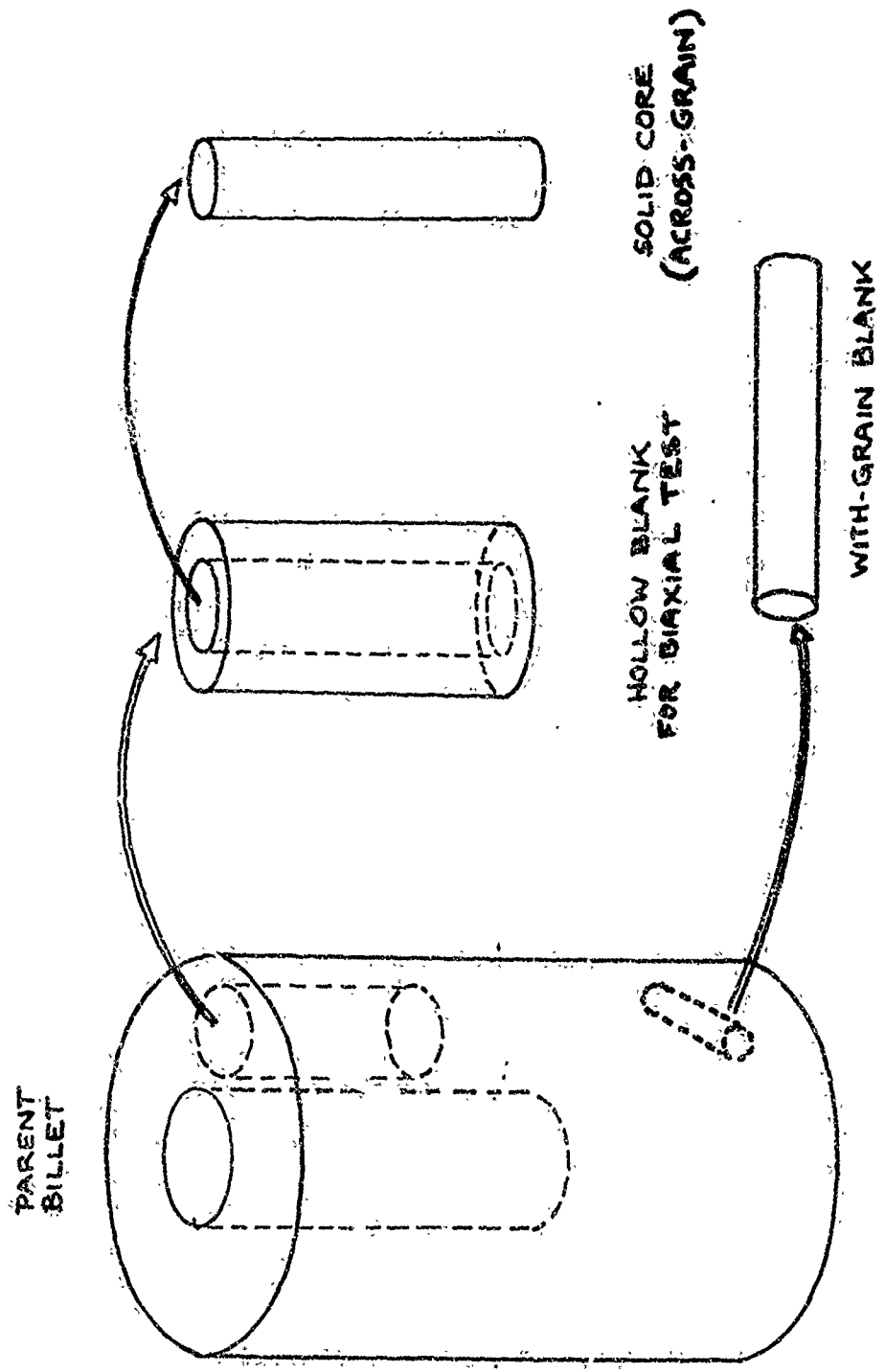
Figure 3. Typical Specimen Blanks

cylindrical blanks used for making biaxial specimens. The solid specimen blanks, including biaxial specimen cores, were subjected to bulk density and ultrasonic velocity measurements. The results are summarized in Table II.

TABLE II

BILLET CHARACTERIZATION (SPECIMEN BLANK DATA)

ATJ-S Billet Number	Bulk Density g/cc	Acoustic Velocity in/microsec	
		Across Grain	With Grain
12S1-3	1.84 – 1.86	0.086 – 0.088	0.102 – 0.103
21R1-6	1.84 – 1.85	0.084 – 0.086	0.102 – 0.104

NOTES: (1) Density by dry weight and measured volume.

(2) Acoustic velocity measured at 1 MHz.

9

Section 3

EVALUATION OF THE BIAXIAL TEST

The immediate motivation for evaluating the biaxial test (as conducted at
MDAC to provide the data reported in References 1, 2, 3 and 4) was to explain
the apparent discrepancy between the uniaxial tensile strengths measured with
biaxial specimens and the strengths measured with standard uniaxial specimens.
The discussion also is intended to provide some insight into the experimental
difficulties associated with biaxial testing and outline the limitations of
the data obtained. The biaxial techniques are described in Section 3.1; the
stress and strain gradients existing in the biaxial specimens are discussed
in Section 3.2; and uniaxial techniques are described in Section 3.3. The
discrepancies between results from the two types of specimens are discussed
in Section 3.4; and the implications are summarized in Section 3.5.

3.1 BIAXIAL TEST TECHNIQUES

The biaxial test methods employed at McDonnell Douglas have been described in
References 1, 2 and 6. Biaxial stresses are obtained by combining axial load
with internal pressure applied to a hollow cylindrical specimen. The biaxial
specimen design shown in Figure 4 has been used in the tests reported in
References 2, 3 and 4 and in the study reported here. The specimen used in
Reference 1 was similar in diametral measurements but was shorter (3.15-inch
overall length, 0.8-inch gage length).

All specimens were inspected, using standard machine shop practice, for
conformity to the dimensional tolerances shown in Figure 4. Prior to testing,
the wall thickness was measured directly using a special micrometer gage set
set-up (Figure 5), rather than by taking the difference between outer and
inner diameters, because it was found that the action of a three-point
inner-diameter micrometer could deform the specimen wall enough to cause
error   Actual wall thicknesses have varied between 0.047 to 0.051 inches
from specimen to specimen.

Figure 4. Biaxial Specimen Design

NOTES

1. UNSPECIFIED TOLERANCES ±0.010

2. UNSPECIFIED SURFACE FINISH 16

12
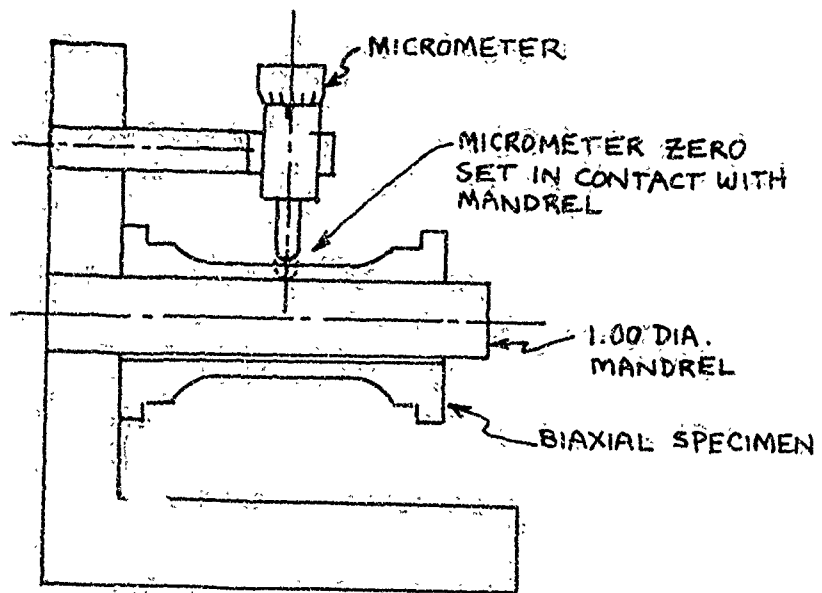
Figure 5. Wall-Thickness Measurement Technique

A potential source of error in the strength calculations is the difficulty of precisely measuring the wall thickness of the biaxial specimen. A recent check on the pretest measurements, by direct micrometer measurements of the fragments from fractured specimens, showed that the gage technique of Figure 5 sometimes overestimates the wall thickness by approximately 0.0005 to 0.0010 inches. The data reduction in the current study was based on direct measurements of the fractured fragments from the gage section of each specimen. In prior efforts, (References 1 through 4), however, the pretest measurements were used.

The exterior surface of the gage section of each specimen was inspected visually after being wiped with alcohol. A fair number of small pits and, in some cases, machining marks on some specimens were discovered in this manner. However, there appears to be no correlation between fracture initiation sites and the location of these marks. The lack of correlation may be due to the existence of more severe defects at the inner-diameter surface (which was not as well inspected because of its relative inaccessibility) or may imply that such surface pits are not as effective as other types of defects in reducing strength.

The axial loads are applied in a "rigid" fixture (Figure 6) designed to limit bending strains in the specimen. Alignment checks performed before each series of tests show that the bending strains introduced into the biaxial specimen are less than 3 percent of the average axial strain at fracture both in tensile and compressive loading.

Friction between the load rods and their guide bushings causes the measured load (top load cell) to be less than the actual axial load acting on the specimens. The measured load was used, without correction, in the data reduction (Section 3.1.1). The resulting error in axial stress is estimated at less than 1.5 percent, based on direct measurements of the friction both at room and elevated temperature.
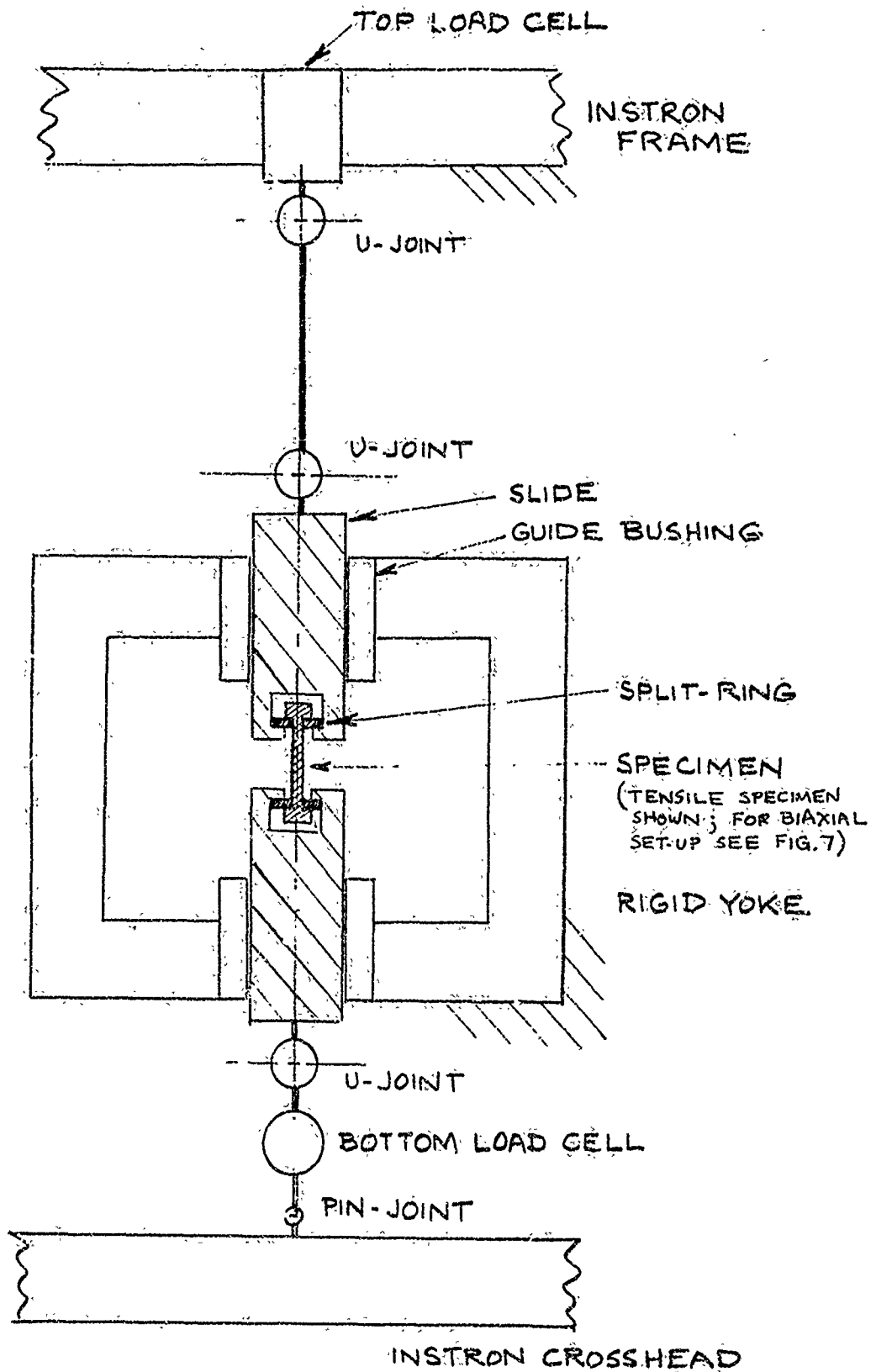
Figure 6. Rigid Alignment Fixture
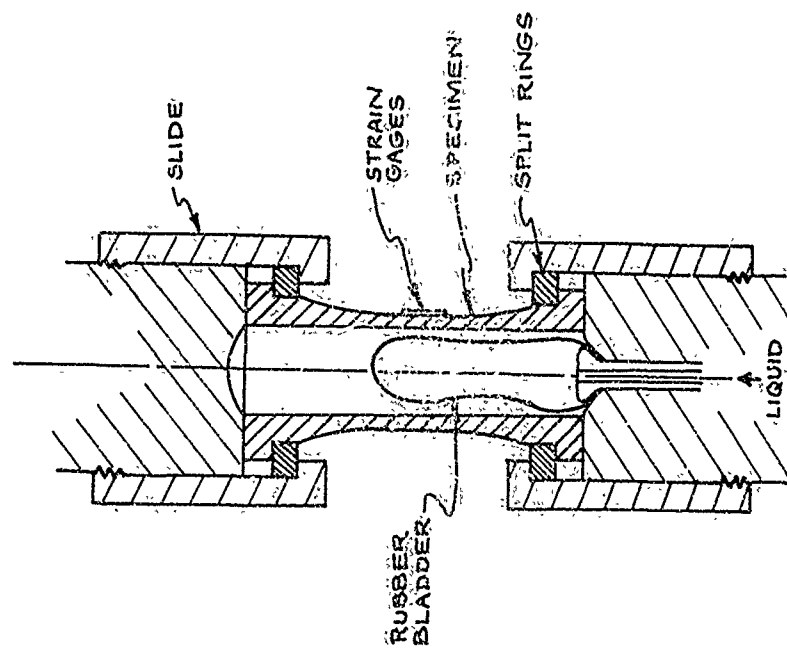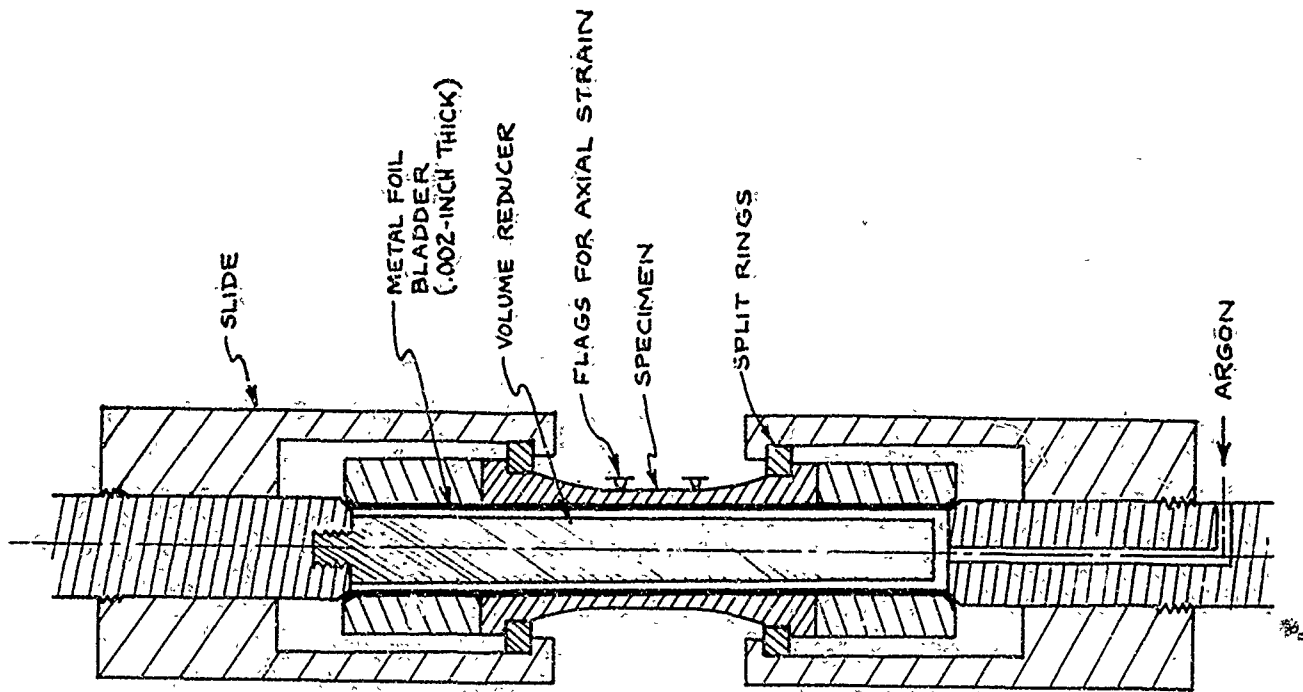
Figure 7. Biaxial Test Set-Ups

16

As indicated in Figure 7, a thin rubber balloon was used at room temperature to prevent penetration of the pressurizing fluid (water containing soluble oil) into the graphite specimen, and a metal foil bladder was used to seal the pressurizing medium (argon) at elevated temperature. For tests at 2000°F, the bladder was a seamless electrodeposited nickel tube, 0.002 to 0.003 inches thick. At 2000°F the flow strength of the nickel bladder is low and at failure of the graphite specimen accounts for less than two percent of the load and pressure carrying capacity of bladder/specimen combination.

The effect of the nickel bladder on the calculated stresses in the graphite can be estimated as:

$$\frac{\sigma}{\sigma_G} = 1 + \frac{\sigma_N \, t_N}{\sigma_G \, t_G}$$

where

σ = nominal stress in graphite, calculated from equations in Section 3.1.1

σ_N = stress carried by nickel bladder

σ_G = stress actually sustained by graphite

t_G = thickness of graphite tube $\cong$ 0.050 inch

t_N = thickness of nickel bladder $\cong$ 0.002 to 0.003 inch

The maximum value of σ_N is the yield strength of the nickel at 2000°F which is estimated at 1000 - 2000 psi. The effect of the bladder at fracture of the graphite (taken nominally as 4500 psi tensile strength) is then approximately

$$\frac{\sigma}{\sigma_G} = 1 + \frac{1500}{4500} \times \frac{0.0025}{0.050} \cong 1.017$$

or less than two percent. At fracture therefore, this effect is comparable in magnitude, but opposite in sign, to the effect of load-train friction.

17

However, at lower stresses, of interest with respect to stress-strain data, the effect of the bladder could be more significant. For example, at approximately 1,000 psi stress in the graphite, the bladder's effect could be as large as ten percent of the applied stress.

The furnace shown in Figure 8 was used for elevated temperature tests. Heating of the specimen is by radiation from six ohmically-heated graphite elements, which surround the specimen, and by convection in the argon atmosphere maintained within the furnace. The furnace is provided with sight-ports so that strains and temperature can be measured optically (Figure 9).

Most tests were conducted using approximately radial loading. That is, the pressure was manually controlled to increase in proportion to the axial load so that the ratio of axial stress to hoop stress was approximately constant. Some deviations from the desired stress-ratio occurred during loading. The points through which the published biaxial stress-strain curves (References 1 through 4) were plotted were taken from the data recordings at the indicated stress ratios, as illustrated in Figure 10.

At room temperature, the strains were usually measured with two strain gages, one axially oriented and the other circumferentially oriented, mounted adjacent to each other on the outer surface at the middle of the gage section. Because only one gage was usually used for axial strains there is a potential effect of parasitic bending on the measured strain. The maximum magnitude of the bending strains is estimated at 3 percent of the measured strain (References 1 and 2). In those cases where multiple axial gages were used, the reading at fracture of any individual gage did not differ by more than 2.5 percent from the average strain.

At 2000°F, strains were measured optically using a Physitech Model 440 extensometer aimed at graphite "flags" mechanically attached to the specimen for axial strains, and an Optron Model 800 extensometer aimed at the diametral extremes of the specimen gage section for hoop strains. Figure 11 shows the flags and the relation of optical sighting points to the specimen. Axial
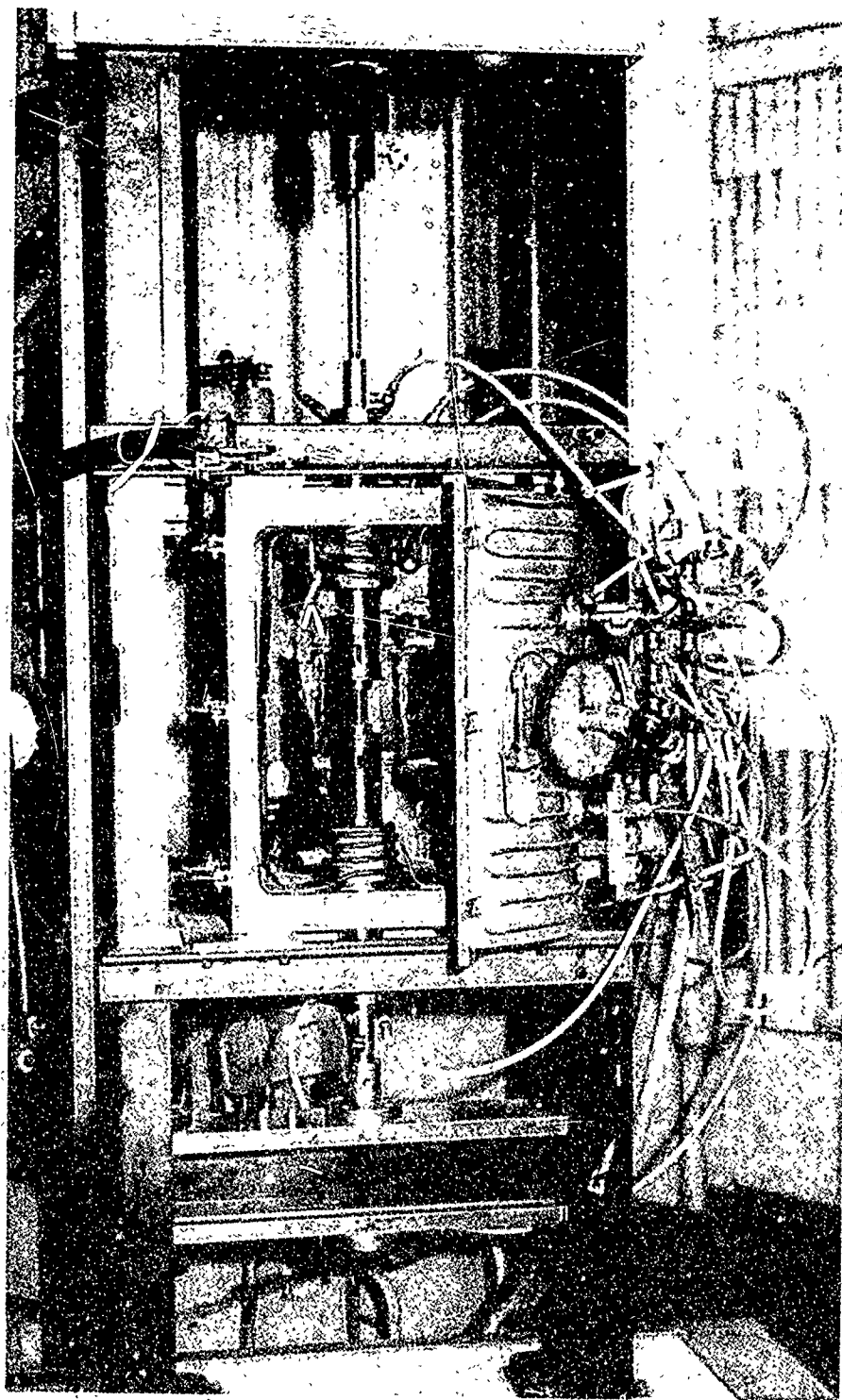
Figure 8. Biaxial Furnace

19
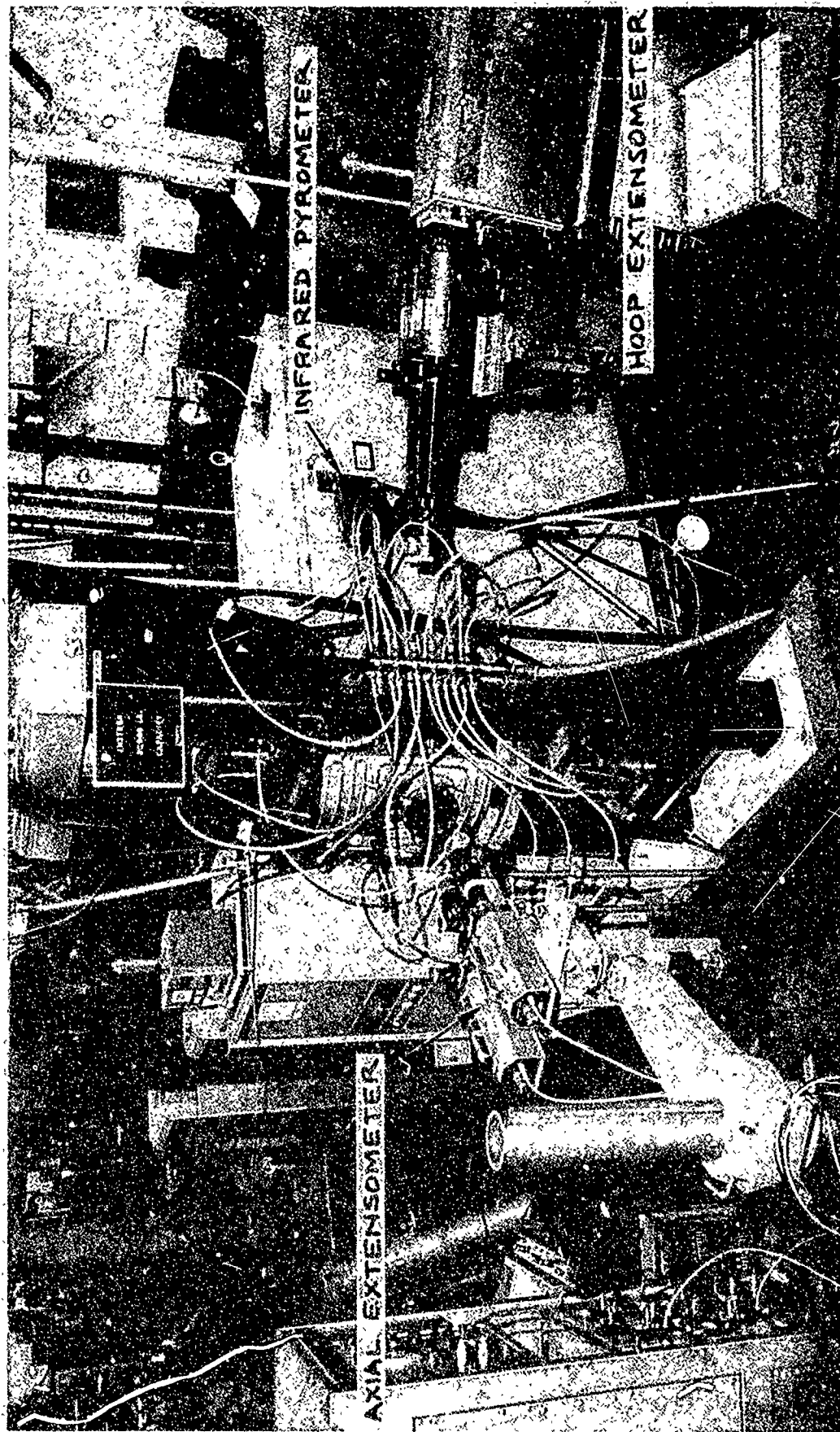
Figure 9. Furnace Instrumentation
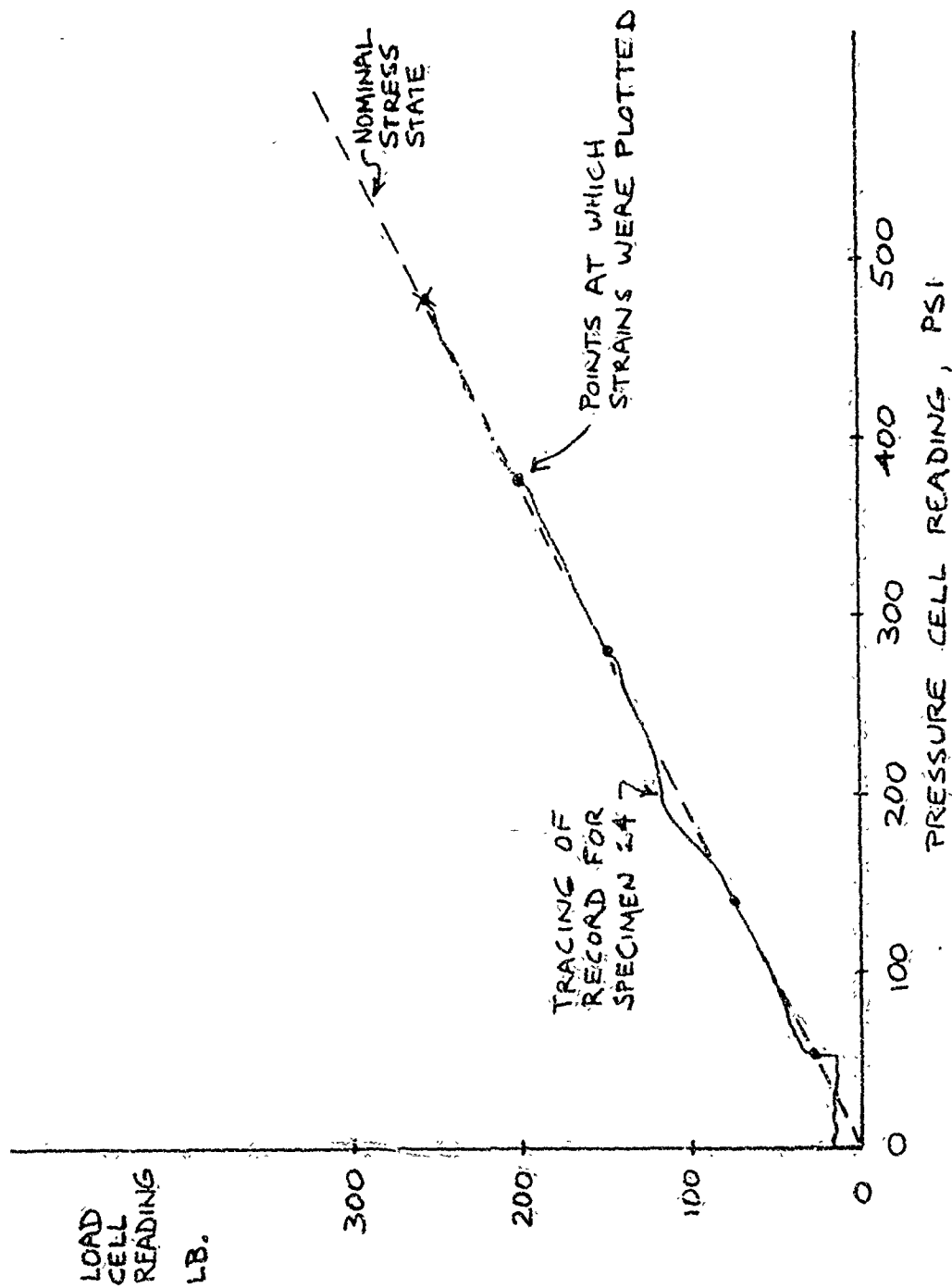
Figure 10. Typical Load-Path Data in Biaxial Test

21
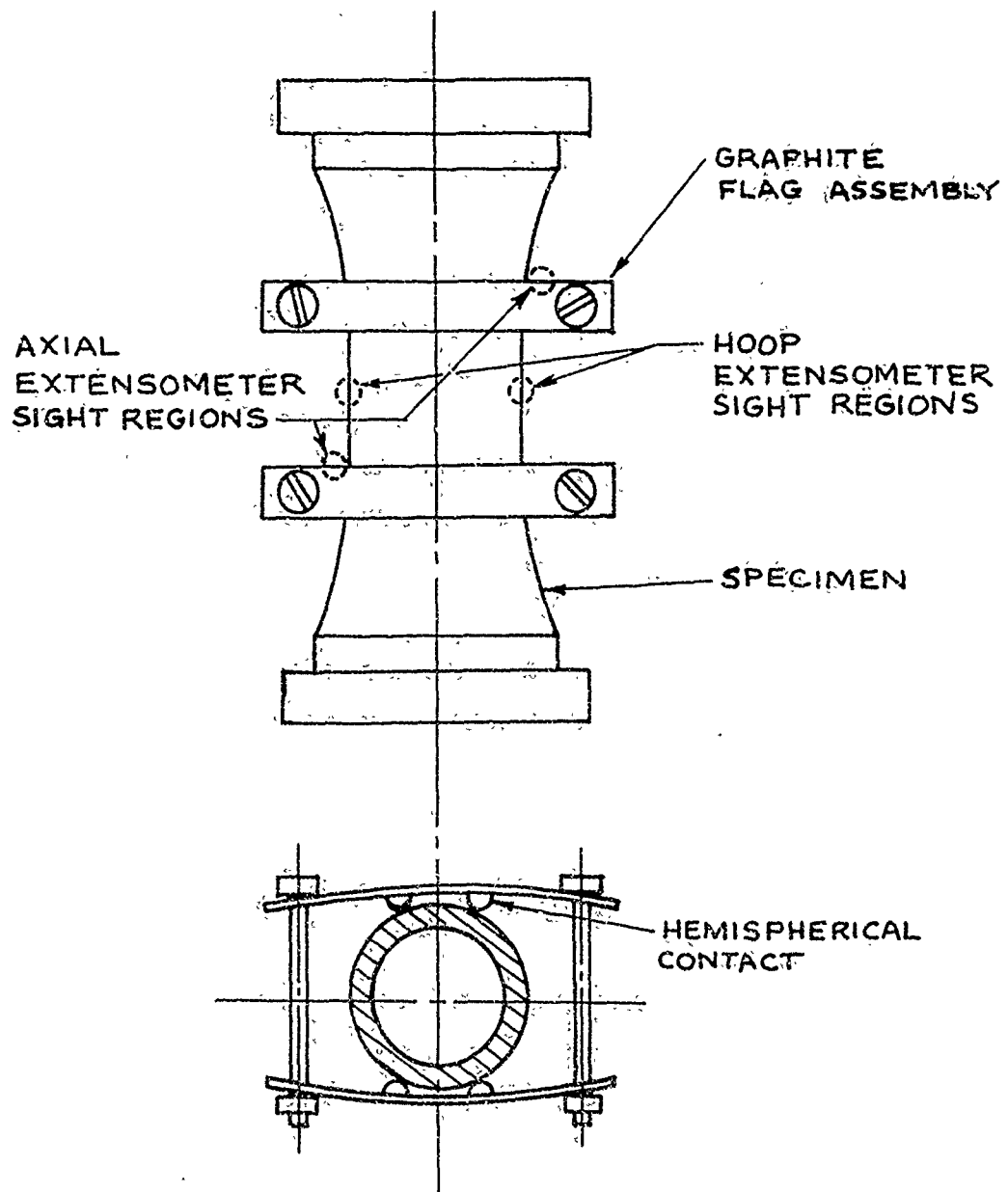
Figure 11. Biaxial Specimen and Flag Assembly for Strain Measurement at Elevated Temperature

sightings were at opposite sides of the specimen to minimize the effects of bending. The flags were designed to be flexible so they exert little diametral constraint on the specimen while maintaining contact in spite of diametral strains.

Calibration tests on the optical extensometers show that the strain data is repeatable and accurate within approximately $\pm$ 0.0002 inches per inch, for the axial strains, and somewhat less accurate (approximately $\pm$ 0.0003 inch per inch) for the hoop strains. The lesser accuracy in the case of hoop strain is believed due to difficulties in adequately focusing the extensometer on the "edge" of the cylindrical specimen. Part of the uncertainty in both extensometers is the "noise" due largely to convection currents within the test furance. Traces representative of the type of load-strain data obtained are shown in Figure 12.

3.1.1 Data Reduction

Nominal stresses were calculated from the loading data using the following equations, which are "thin-wall" approximations:

$$\sigma_{A_m} = \frac{L + \pi r_{iB}^2 P}{\pi(r_o^2 - r_i^2)} \tag{1}$$

$$\sigma_{H_m} = \frac{P\, r_{iB}}{r_o - r_i} \tag{2}$$

where

σ_{A_m} = mean axial stress, psi

σ_{H_m} = mean hoop stress, psi

L = measured load, lb

P = internal pressure, psi

r_o = outer radius of gage section, in.

r_i = inner radius of gage section, in.

r_{iB} = effective inner radius, in.

23

a) P vs. e_H

b) P vs. e_A

100 psi

←0.001→

←0.001→
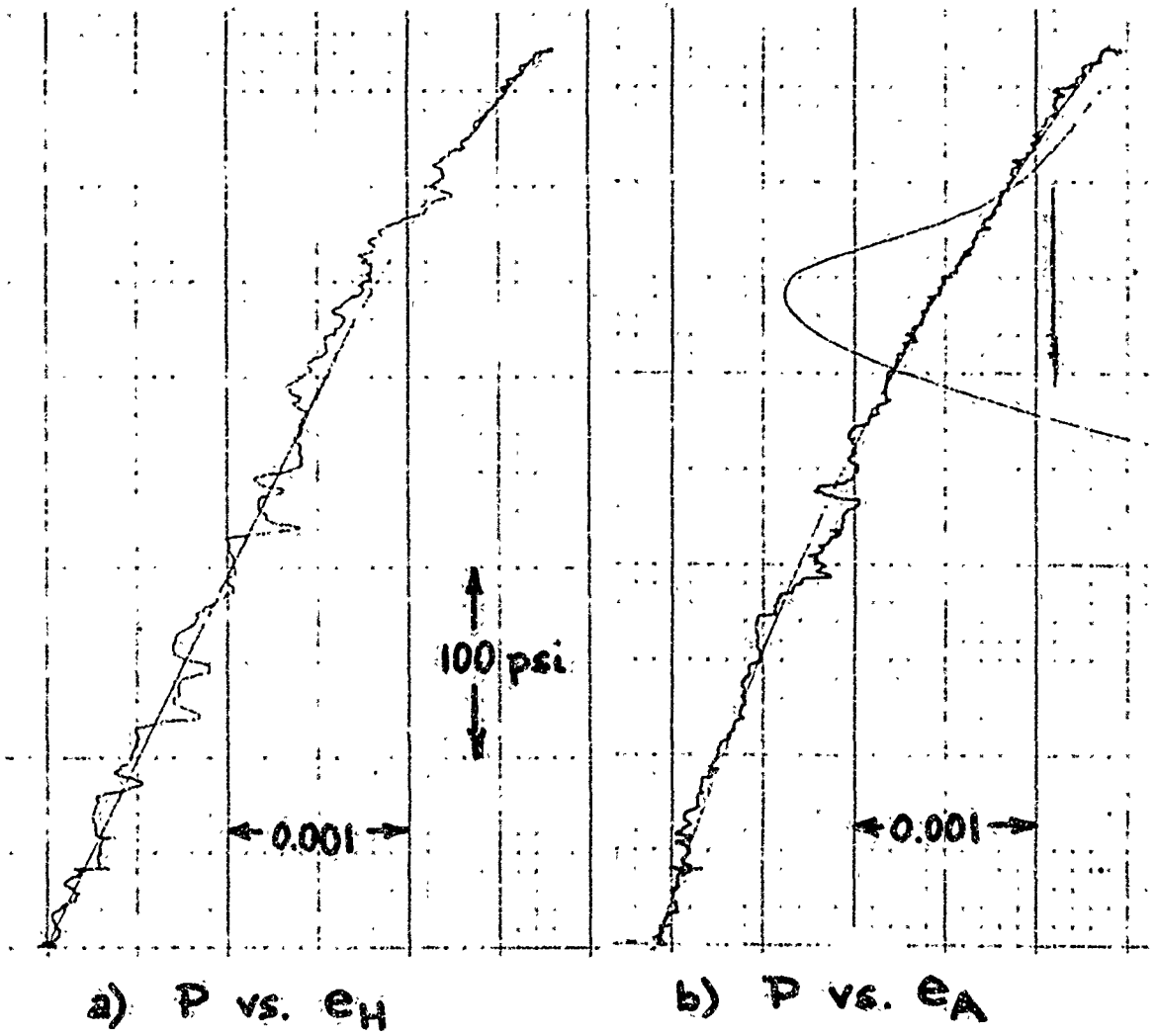
Figure 12. Typical 2000°F Strain Measurements

For tests at room temperature r_{iB} was taken as equal to r_i on the assumption that the rubber bladder acts like a fluid under pressure. For tests at 2000°F, r_{iB} was taken as the nominal internal radius of the nickel bladder, $r_{iB} = r_i - t_B$, where t_B is the measured bladder thickness.

Strains were obtained from the strain gage and extensometer readings in the usual manner. In the case of strain gages, the readings were corrected for the transverse sensitivity of the gage using the transverse sensitivity factor supplied by the gage manufacturer.

It should be noted that equations (1) and (2) represent the average or mean stresses in the gage section. Because of bending, axial stress gradients, and the radial stress gradients unavoidably present in any pressurized cylinder, the maximum stresses are somewhat (less than 10 percent) higher. In principle, if the location of the fracture origin within the specimen were precisely known the stress at fracture could be located using the types of stress analysis described in Section 3.2. Rarely, however, can the fracture origin be located with adequate precision, without extraordinary effort. The mean stresses therefore have been used to represent the fracture strength in References 1, 2 and 3. Since the stress gradients are not strongly affected by the ratio of applied load to applied pressure, the mean stresses at fracture are believed to give an adequate picture of biaxial effects on strength.

The stress gradients also affect the interpretation of biaxial stress-strain data. Strains were measured at the outer surface where the stresses may be expressed as:

$$\sigma_{A_o} = \sigma_{A_m} \tag{3}$$

$$\sigma_{H_o} = K\sigma_{H_m} \text{, where } K < 1.0 \tag{4}$$

Thus the hoop stress calculated from equation (2) should be corrected by the factor K before plotting stress-strain response data. Based on the analysis discussed in Section 3.2, K = 0.96 ± 0.01. In the biaxial stress-strain curves presented in References 1, 2, 3 and 4, the correction factor K was not used. As pointed out in these references, the absence of the correction should not affect the inferred effects of biaxiality, because biaxiality has only a small effect on K.

Strain gradients of course accompany the aforementioned stress gradients. Only the measured (outer surface) strains at fracture have been presented in References 1, 2 and 3. As shown in Section 3.2, the maximum hoop strain at failure is probably more than ten percent higher than the hoop strain measured at the outer surface of the specimen.

3.2 STRESS AND STRAIN GRADIENTS

Finite-element stress analyses of the biaxial specimen using the SAAS II code (Reference 15) with bilinear constitutive inputs for the graphite have been reported in References 1 and 2. Although these analyses were made using Poisson's ratios too large to correctly represent ATJ-S, the stress gradients are probably negligibly affected. Figure 13 shows estimated stress gradients in the 4.0-inch long biaxial specimen under combined tensile load and internal pressure; this combined loading results in the greatest stress concentrations at the ends of the uniform-section gage length.

Additional SAAS II analysis, using more representative Poisson's ratios, was reported in Reference 3. Results, showing the effect of applied stress state on the stress and strain gradients through the thickness of the biaxial specimen, are summarized in Figure 14. However, the strain results are somewhat suspect because the constitutive formulation in the SAAS II code does not truly represent ATJ-S graphite (See Section 5.1).
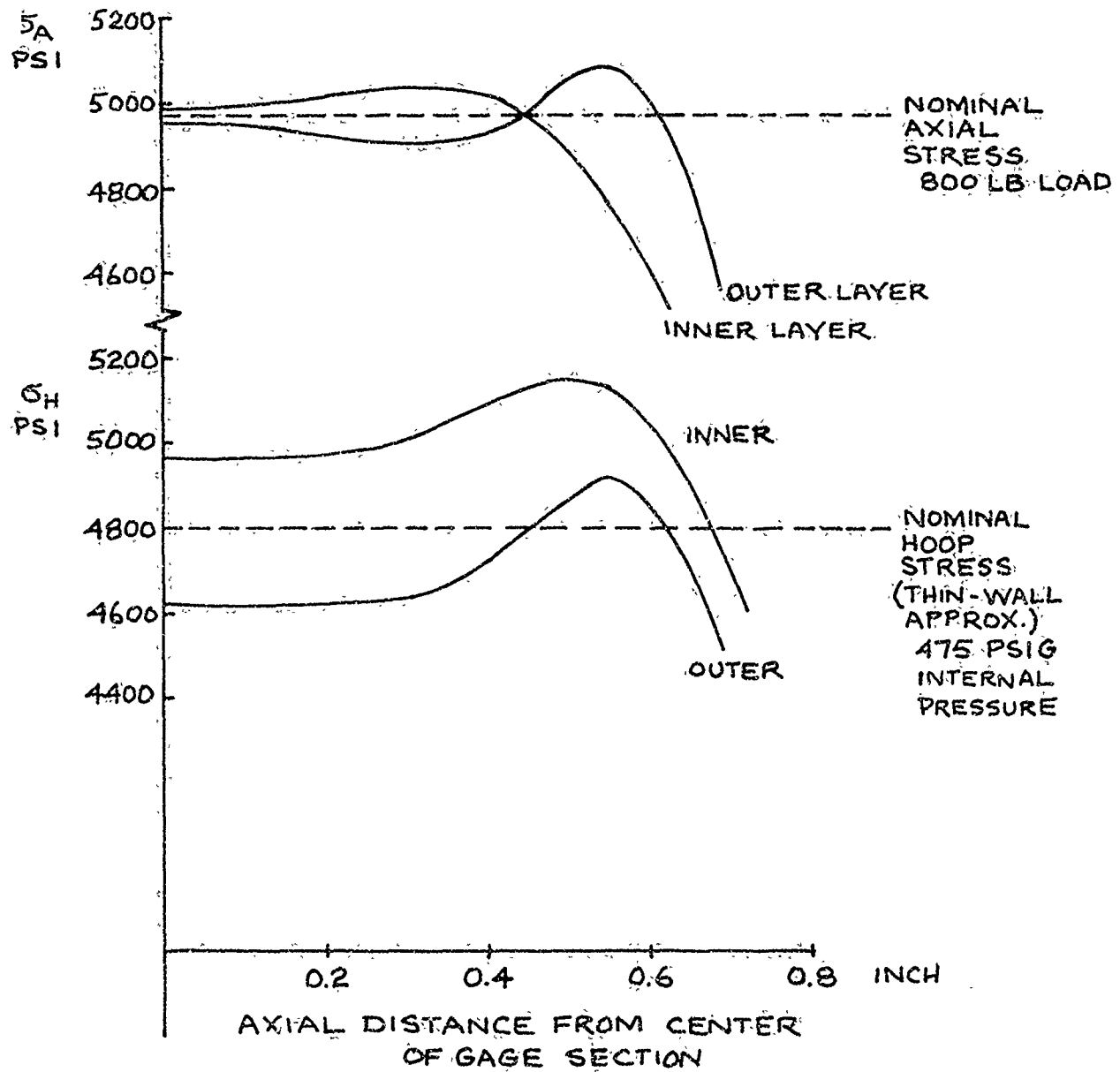
Figure 13. Stress Distribution in Biaxial Specimen Under Combined Loading
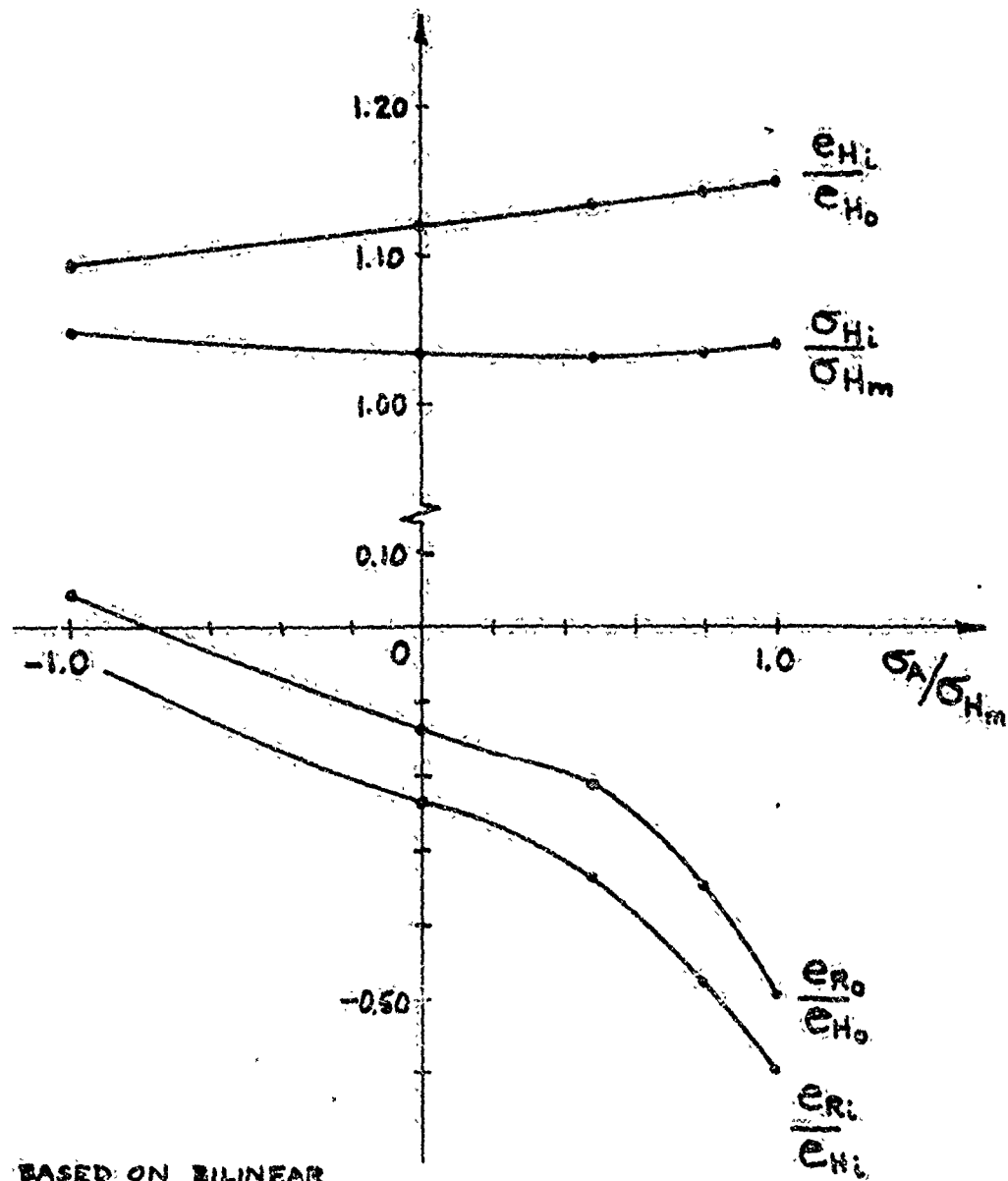
Figure 14. Estimated Hoop Stress and Strain Variations Across Biaxial
Specimen Wall at the Mid-Length Section and Estimated
Radial Strains, SAAS II Analysis

An alternate approach to estimating the strain gradients, based on a different constitutive assumption, may be informative. The hoop and radial strains are related by simple geometry:

$$(1 + e_{R_m})(r_o - r_i) = (1 + e_{H_o})r_o - (1 + e_{H_i})r_i \qquad (1)$$

Rearranging the terms gives:

$$\frac{e_{H_i}}{e_{H_o}} = \frac{r_o}{r_i} - \frac{e_{R_m}}{e_{H_o}} \frac{(r_o - r_i)}{r_i} \qquad (2)$$

To estimate the gradient in hoop strains it is necessary to estimate the ratio of radial strain to the hoop strain. To do so requires a constitutive law. The assumption made here is that the ratios of principal strains to one another remain constant during loading. This assumption is supported by the fact that the strain trajectories in biaxial and triaxial tests under proportional loading tend to be nearly linear (Reference 3, for example, and Section 5.4). The ratio of principal strains will then be approximately the same as that calculated using linear elastic theory:

$$\frac{e_{R_m}}{e_{H_o}} = \frac{\dfrac{1}{E_a}\sigma_{R_m} - \dfrac{\nu_{ab}}{E_a}\sigma_{H_m} - \dfrac{\nu_{ca}}{E_c}\sigma_{A_m}}{\dfrac{1}{E_a}\sigma_{H_o} - \dfrac{\nu_{ca}}{E_c}\sigma_{A_o}} \qquad (3)$$

Equation (3) may be simplified by substituting:

$$\sigma_{H_o} = \sigma_{H_m} = \sigma_H \quad \text{(within 5 percent)} \qquad (4)$$

$$\sigma_{A_m} = \sigma_{A_o} = \sigma_A \qquad (5)$$

$$\sigma_{R_m} = -\frac{P}{2} = \frac{\sigma_H}{2}\left(\frac{r_o - r_i}{r_i}\right) \qquad (6)$$

$$\frac{\nu_{ca}}{E_c} \cong 1.4\, \frac{\nu_{ab}}{E_a} \qquad \text{(Reference 3)} \tag{7}$$

$$\nu \equiv \nu_{ab} \tag{8}$$

to get:

$$\frac{e_{R_m}}{e_{H_o}} = \frac{-\dfrac{r_o - r_i}{2r_i} - \nu\left(1 + 1.4\,\dfrac{\sigma_A}{\sigma_H}\right)}{1 - 1.4\,\nu\left(\dfrac{\sigma_A}{\sigma_H}\right)} \tag{9}$$

The strain ratios calculated from equations (9) and (2) are sensitive to the value of Poisson's ratio assumed. The elastic value is approximately 0.1; however, the secant value near failure in tension at room temperature is about 0.05 (Reference 3).

By substituting equation (9) into equation (2), the hoop-strain gradient can be estimated, with the results shown in Figure 15, for a specimen with a wall-thickness equal to one-tenth its inner radius. It is seen that the alternate analysis gives slightly smaller strain gradients than does the SAAS II analysis.

In the region of interest with respect to hoop strains at failure, at stress states of σ_A/σ_H less than unity, the effect of assumed Poisson's ratio is fairly small. A fairly good compromise value of e_{H_i}/e_{H_o} appears to be 1.12, and this ratio is suggested as a correction factor to be applied to the measured hoop strains at failure to provide an estimate of the maximum (inner-wall) hoop strain at failure at the specimen mid-length section.

The hoop-stress gradient through the specimen wall is considerably smaller than the hoop-strain gradient, and less sensitive to constitutive assumptions. Based on the SAAS II analysis (Figure 14) a correction factor of 1.04 applied to the calculated mean hoop stress (Equation 2 in Section 3.1.1) would appear to give an adequate approximation to the maximum hoop stress at failure, in the specimen mid-length section.

30
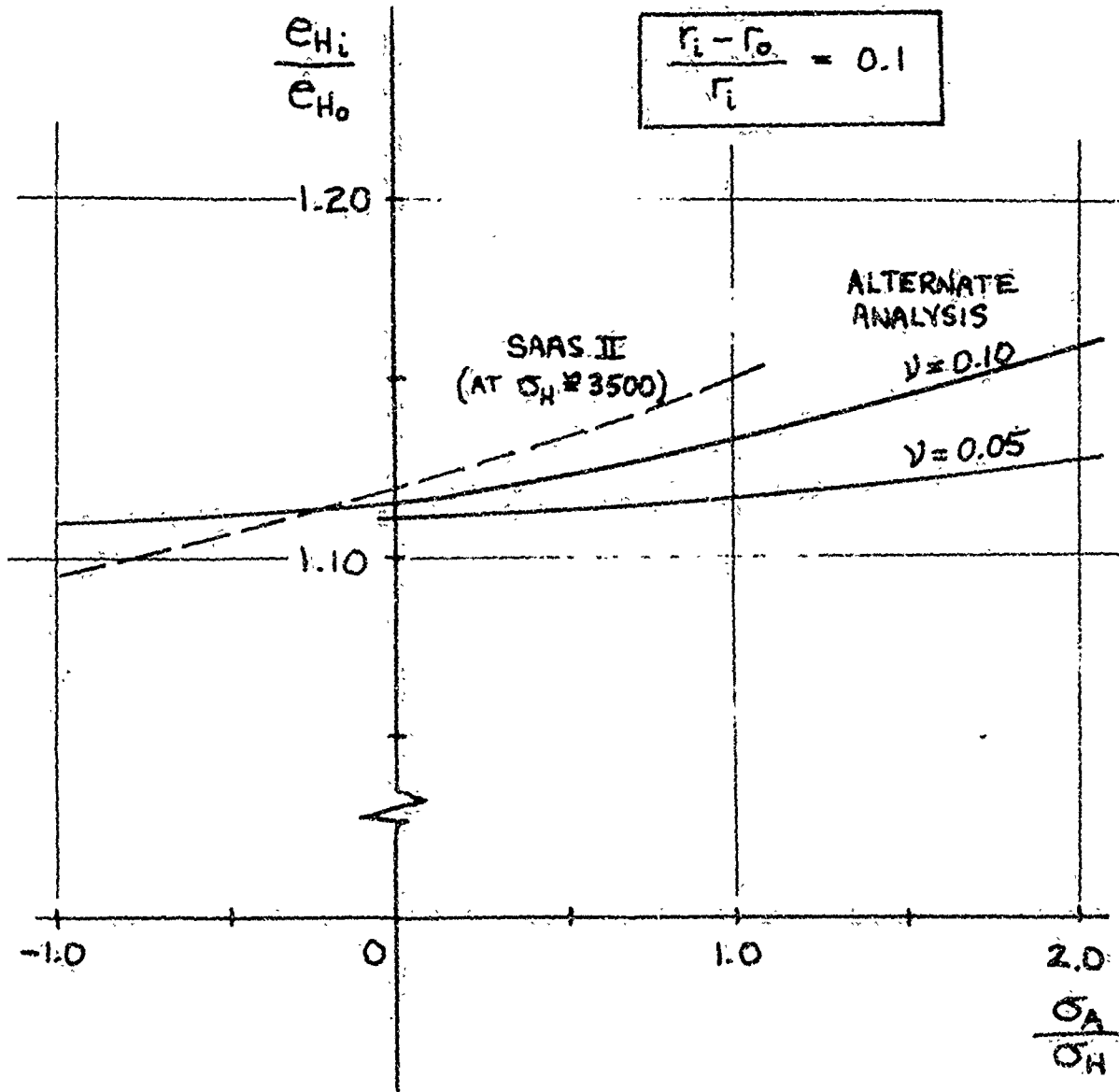
Figure 15. Estimated Hoop Strain Gradients, Biaxial Specimen

Both the SAAS II and the alternate analysis serve to show that the strain
state is distinctly triaxial. Figure 16 shows the estimated ratio of radial
strain (compressive) to hoop strain, as a function of applied stress ratio.
The alternate analysis predicts significantly smaller radial strains than
does the SAAS II analysis.

The stress-state is, of course, also triaxial. However the radial stress
(always compressive) never exceeds the internal pressure and is therefore
less than one-tenth of the hoop stress in absolute magnitude. At the outer
surface of the specimen the radial stress is zero.

3.3 UNIAXIAL TECHNIQUES

Two types of uniaxial tensile specimens have been used in the referenced
studies (References 1, 2, 3 and 4). Figure 17 shows the usual button-head
rod specimen which is loaded with split-collar rings in the same sort of
rigid-alignment fixture as used in the biaxial tests. As in the biaxial
tests, friction can cause the measured load to be about one percent less
than the load actually sustained by the specimen.

Axial stress is calculated simply by dividing the applied load by the
measured cross-sectional area of the specimen. As in the biaxial specimen,
axial stress gradients exist in the uniaxial rod and the peak stress is
found near the tangent points at the ends of the uniform-section gage length.
Using the stress-concentration factors provided for a linear-elastic material
in Reference 29, together with an estimated factor (approximately one-half)
to account for the nonlinearity of ATJ-S strain response, the stress increase
at the ends of the gage length is estimated at about three percent.

The second type of tensile specimen, used in the off-axis study in Reference 2,
is a square-section "bar" (Figure 18). Because this specimen was loaded in a
pinned load train, not using the rigid-alignment fixture, there is no friction
to account for. However the increased possibility of bending probably
counters any advantage therefrom. The very gentle radius leading to the
uniform-section gage length results in an estimated stress concentration at
the ends of the gage length of less than one percent (Reference 29).
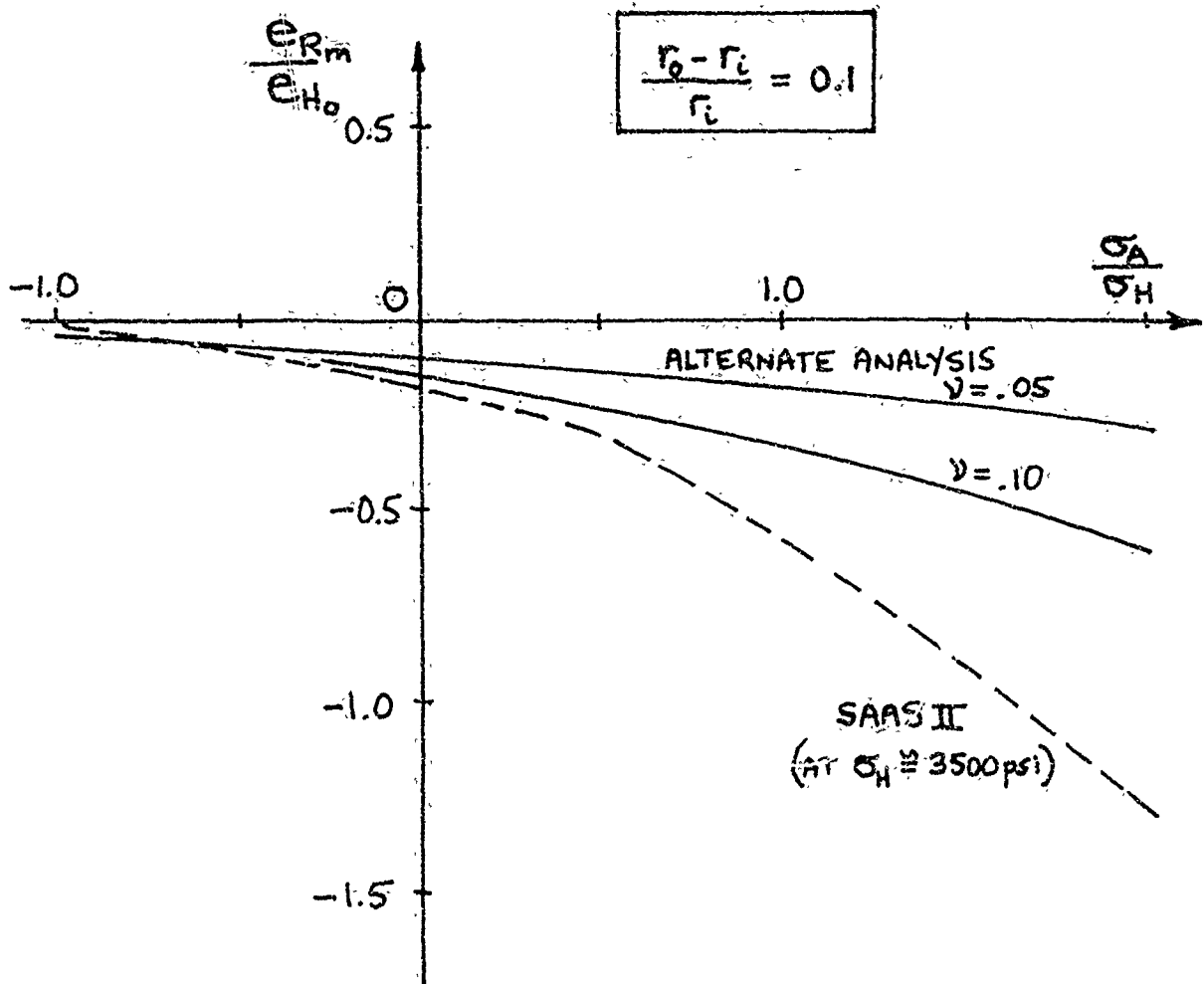
Figure 16. Radial Strain Estimates, Biaxial Specimen

Figure 17. Tensile Specimen (Rod)

NOTES

1. UNSPECIFIED TOLERANCES ±.010
2. UNSPECIFIED SURFACE FINISH 16

.750 R. (TYP) NO U'CUT
AT TAN. PT. TO .250 DIA.

.3750 +.0000 DIA.
      -.0005

.625 DIA

64

64

1.39 (REF)

.250 ±.001 DIA.

.045 R
.025
(TYP)

.500 (TYP)

.500 (TYP)

4.000 ±.020

34

Figure 18. Tensile Specimen (Bar)
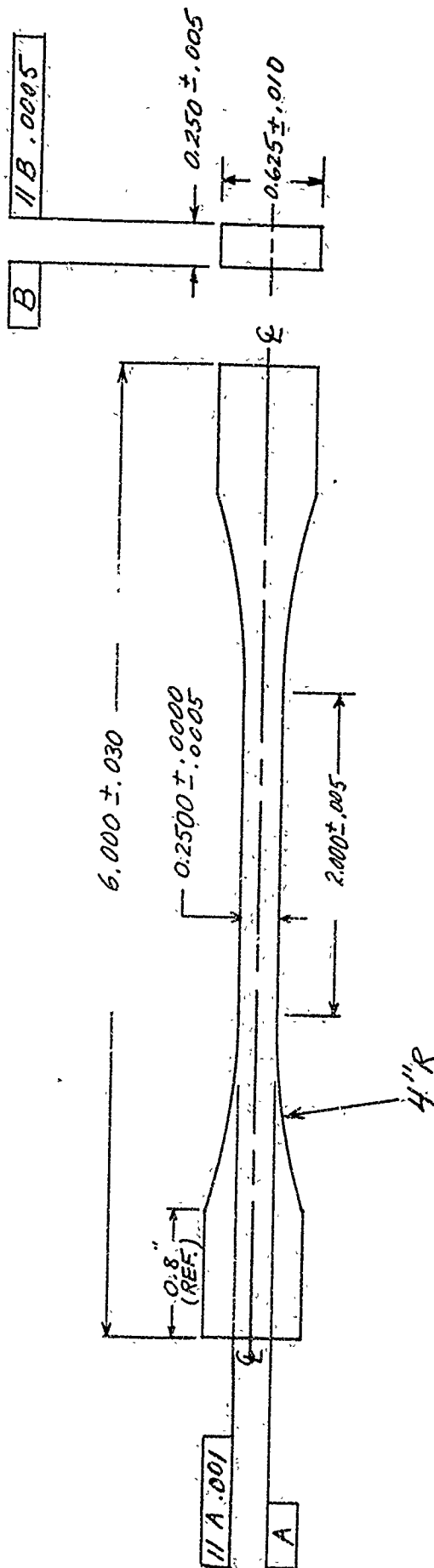
NOTES:

1. ALL SURFACES MACHINED TO ∇32 ROUGHNESS OR BETTER.

2. NO UNDERCUTTING PERMITTED WHERE 4"R BLENDS INTO REDUCED SECTION EDGE.

35

3.4 COMPARISONS OF UNIAXIAL TENSILE DATA

Comparisons of the stress-strain responses measured with biaxial specimens (in uniaxial stress-states) with those obtained from uniaxial specimens are shown in Figures 19, 20 and 21 (re-plots of data presented in Ref 4). Figures 19 and 20 show that the axial (across-grain) stress-strain responses for biaxial specimens from two billets are quite close to the data from uniaxial rods from the same billets. The discrepancy in transverse stress seen in Figure 20 is large percentage-wise but represents a very small absolute difference in measured strains. Figure 21 shows that when the nominal thin-wall hoop stress is corrected by four percent (K = 0.96) to give the hoop stress at the outer surface of the biaxial specimen, where the strains are measured, the stress-strain response for the biaxial specimen falls in line with the uniaxial specimen data.

Comparisons of uniaxial strength data, as in Table III, show the uniaxial specimens to give discernibly higher strength values than do the biaxial specimens in equivalent uniaxial stress-states. Possible reasons for such a discrepancy include:

A. Greater stress gradients exist in the biaxial specimen than in the uniaxial specimen.

B. Experimental uncertainties including those attributable to bending, friction, and the presence of the pressure-containing bladder.

C. The biaxial specimen is of larger volume and has greater surface area and would therefore be more likely to contain strength reducing flaws.

D. The 0.050-inch wall thickness of the biaxial specimens may be insufficient to represent the bulk material, may lead to a change in fracture mode, or increase the sensitivity to flaws.
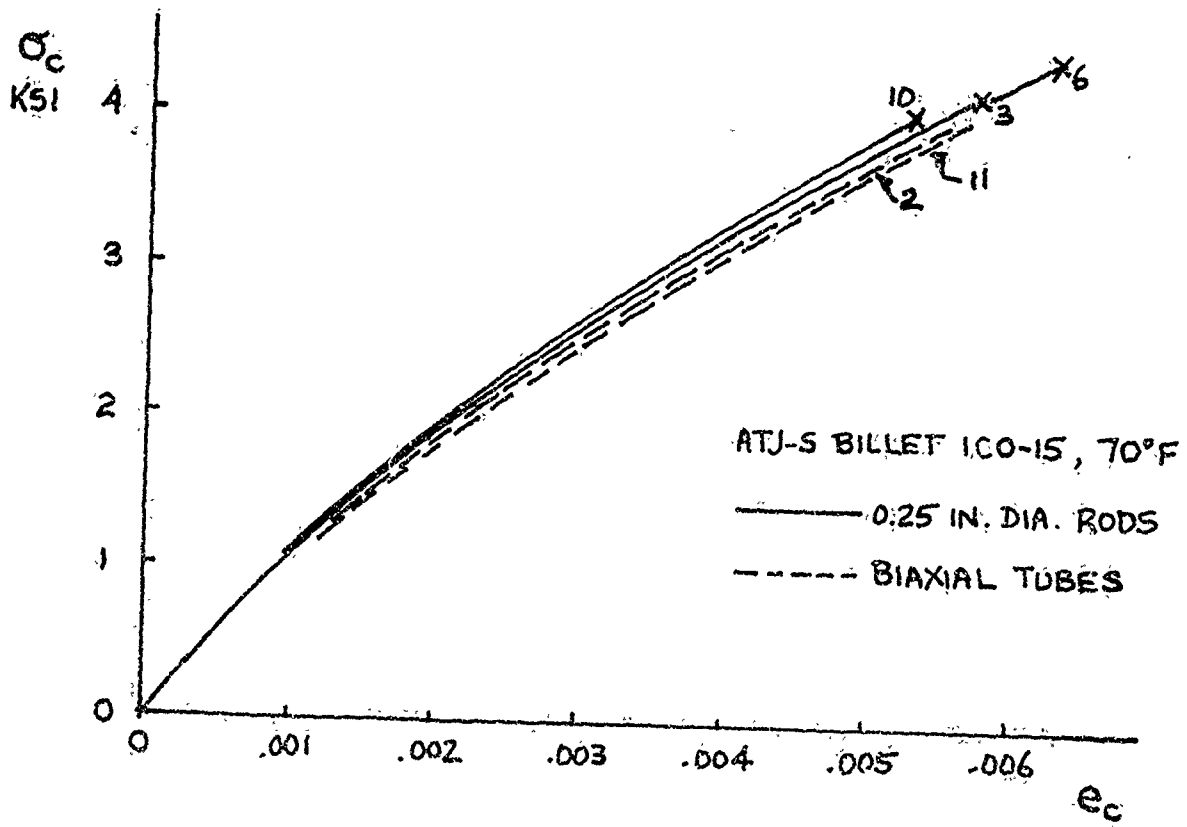
Figure 19. Across-grain Tension Strain Responses, Billet 1C0-15

ATJ-S BILLET 16K9-27, 70°F
——— 0.25 IN. SQUARE TENSILE BARS
——— BIAXIAL SPECIMENS
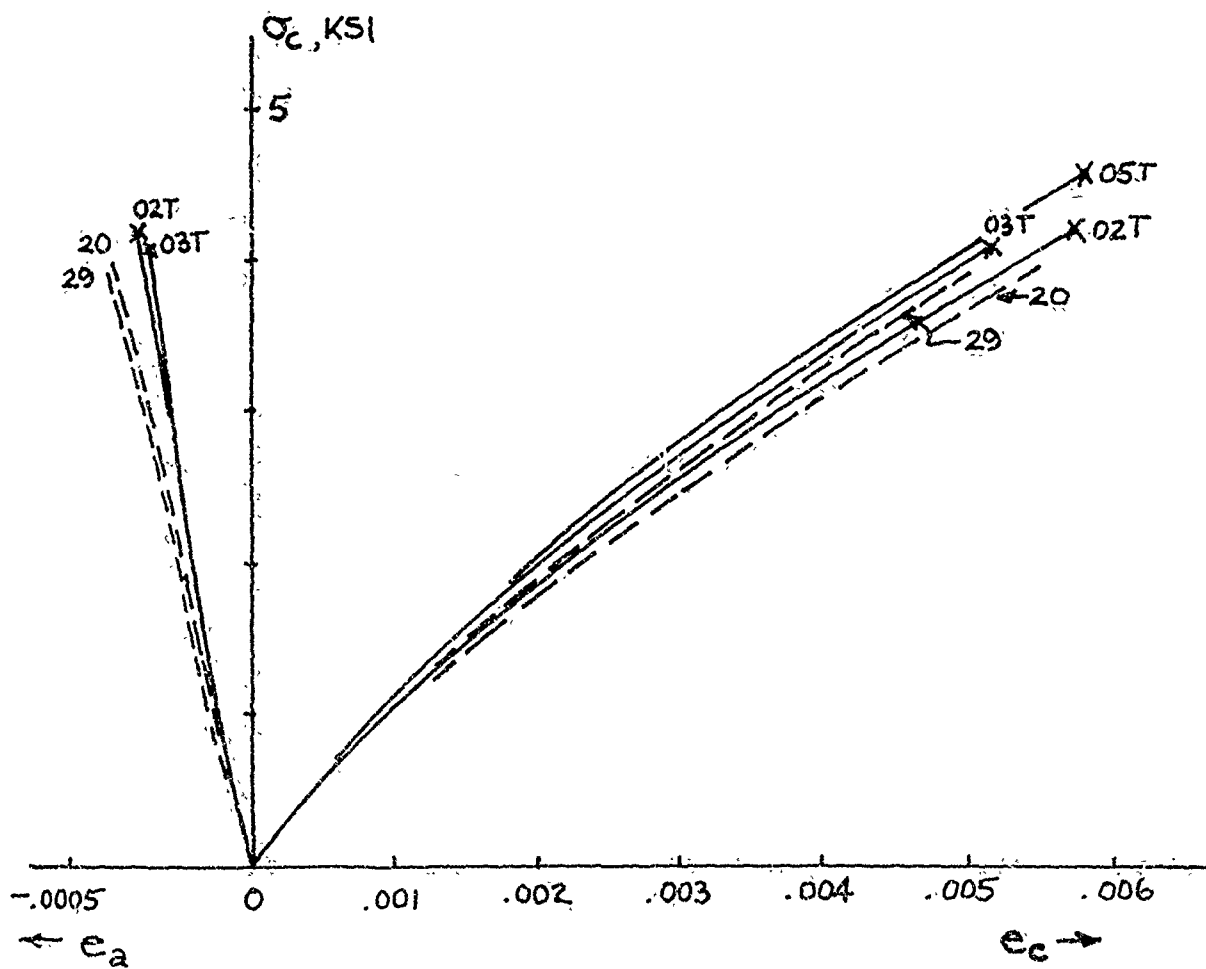
Figure 20. Across-grain Tension Strain Responses, Billet 16K9-27
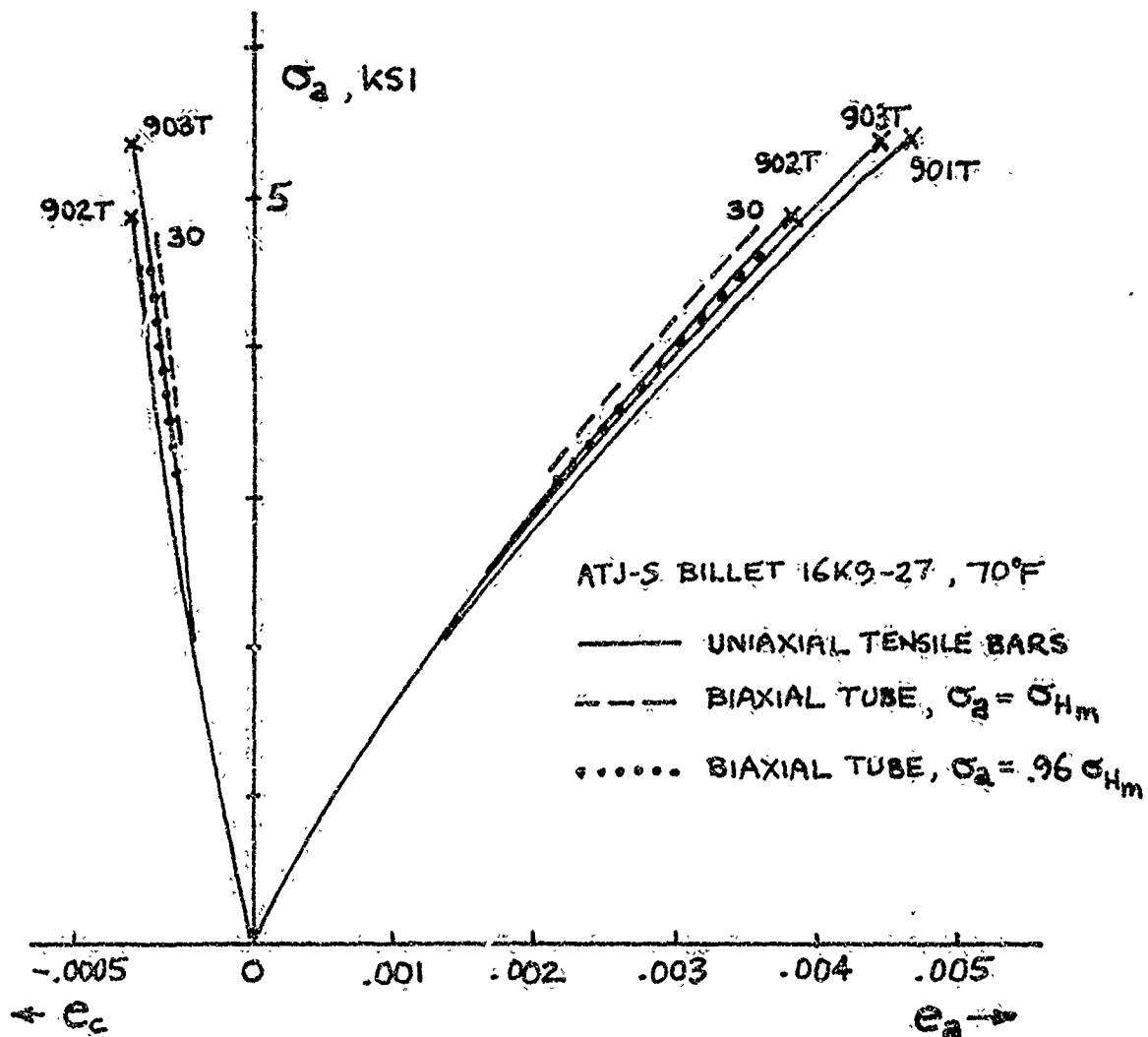
Figure 21. With-grain Tension Strain Responses, Billet 16K9-27

TABLE III

COMPARISON OF TENSILE STRENGTHS, BIAXIAL AND UNIAXIAL SPECIMENS

| | SPECIMEN TYPE | | | | % STRENGTH DIFFERENCE |
| | BIAXIAL | | UNIAXIAL | | |
	SHORT (REF 1)	LONG (REF 2)	ROD	SQUARE SECTION BAR	
Specimen Geometry					
Wall thickness, in.	0.050	0.050	Solid	Solid	---
Diameter, in.	1.00	1.00	0.25	0.25	---
Gage Volume, in^3	0.17	0.21	0.07	0.15	---
Gage Surface, in^2	6.8	8.5	1.2	2.4	---
Across-grain Strength, psi					
Ref 1 All billets	3770[3]*	----	3960[3]	---	5
Ref 2 Billet 1CO-15	----	4025[2]	4200[3]	---	4
Ref 2 Billet 16K9-27	----	3940[2]	----	4240[5]	7
With-grain Strength, psi***					
Ref 1 Billet 4R9-1	5000[1]	----	4830[4]**	----	-3
Ref 1 Billet 3R9-33	4100[2]	----	5033[4]**	----	23
Ref 2 Billet 16K9-27	----	4800[2]	----	5200[3]	8

* Numbers in [ ] denote number of specimens tested to give tabulated
average strength.

** These uniaxial rods, tested at Union Carbide, are of different design
than the others; gage volume unknown; gage diameter 0.25 inch.

*** Strength tabulated for the biaxial specimens is the mean hoop strength
obtained from "thin-wall" formula.

To address the first two possibilities, the uncertainties and estimated gradients in the stresses and strains at failure are summarized in Table IV. Shown in Table IV are approximate percentage corrections that should be added to the nominal failure stresses and strains (obtained by the procedures outlined in the preceding section and presented in References 1 through 4) to reach an estimate of the maximum stresses and strains existing in the specimen at the time of fracture. Also tabulated are the corresponding uncertainties and gradient effects for uniaxial rod specimens. Subtracting the total corrections for the uniaxial specimen from the total corrections for the biaxial specimen, as in Table IV, gives the following conclusions:

A. At room temperature and 2000°F, the average axial (across-grain) strength data of the biaxial specimen may be expected to be about the same as the corresponding data from uniaxial specimens.

B. At both temperatures, axial (across-grain) strain-at-failure measurements should be nearly equivalent for both types of specimens, although, at elevated temperature, the uncertainty in strain measurement is relatively large.

C. Hoop (with-grain) strengths based on the thin-wall stress formula (Pr/t) may be increased by up to about four percent to put them on the same basis as with-grain strength measured with uniaxial specimens.

D. Measured hoop strains may be increased by up to about fourteen percent to put them on the same basis as the failure strains recorded in tests on with-grain uniaxial specimens.

In addition to the factors listed in Table IV, the biaxial specimen differs from typical uniaxial specimens in volume, surface area, minimum dimension of gage section, and complexity of fabrication.

Volume effects have been studied experimentally for ATJ graphite (Ref 7). That study and additional work on other grades, including ATJ-S, provide the conclusion that volume does not affect the strength of graphite as much as

41

TABLE IV

POTENTIAL UNCERTAINTIES AND BIASES IN FAILURE DATA

	POTENTIAL EFFECT, PERCENT [1]					
	TENSILE STRENGTH			STRAIN-AT-FAILURE		
	BIAXIAL SPECIMEN			BIAXIAL SPECIMEN		
FACTOR	ACROSS GRAIN (AXIAL)	WITH GRAIN (HOOP)	UNIAXIAL SPECIMEN	ACROSS GRAIN (AXIAL)	WITH GRAIN (HOOP)	UNIAXIAL SPECIMEN
Friction	+ 1		+ 1			
Bending	+ 2		+ 1	± 3		± 2
Area Measurement	1 ± 1	1 ± 1	± 0.5			
Bladder [2]	(– 2)	(– 2)				
Radial Stress Gradients		+ 4			+ 12	
Axial Stress Gradients	+ 2	+ 4	+ 3	+ 3	+ 6	+ 4
Load & Pressure Transducer Error	± 1	± 1	± 1			
Strain-Gage Error				± 1	± 1	± 1
Optical Extensometer [2]				(± 5)	(± 10)	(± 5)
Recorder Error	± 1	± 1	± 1	± 1	± 1	± 1
Total at 70°F	6 ± 3	9 ± 3	5 ± 2.5	3 ± 5	18 ± 2	4 ± 4
Total at 2000°F	4 ± 3	7 ± 3	5 ± 2.5	3 ± 9	18 ± 11	4 ± 8
Net Effect [3] at 70°F	1	4	0	– 1	14	0
Net Effect [3] at 2000°F	–1	2	0	–1	14	0

NOTES: (1) Numbers shown are percent to be added to nominal strength and strains-at-fracture to obtain maximum values in specimen.

(2) Effect at elevated temperature only.

(3) Net effect is the estimated average percent correction to be applied to the data to put it on same basis as uniaxial specimen data.

42

weakest-link statistics would predict; the effect, in the range of volumes of interest here, is approximately 10 to 12 percent reduction in average strength per tenfold increase in volume (Ref 8). For the three-to-one volume ratio between the biaxial specimen and the uniaxial rods, a strength difference of about 3 percent would be expected.

To the author's knowledge, surface area effects have not been studied independently of volume changes for graphites. According to Reference 7, surface finish (in the machinist's terminology) has little effect on strength. However, an increase in surface area must be accompanied by an increased probability of surface damage during fabrication and handling of the specimen; especially when combined with increased complexity of fabrication as in the case of the biaxial tube. Unfortunately no systematic study of machining damage to the relatively delicate biaxial tube specimen has been undertaken.

Concern has been expressed (References 1 and 2) that the 0.050-inch thickness of the biaxial specimen wall may not be enough to represent the bulk behavior of the ATJ-S graphite. As Figure 22 shows, the microstructure is fairly coarse relative to the wall thickness.

The fracture surfaces of a biaxial specimen and a uniaxial tension specimen were examined using a scanning electron microscope (SEM) at magnifications between 20X and 1000X. Both specimens were of ATJ-S graphite from Billet 16K9-27 (Ref 2). The biaxial specimen had been fractured in hoop tension, failing at a with-grain stress of approximately 4900 psi. The uniaxial specimen had fractured at a with-grain stress of about 5400 psi. Figure 23 shows composite views of the two fracture surfaces. The primary crack segment of the biaxial specimen was too long to conveniently fit the SEM stage; therefore the graphite piece was sawed in two as is obvious in the photos. It is believed that the fracture in the biaxial specimen initiated near the saw cut where the surface texture appears relatively smooth. As the crack ran towards the ends of the specimen, the surface texture became discernibly rougher (especially at the right-hand end). The scale of the surface features in the "smooth" region appears relatively small compared to the wall thickness of the biaxial cylinder (suggesting that a 0.050-inch wall

43
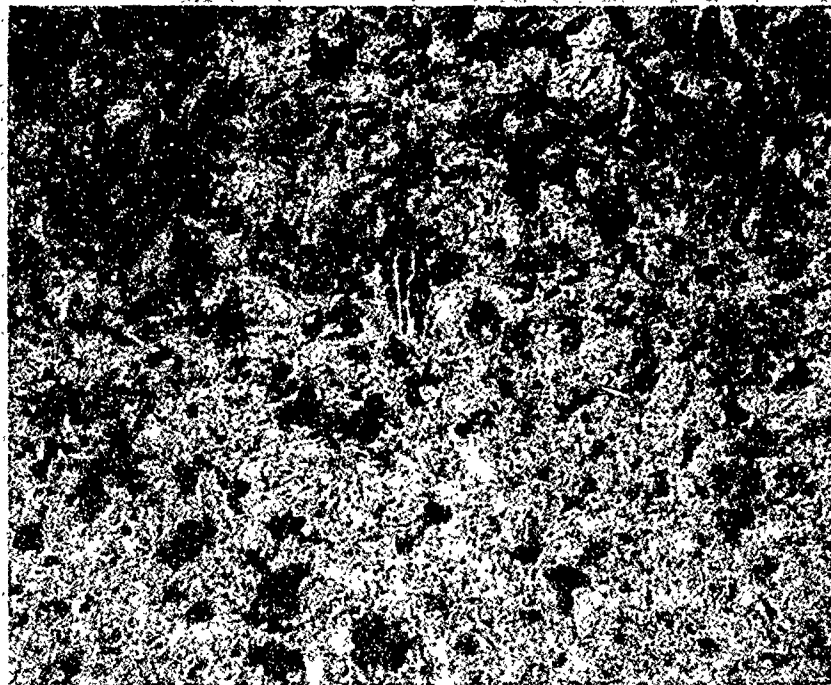
|←————— 0.050" —————→|

Figure 22. ATJ-S Microstructure
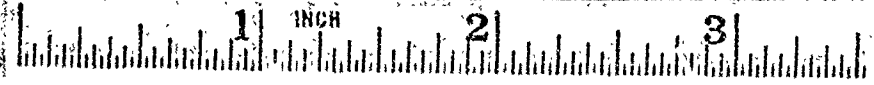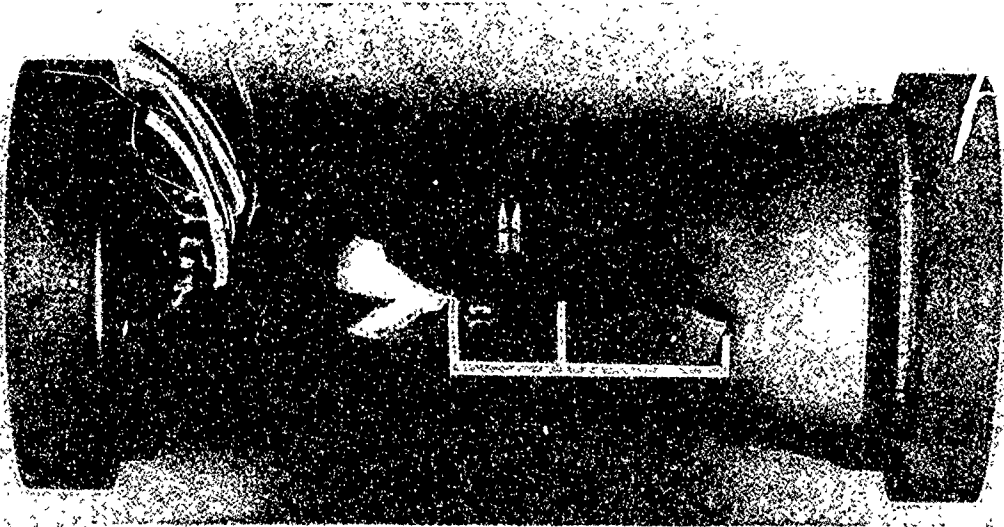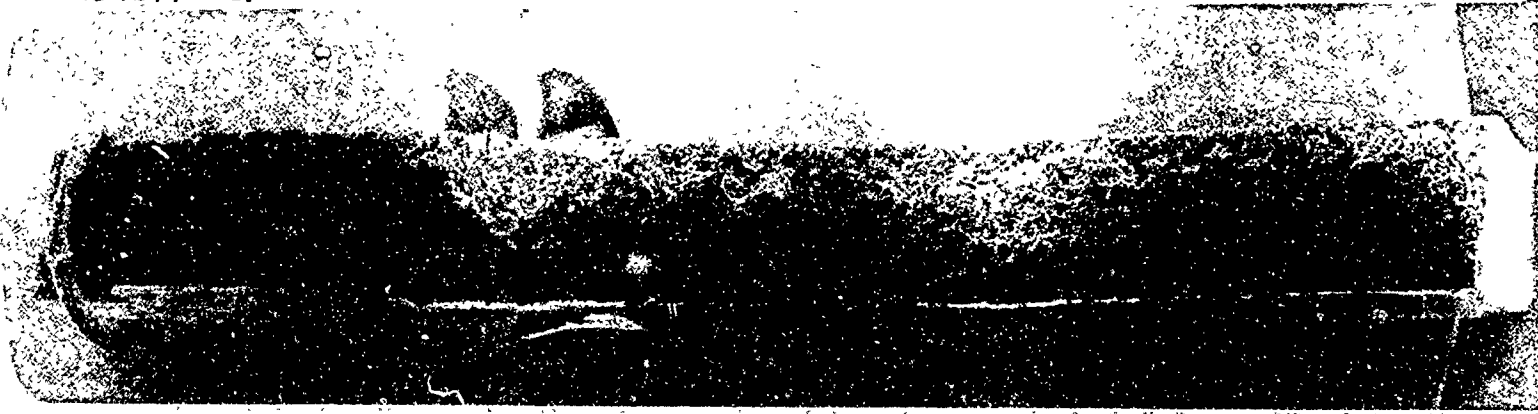
SPECIMEN   NO. _____ 25

BIAXIAL SPECIMEN TESTED IN HOOP (w.g.) TENSION
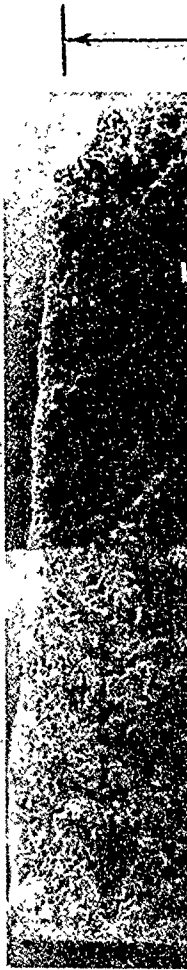
HS 4238 etc.
UNIAXIAL S

A

0.250 INCH

901T

1 INCH

UNIAXIAL SPECIMEN TESTED IN WIT

S.E.M. VIEWS OF A

HS 4238 etc.
UNIAXIAL SPECIMEN #901T

Figure

B
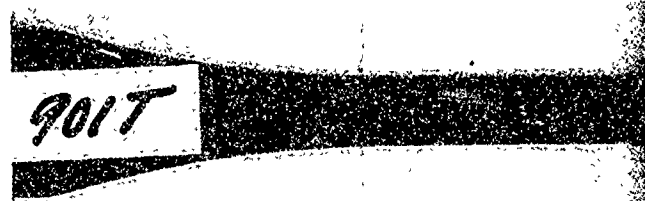
901 T

UNIAXIAL SPECIMEN TESTED IN

S.E.M. VIEWS OF

HS 4238 etc.
UNIAXIAL SPECIMEN #901T

Fig

B

901 T
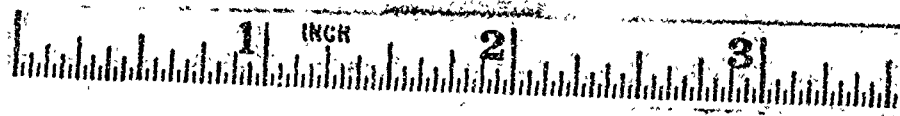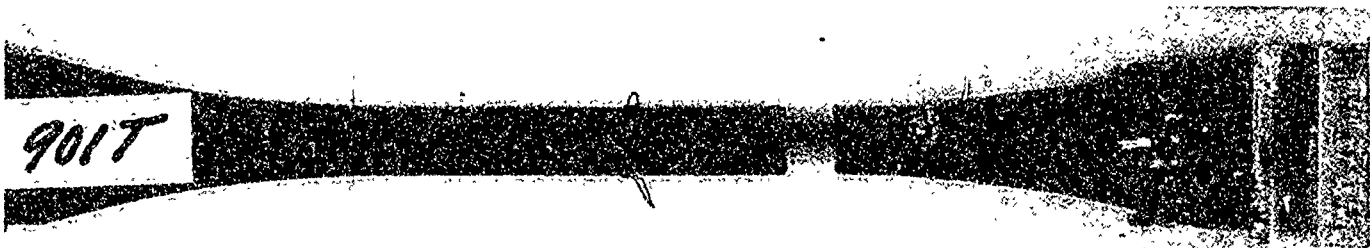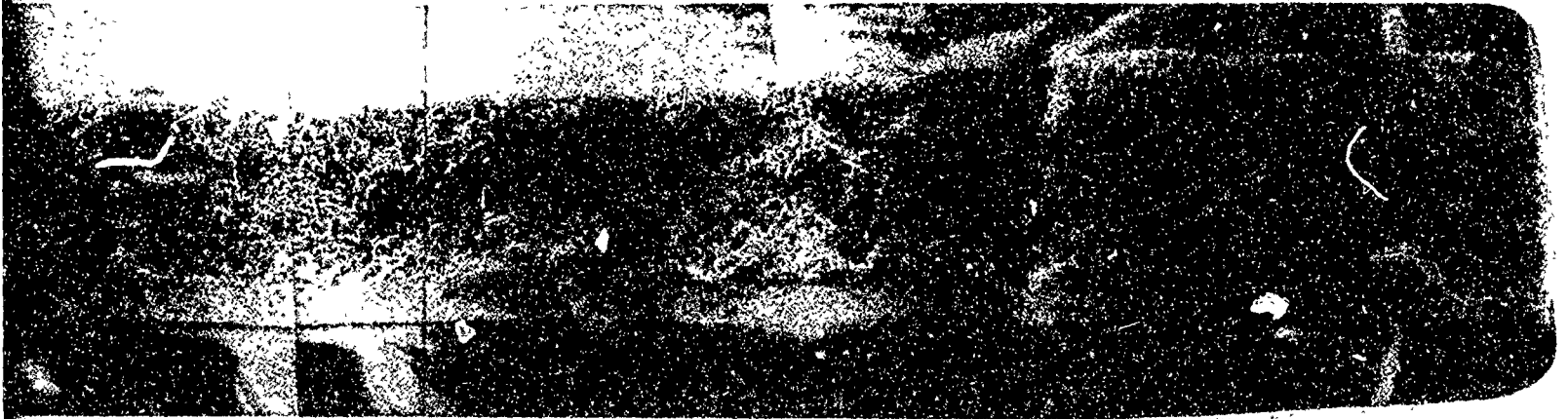
UNIAXIAL SPECIMEN TESTED IN WITH-GRAIN (w.g.) TENSION

S.E.M. VIEWS OF ATJ-S FRACTURES — 70°F TESTS

Figure 23. SEM Views of ATJ-S Fractures (70°F Tests)

C

45

may be adequate), and of the same general appearance and size as in the smoother regions of the uniaxial specimen surface. Additional viewings at higher magnifications failed to reveal any obvious differences in fracture mode between the two specimens.

The effect of minimum dimensions of the gage section has been investigated experimentally for ATJ-S in a very limited effort described in Reference 2. Five ring specimens of 0.050-inch wall and five others of 0.082-inch wall (but of equal volume and radius-to-thickness ratio) were burst in hoop tension. The results showed the thinner-walled specimen to give somewhat higher strengths. Similar results were mentioned in Reference 9 for 0.040-inch thick and 0.080-inch thick rings of ATJ graphite. Although it is not understood why the thinner wall gave higher strengths, these results do suggest that reducing the minimum gage dimensions to 0.050-inch should not cause any striking deleterious effects.

However, a theoretical case can be based on "fracture mechanics" to show that a difference in measured strengths should exist between thin-wall biaxial tube specimens and 0.25 diameter rods. It appears widely accepted, at least as a working hypothesis, that tensile fracture of graphite occurs by the rapid propagation of cracks from a flawed, weakened, or precracked region in the specimen, and that the size of this region, or flaw, at the time of fracture can be related to the fracture stress using the concepts of linear fracture mechanics (References 10, 11, 12 and 13 for example). Fracture mechanics concepts include "free-surface magnification" factors to describe the increase in stress intensity caused by the proximity of a flaw to a surface (see Reference 14, for example). In the biaxial tube specimen, if the size of typical fracture-causing flaws is an appreciable fraction of the wall thickness, free-surface effects can be expected to affect the measured tensile strengths.

Preceding page blank

47

The nomenclature used here to describe a flaw in a thin wall is shown in Figure 24. For a linearly elastic material, the tensile stress at fracture is related to the flaw and specimen geometries by (Ref 14):

$$\sigma = \frac{K_{IC}\,\phi}{M_1 M_2 \sqrt{\pi a}}$$

where

K_{IC} = critical stress intensity (or fracture toughness) of the material

ϕ = factor expressing the shape of the flaw

M_1 = front-face free-surface magnification factor

M_2 = back-face free-surface magnification factor

a = flaw depth

To obtain a rough estimate of wall thickness effects, assume that the typical flaw in ATJ-S graphite is a circular region of radius a^*. This typical radius may be estimated from the average tensile strength, $\bar{\sigma}$, of relatively large specimens:

$$\bar{\sigma}\,\sqrt{\pi a^*} = \phi K_{IC}$$

For a circular flaw $\phi = 2.4$ (Ref 14). Taking K_{IC} for ATJ-S graphite as approximately 750 ksi$\sqrt{in}$ (References 11 and 13) and $\bar{\sigma}$ as approximately 5 ksi, the critical circular flaw radius is found to be approximately:

$$a^* = 0.018 \text{ inch}$$

Figure 25 shows various possible placements of such a critical flaw relative to the surfaces of a "massive" (say a 0.25-inch diameter rod) specimen, and a thin-wall (0.050-inch) biaxial specimen. Some free-surface magnification factors may be estimated using the results presented in Reference 14 for semi-circular flaws. The front-face magnification reaches a maximum of about

48

NOTE: PLANE OF FLAW ASSUMED
PERPENDICULAR TO APPLIED
TENSILE STRESS
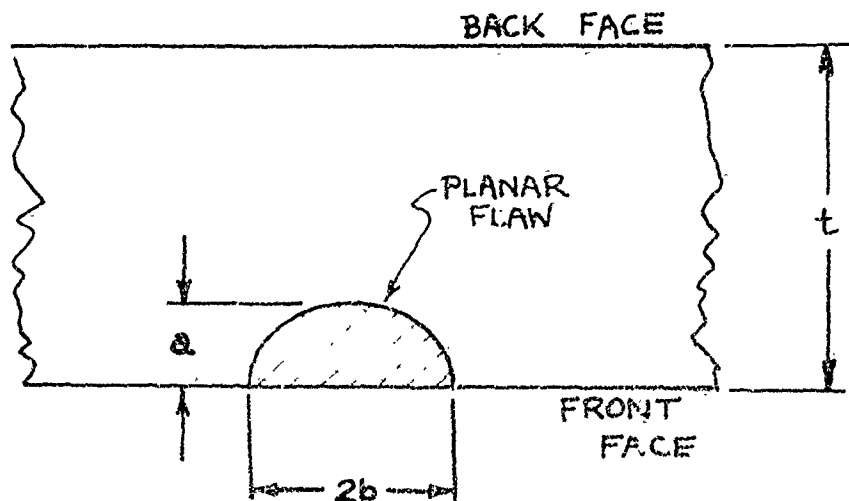
Figure 24.   Flaw Nomenclature
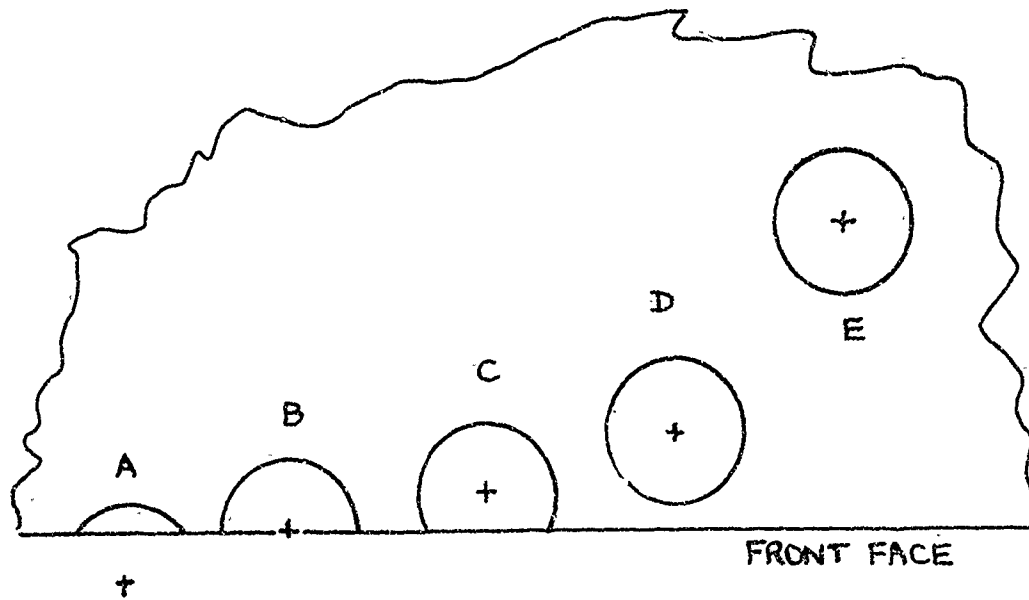
MASSIVE SPECIMEN
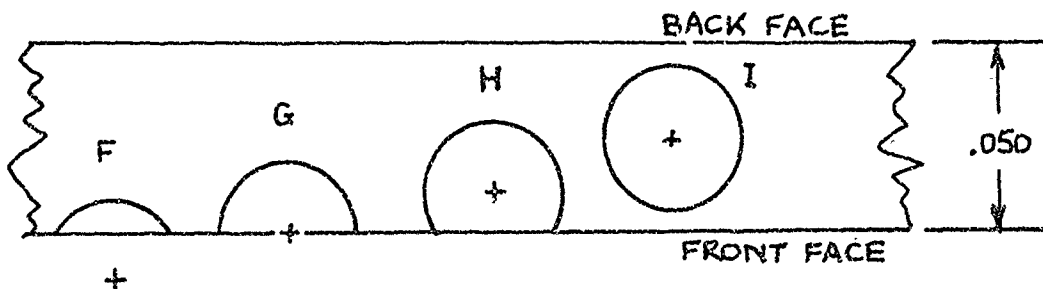
THIN-WALL SPECIMEN
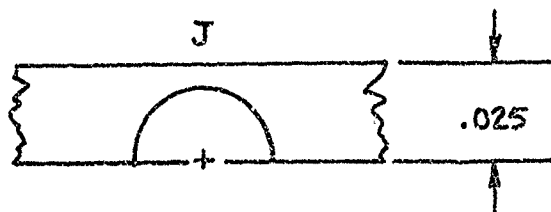
SITUATION ASSUMED FOR ESTIMATING
MAXIMUM BACK-FACE MAGNIFICATION

Figure 25. Some Possible Flaw Situations

twenty-one percent (M_1 = 1.21) for the semi-circular surface flaw (situations B and G in Figure 25). The maximum back-face magnification effect, as estimated for situation I in Figure 25 (from a solution for the extreme situation shown as J in Figure 25), is approximately five percent. For flaw placement G, the back-face magnification is less than one percent.

Because even the most massive specimen has a surface, front-face magnification will affect the measured strength. However, a solid-rod specimen may tend to give higher measured strengths (than a thin-wall tube of equal volume) because only a small proportion of inherent flaws will lie near the surface. For example, in the 0.050-inch wall biaxial specimen, 72 percent of the gage-section volume lies within 0.018 inches (the critical flaw radius) of the surface; whereas in a 0.25-diameter tensile bar, only 14 percent of the specimen volume is within 0.018 inches of the surface. Furthermore, the biaxial tube has about 8 times the surface area of the 0.25-inch diameter tensile specimen (Table III). Therefore, because of the increased probability of front-face magnification effects biaxial specimens should tend to give lower average measured strengths than do the tensile rods.

3.5 CONCLUSIONS

The discussions in the preceding subsections lead to the following conclusions:

A. Stress-strain responses measured in uniaxial tension with biaxial specimens at room temperature are essentially the same, within normal experimental errors, to those measured with uniaxial specimens. For the case of with-grain stress-strain response, the hoop stress estimated at the outer surface of the specimen, where the strains are measured, should be used. A good estimate of the outer-surface hoop stress is:

$$\sigma_{H_o} = 0.96 \frac{Pr_i}{r_o - r_i}$$

B.   The strain measurements obtained at elevated temperature are
     subject to relatively large experimental uncertainties, related
     primarily to the optical extensometry techniques used. When these
     uncertainties are considered together with the potentially
     significant effect on stress, at low stress levels, of the metal
     foil bladder used, it appears that the stress-strain responses
     measured on biaxial specimens at 2000°F may be of marginal quanti-
     tative value.

C.   Average uniaxial tensile strengths measured on biaxial specimens
     tend to be lower than average strength obtained with uniaxial
     specimens (Table III). Some of the discrepancy may be attributed
     to the experimental factors listed in Table IV. However the
     influences of volume, surface area, and minimum gage dimensions
     (0.050-inch in the case of the biaxial specimen) may also be
     significant. Available information on graphite implies that the
     greater biaxial specimen volume might account for a three percent
     decrease in strength. Available information on gage dimension
     effects is inconclusive but suggests the net effect is small.

D.   The brief fracture-mechanics analysis presented at the end of
     Section 3.4 suggests that:

     1.   fracture strengths measured on specimens with highly-stressed
          free surfaces may be lower than the fracture strength within
          a solid body of graphite (e.g., an externally heated thermally
          stressed block) because stress intensities are magnified at
          flaws near surfaces.

     2.   surface area may play a role independent of volume in the
          fracture of brittle materials even in the absence of
          externally-caused surface damage.

     3.   the greater surface area of biaxial tube specimens may be a
          significant factor contributing to their lower strengths
          relative to uniaxial specimen tests.

E. Hoop (with-grain) strains measured in biaxial fracture tests must
be increased by more than ten percent to provide an estimate of the
maximum hoop strain experienced by the biaxial specimen
(Section 3.2). The calculated magnitude of the strain gradient
depends on the constitutive law assumed for ATJ-S. A reasonable
estimate of the ratio of maximum hoop strain to measured hoop strain,
over the range of biaxial stress states tested, is 1.12. This ratio
has been applied to the hoop strains measured in biaxial fracture
tests at room temperature (References 1, 2 and 3) to obtain the new
summary plot of Figure 26.

F. Hoop stresses are subject to less uncertainties than hoop strains
because the stress gradients within a specimen are smaller than the
strain gradients and because, especially at elevated temperature,
the experimental uncertainties in strain measurement appear to be
greater. Based on the analyses described in Section 3.2, a
reasonable estimate of the ratio of maximum hoop stress at fracture
is 1.04 times the mean hoop stress calculated from the thin-wall
cylinder formula. In References 1, 2 and 3, the mean hoop stress
was used in the presentation of fracture data. A new summary plot
of 70°F biaxial fracture stress data, in which the hoop stresses
shown are 1.04 times the mean hoop stress, is presented in
Figure 27.
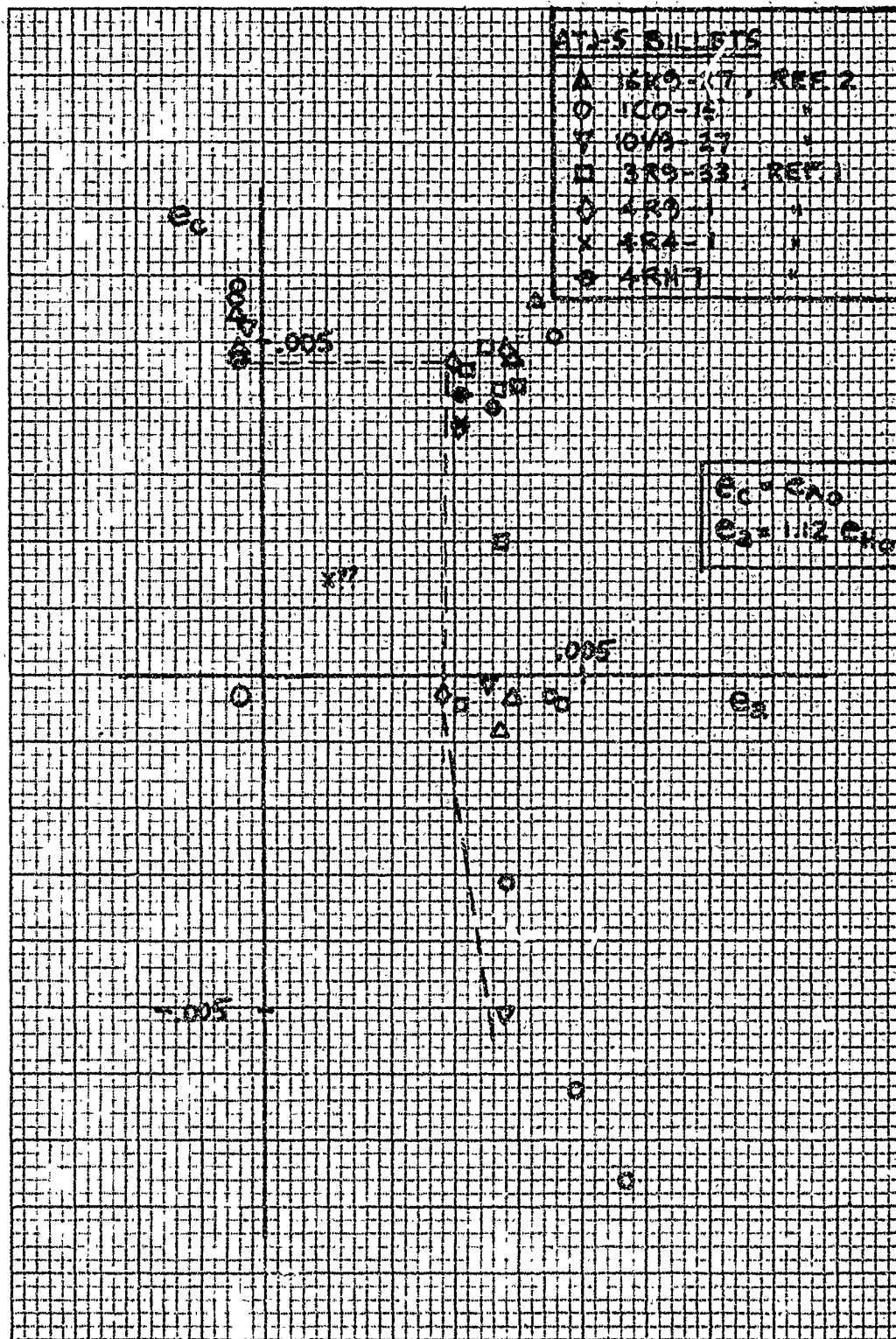
Figure 26. Biaxial Failure Strains at 70°F (ATJ-S)
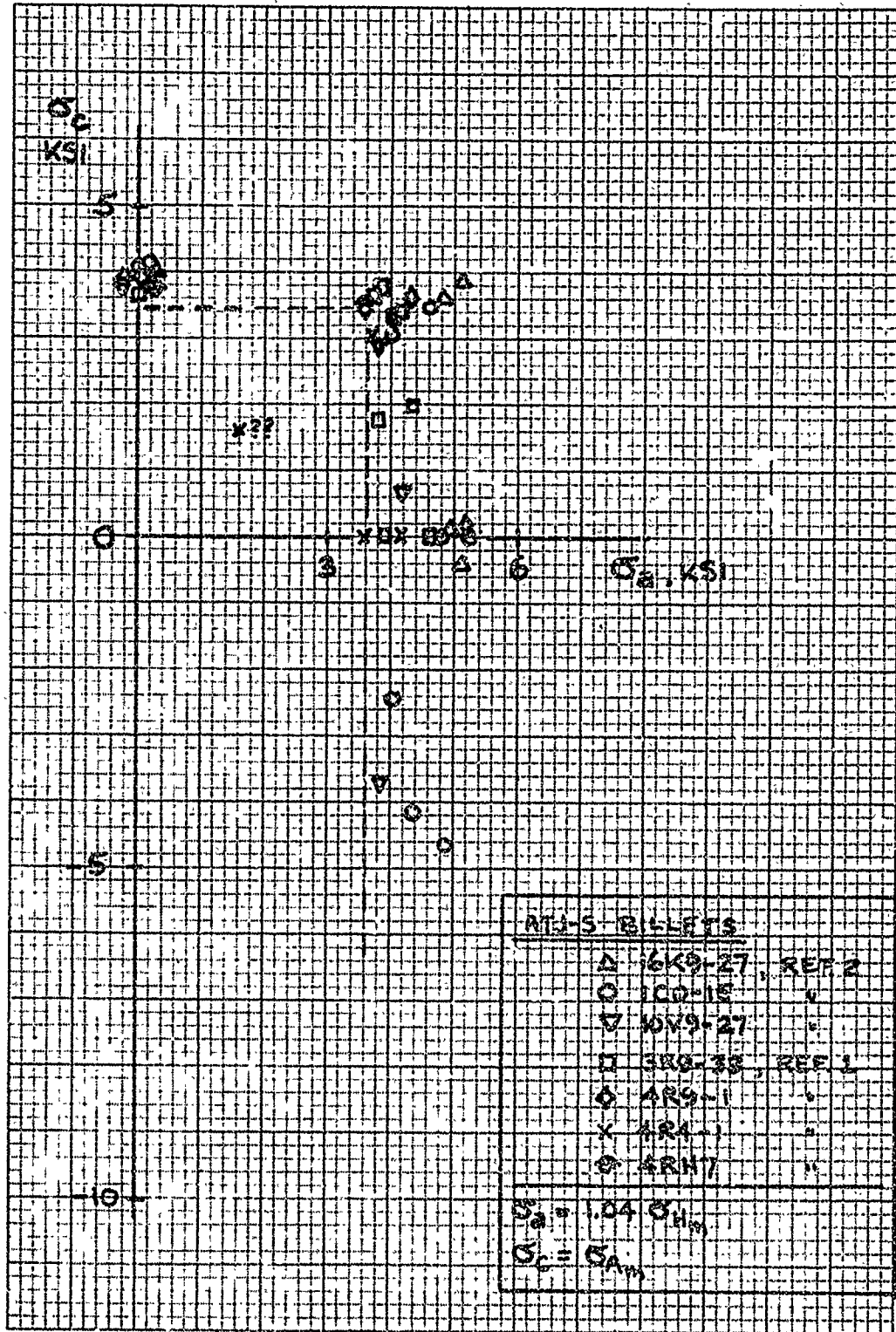
Figure 27. Biaxial Failure Stresses at 70°F (ATJ-S)

Section 4
BIAXIAL TESTS AT 2000°F

Biaxial fracture data for ATJ-S at 2000°F has been presented in Reference 2. However, the relatively small number of tests, the scatter in the data, and the fact that some graphite structural components are expected to experience a maximum risk of fracture at elevated temperature, motivated further testing.

All specimens tested at 2000°F in the current program were obtained from ATJ-S Billet 21R1-6. Based on the bulk density, acoustic velocity, X-ray, and ultrasonic pulse-echo information described in Section 2, the billet appeared to have no unusual features. In addition to these non-destructive measures, uniaxial specimens of the type shown in Figure 17, were tested at 70°F and 2000°F with the results summarized in Table V and Figure 28.

The biaxial specimens were machined to the dimensions shown in Figure 4. The test techniques were those described in Section 3.1. The fracture results are summarized in Table VI; Figure 29 is a plot of the fracture stresses. Figure 30 shows the strains-at-fracture. Also shown in Figures 29 and 30 are the uniaxial rod data from Table V.

The with-grain stresses and strains shown in the graphs presented in this section were obtained as follows:-

$$\sigma_a = 1.04 \ \sigma_{Hm}$$

$$e_a = 1.12 \ e_{Ho}$$

That is, they represent the values estimated to have existed at the inner surface of the mid-length gage section (see Sections 3.1, 3.2 and 3.5).

57

TABLE V

TENSILE CHARACTERIZATION OF ATJ-S GRAPHITE BILLET 21R1-6

TEST TEMP °F	LOAD AXIS	SPECIMEN NO. (1) (2)	YOUNG'S MODULUS 10^6 PSI	FRACTURE DATA	
				STRESS PSI	STRAIN (3) IN/IN
70	AG	101	0.9	4070	0.0064
		102	0.8	3920	0.0066
		105	0.8	3950	0.0068
		110	1.0	4050	0.0064
	WG	A	1.5	5170	0.0053
		C	1.4	4520	0.0045
		F	1.4	5150	0.0052
		H	1.6	5050	0.0047
2000	AG	106	1.1	4680	0.0050
		107	1.1	4870	0.0051
		113	1.1	5190	0.0059
		114	1.2	4730	0.0055
	WG	B	1.8	6010	0.0041
		D	1.9	6040	0.0039
		E	1.9	5680	0.0039
		G	1.9	6190	0.0042

NOTES: (1) Specimens were of standard design (Figure 17).

(2) Specimen numbers refer to locations within billet, Figure 1

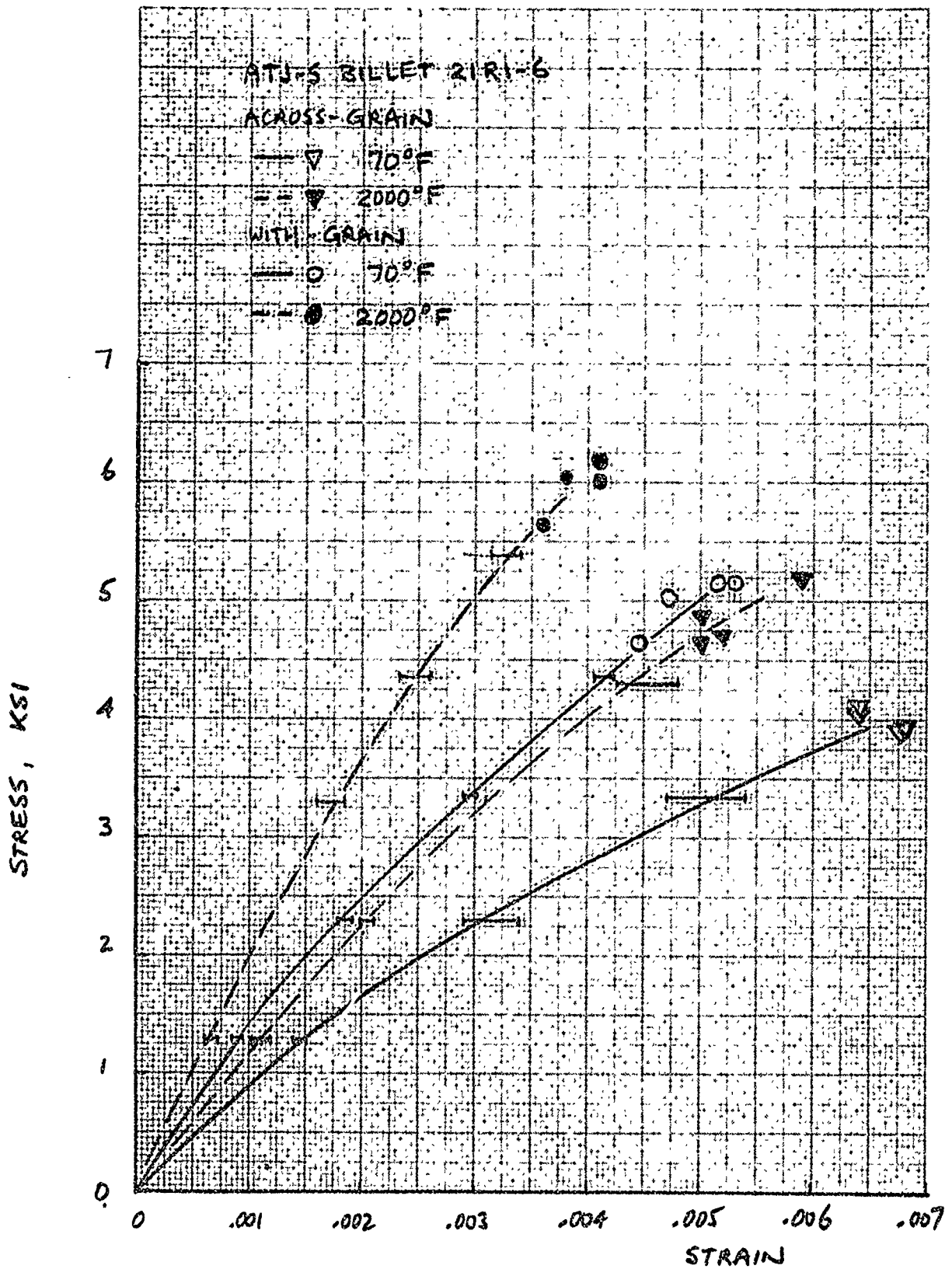(3) Strains were measured optically at both 70°F and 2000°F over a one-inch gage length.

Figure 28. Uniaxial Tension Data From Billet 21R1-6

TABLE VI

SUMMARY OF BIAXIAL FRACTURE DATA – ATJ-S BILLET 21R1-6 AT 2000°F

NOMINAL STRESS STATE $\sigma_A : \sigma_H$	SPECIMEN NUMBER	AXIAL STRESS PSI	CONDITIONS AT FRACTURE				
			MEAN HOOP STRESS(1) PSI	MAXIMUM HOOP STRESS(2) PSI	MEASURED AXIAL STRAIN	MEASURED HOOP STRAIN	MAXIMUM HOOP STRAIN(3)
1:0	103	4500(4)	---	---	0.0044	n.d.	---
	113	4890	---	---	0.0045	n.d.	---
	114	4760	---	---	0.0044	n.d.	---
2:1	105	4040(5)	2050	2130	0.0039	n.d.	---
	107	4000	2030	2110	0.0032	0.0008	0.0009
	109	4600	2310	2400	0.0042	0.0011	0.0013
	112	4520	2310	2400	0.0035	0.0012	0.0014
1.1:1	102	4140	3930	4010	0.0043	0.0018	0.0020
1:1	106	4130	4310	4500	0.0037	0.0023	0.0026
	110	3470	3680	3830	0.0035	0.0021	0.0024
0.7:1	108	4100	5670	5900	n.d.	n.d.	---
	116	3500	4930	5130	0.0025	0.0032	0.0036
0.5:1	101	2110	4450	4630	0.0018	0.0026	0.0029
	111	2350	4940	5140	0.0025	0.0028	0.0031
0:1	104	172	5400	5620	-0.0006	0.0031	0.0035

NOTES:
(1) Mean hoop stress calculated from "thin-wall" formula.
(2) Maximum hoop stress is estimated to be 4 percent greater than mean hoop stress (See Section 3.2).
(3) Maximum hoop strain is estimated to be 12 percent greater than measured (outer-surface) hoop strain. (See Section 3.2).
(4) Specimen 103 was scratched in handling prior to test and failed at the scratch.
(5) Specimen 105 was found to have a defect, approximately 0.025-inch in major dimension, on its fracture face at the fracture origin (See Figure 33).
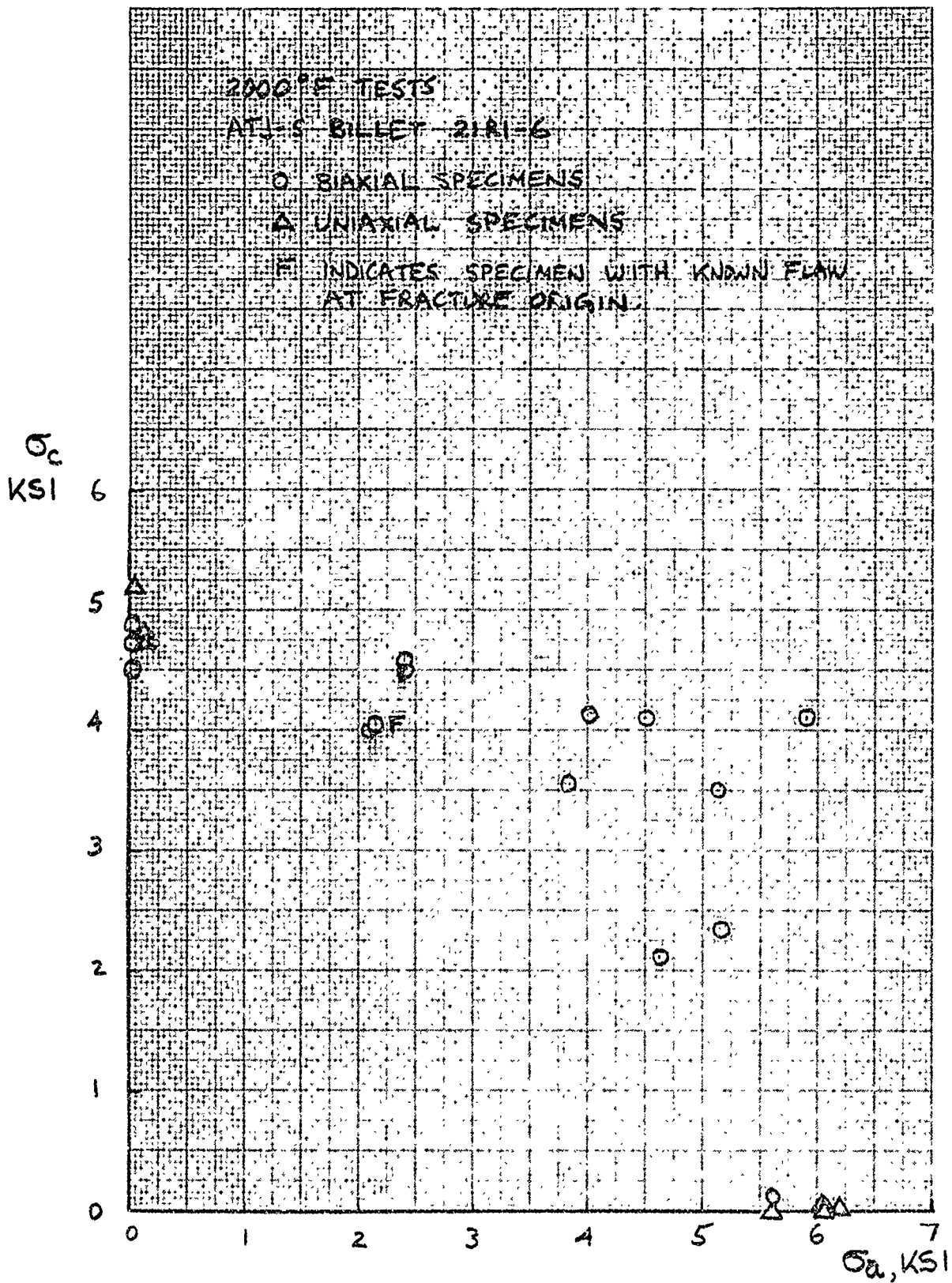
60

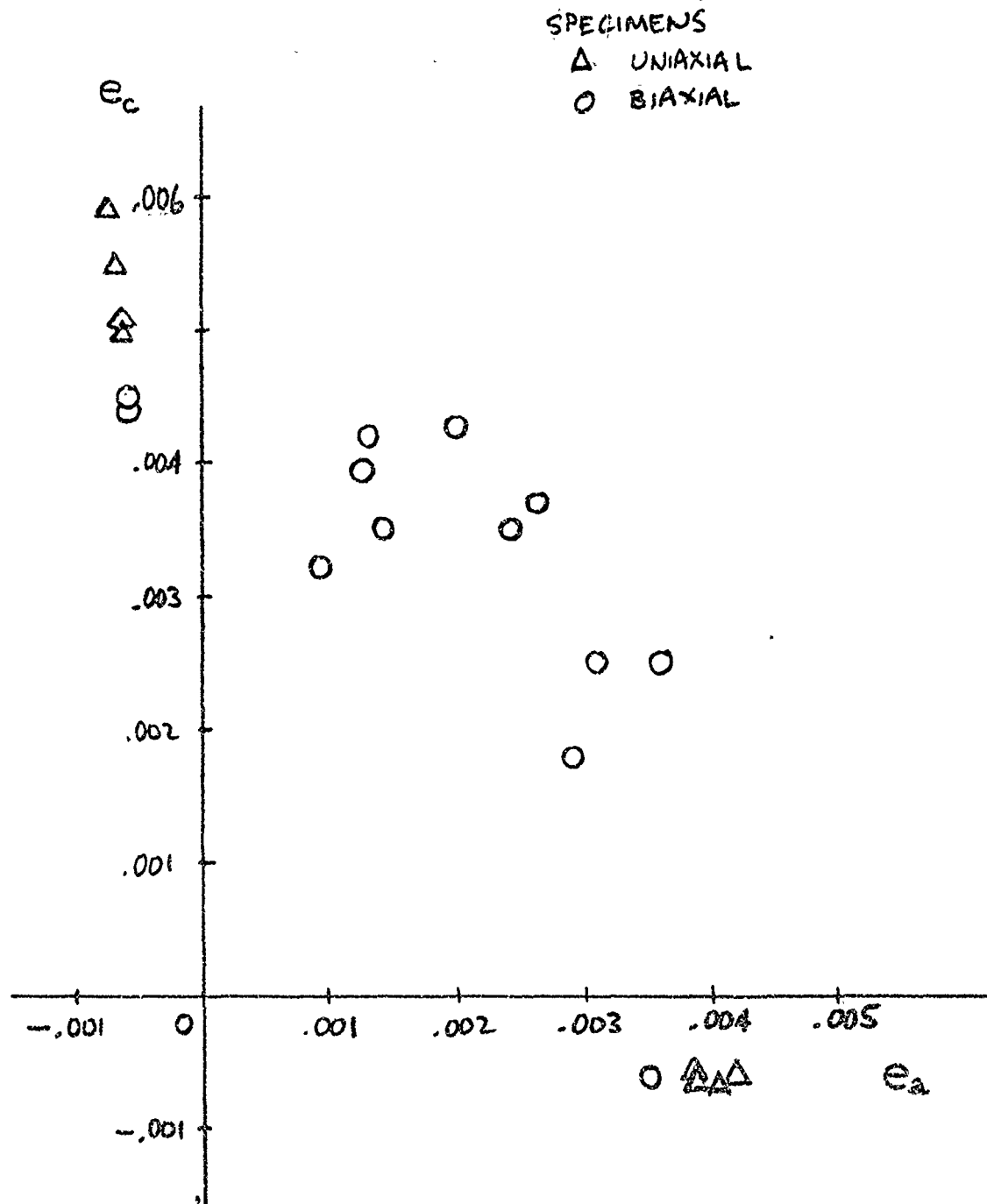Figure 29.   Biaxial Strengths at 2000°F, ATJ-S Billet 21R1-6

Figure 30. Strains at Failure in Biaxial Tension at 2000°F,
ATJ-S Billet 21R1-6

Figure 30 shows the strains-to-failure in across-grain uniaxial tension measured with the biaxial specimens to be significantly lower than those obtained with uniaxial specimens even though the measured across-grain strengths (Figure 29) do not differ greatly. Figure 31 shows that the biaxial specimen tests provided appreciably stiffer across-grain stress-strain response than the uniaxial specimen tests. The reasons for a discrepancy of the magnitude shown are not understood; the possibility of human error in conducting the strain measurements cannot be dismissed. The with-grain stress-strain responses for both types of specimens show good agreement (Figure 32).

In the course of the test program it seemed that many of the specimens were failing at rather low stress levels. In most cases reconstruction of the specimen to determine the origin of fracture (by following the crack bifurcation pattern) was prohibitively difficult because the biaxial specimens tend to shatter into many small pieces under the energy of the pressurizing gas (see specimen photos in Reference 2). However, one of the specimens, tested in the 2:1 axial-to-hoop stress state, was successfully reconstructed. At the fracture surface of this specimen, an anomalously large inclusion about 0.025-inch in major dimension (Figure 33) was found. Electron microprobe scanning failed to reveal any difference in atomic composition between the inclusion and the surrounding graphite. Flaws of similar morphology have been noted recently in other ATJ-S billets (References 24 and 25).

After finding the inclusion, the six remaining specimens were inspected by X-ray radiography prior to testing. No anomalies were discovered in the radiographs; however X-ray radiography is not an appropriate tool for discriminating a carbon particle within a carbon body. No other specimens were successfully reconstructed to the extent necessary to identify the fracture origin.

When the fracture data from billet 21R1-6 is compared to that reported in Reference 2, as in Figure 34, it is seen that billet 21R1-6 tends to have strengths equivalent to billet 1C0-15 and somewhat lower than billet 16K9-27. The biaxial strains at failure are compared in Figure 35. It seems that
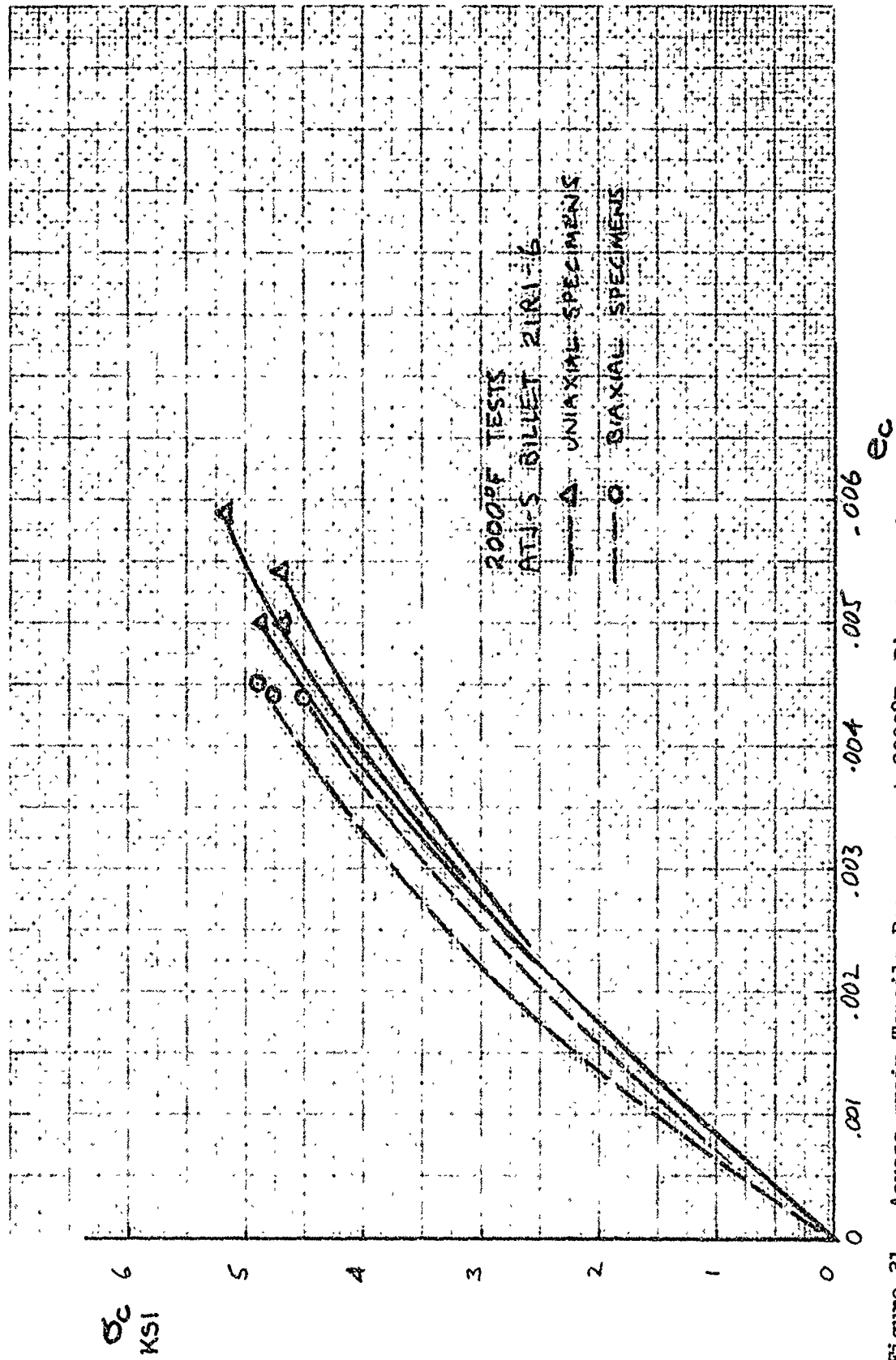
Figure 31. Across-grain Tensile Responses at 2000°F, Biaxial and Uniaxial Specimens

64
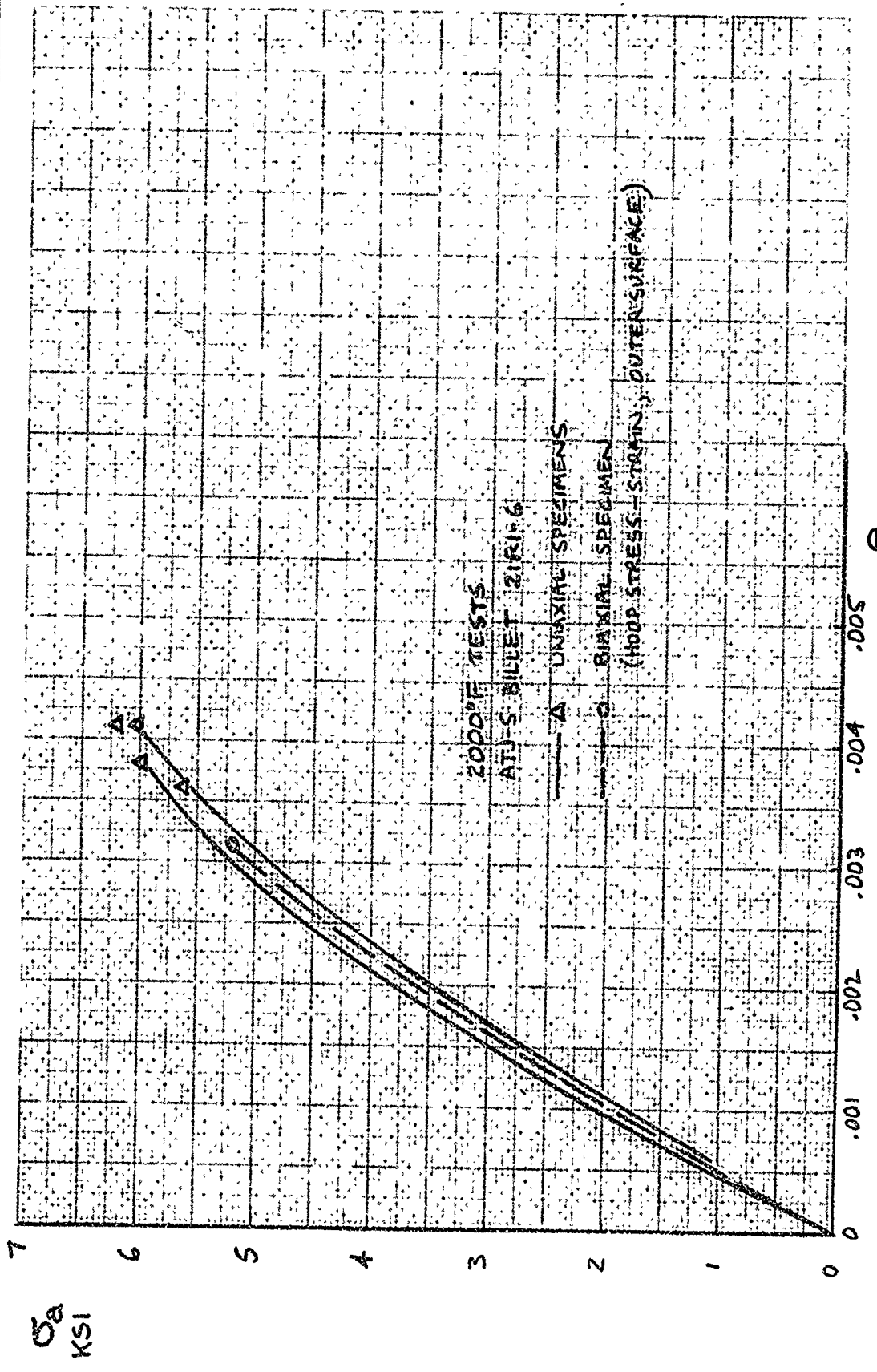
Figure 32. With-grain Tensile Responses at 2000°F, Biaxial and Uniaxial Specimens

65
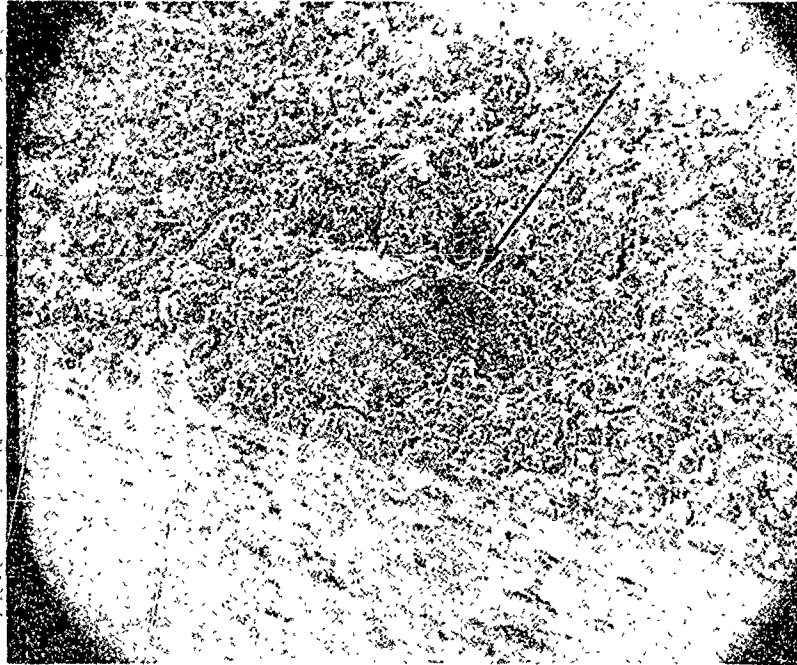
53X

Figure 33. Inclusion Found at Fracture Origin of Biaxial Specimen 105
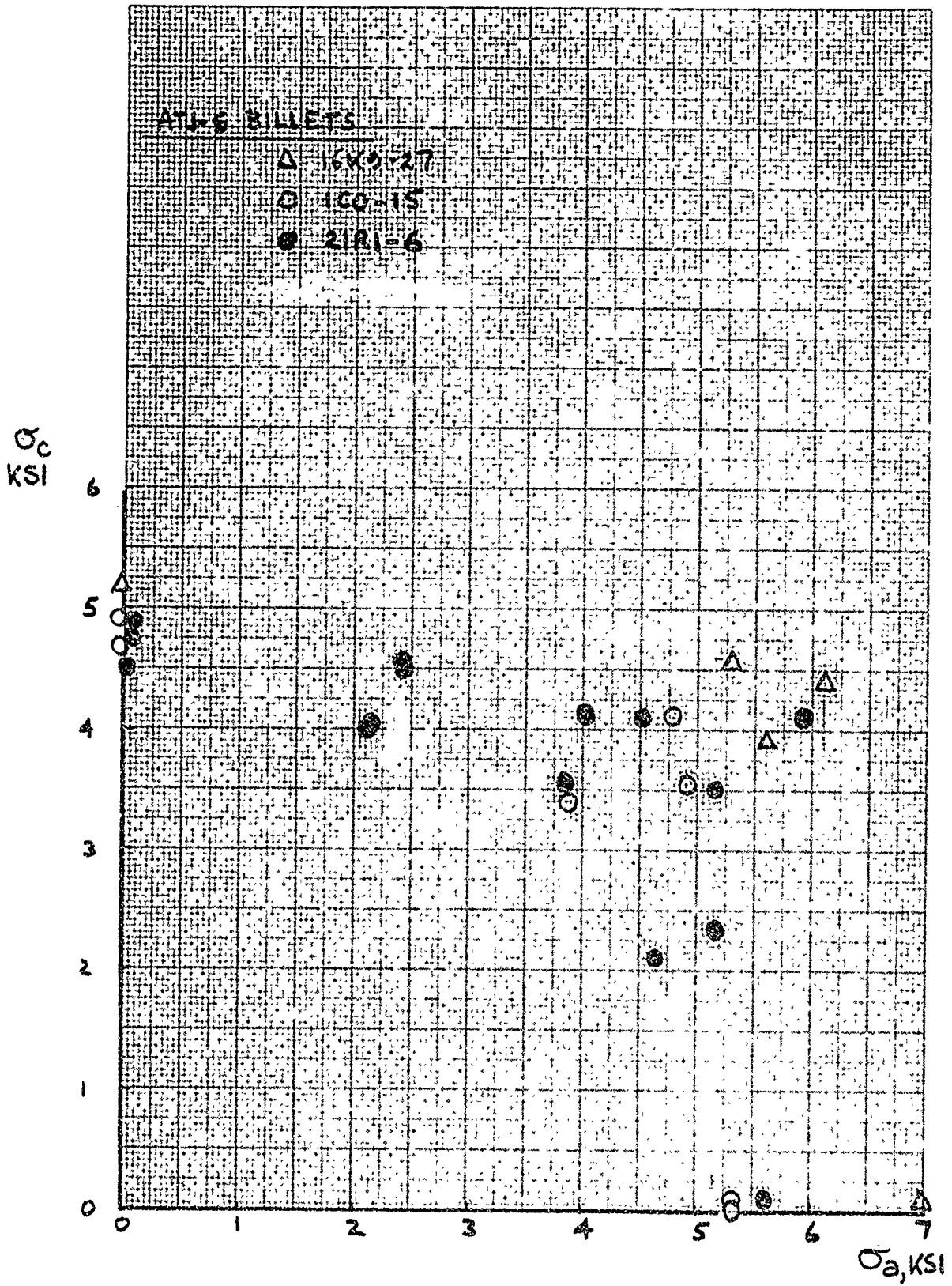
Figure 34. Summary of 2000°F Biaxial Strength Data
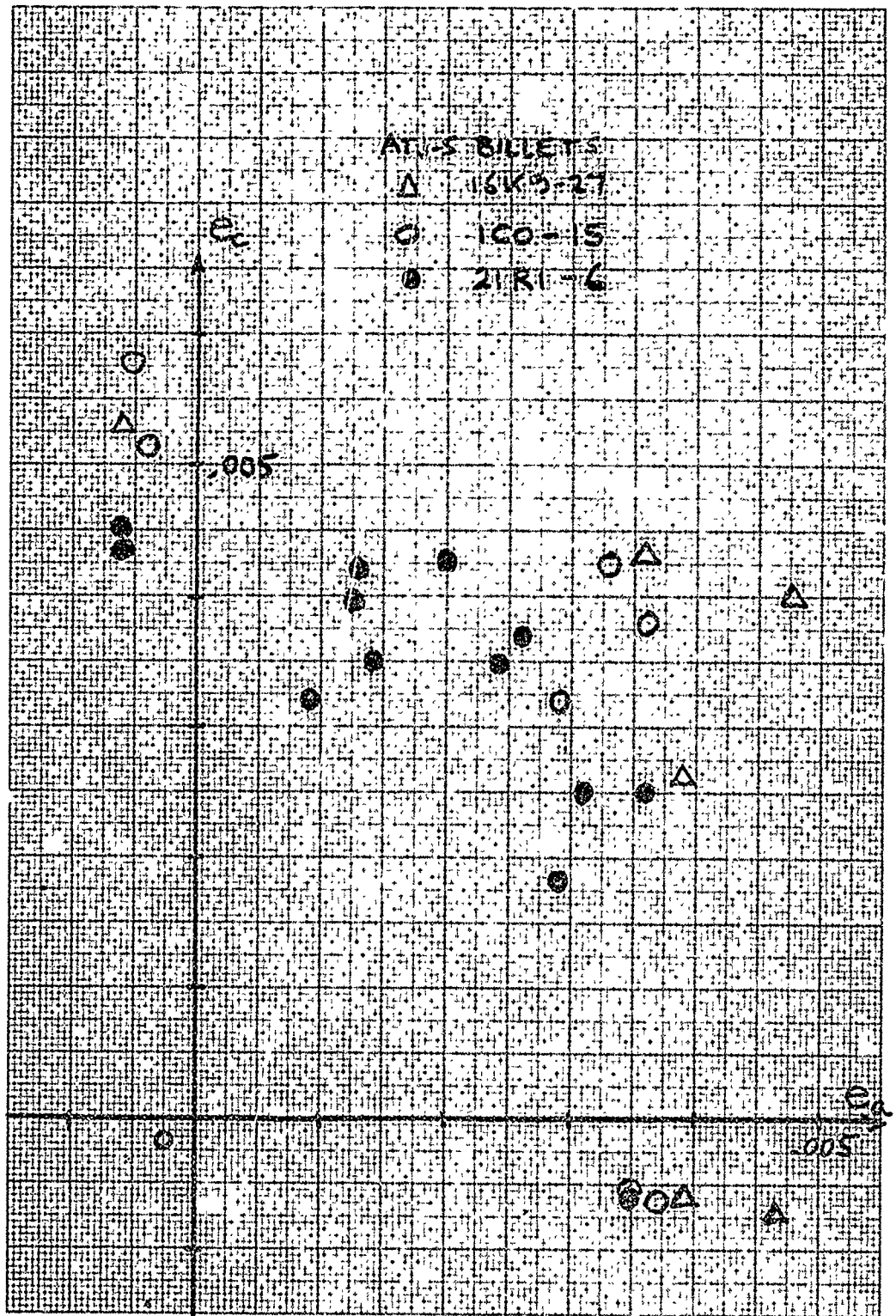
Figure 35. Summary of 2000°F Biaxial Failure Strain Data

billet 21R1-6 tends to provide lower strains-to-failure; however the lesser accuracy of the strain data (see Table IV) and the aforementioned discrepancy in across-grain strains (Figure 31) should be kept in mind.

The presence of the inclusion in one specimen clouds the significance of the fracture data. It is not known whether other specimens failed under the influence of similar inclusions. The available strength data (Figure 34) do show more of a strength reduction in biaxial tension (relative to uniaxial strength) at 2000°F than was observed at room temperatures (Figure 27). The failure strain data at 2000°F (Figures 30 and 35) also show a greater reduction in biaxial tension than was observed at room temperature (Figure 26). Unfortunately, because of a lack of definitive information, there is no basis for attributing these deleterious biaxial effects to the use of flawed specimens. Therefore, caution should be exercised in designing graphite components for use in multiaxial-tension stress states at elevated temperature.

Section 5
TRIAXIAL DEFORMATION STUDIES

The stress-strain behavior of ATJ-S graphite under some triaxial stress states was measured at room temperature. The major objectives were:

A. To provide triaxial stress-strain data that might aid in the formulation of better constitutive laws.

B. To analyze the triaxial stress-strain data to help define the shape of yield surfaces for ATJ-S and to judge the applicability of the associated flow rule.

Most of the experiments were conducted under monotonically increasing stress levels with ratios of principal stresses maintained approximately constant (approximately "proportional" or "radial" loading). Thus the results were analyzed within the restrictions of deformation theory (as opposed to incremental plasticity theory). However, some exploratory tests were also conducted under non-proportional load paths to give some insight into load path effects.

5.1 BACKGROUND

The uniaxial stress-strain curves for polycrystalline graphites are non-linear and of a form reminiscent of the stress-strain curves of some elasto-plastic metals. While linear elastic stress analysis sometimes is still applied to graphite components, the trend in the aerospace industry has been towards using non-linear constitutive equations to better model the behavior of graphite. For example, the methods described in References 15, 16 and 17 treat orthotropic materials with non-linear stress-strain responses. The constitutive equations used appear to be derived from the classical work on plasticity in metals (for example, Reference 18).

Preceding page blank

o facilitate further discussion, and to introduce the terminology used in this report, some of the concepts of classical plasticity are described below:

A. <u>Plastic Strain</u> - The "plastic" strain components are usually defined as:

$$e_{ij}^{P} = e_{ij} - e_{ij}^{E}$$

where e_{ij} is the total strain and e_{ij}^{E} is the "elastic" strain. The elastic strain components are related to the stresses by the generalized Hooke's law (Reference 19 for example). The plastic strain components are derived with the aid of the concepts described below.

B. <u>Effective-stress Function</u> - The effective-stress function is also referred to as the <u>yield function</u>. It is usually taken as a scalar function of the applied stresses:

$$\overline{\sigma} = \hat{f}(\sigma_{ij})$$

When the locus of a specific value of $\overline{\sigma}$ is plotted in principal-stress space, the resulting surface is referred to as a <u>yield surface</u>. The assumption that the effective-stress function depends only on the curr .t value of the stress components, and retains the same form (with c...stant coefficients) as loading proceeds, results in a family of geometrically-similar nested yield surfaces each corresponding to a different value of ..'fect've stres.. This situation is sometimes referred to as <u>isotropic strain-hardening</u> (Reference 20).

C. <u>Generalized Plastic Stress-Strain Relationship</u> - Usually an effective strain function, a scalar function of the plastic strain components, is defined and is assumed to be related to the effective stress by an effective-stress/effective-strain curve. The effective-stress/

72

effective-strain curve, known as the generalized plastic stress-strain relationship, is usually derived from uniaxial stress-strain data. The mathematical formulation of the effective-strain increment

$$d\overline{e} = g(de_{ij}^P)$$

is usually derived from the effective stress equation and the plastic work equation:

$$\overline{\sigma}d\overline{e} = dW^P \equiv \sum \sigma_{ij}de_{ij}^P$$

When the simpler deformation theory is used, the effective strain can be formulated directly in terms of the strain components:

$$\overline{e} = h(e_{ij}^P)$$

and the formulation usually is also derived from work equations such as:

$$\overline{\sigma}\,\overline{e} = W^P \equiv \sum \sigma_{ij}e_{ij}^P$$

or

$$\int \overline{\sigma}d\overline{e} = W^P \equiv \sum \int \sigma_{ij}de_{ij}^P$$

where the integration is restricted to proportional-loading stress paths.

D. <u>Flow Rule</u> – The effective-stress formula and the generalized plastic stress-strain relationship permit the determination of the effective-strain (or, in incremental theory, the effective strain increment) from a knowledge of the stress components. At this point, a flow .rule is required to determine which one of the possible sets of plastic strain components (or plastic strain increment components) that result in that value of effective strain (or effective-strain increment) is appropriate. A flow rule that appears to have theoretical justification (see Reference 21 for example) for

73

materials in which plastic deformation proceeds by dislocation slip is the "normality condition". This rule requires that the strain vector, defined as a vector in stress-space whose components are proportional in magnitude to the strain (increment) components, have a direction normal to the yield surface at the stress point being considered. Presumably because the strain vector direction is associated with the yield surface, this flow rule is often referred to as the associated flow rule.

The concepts outlined above form the basis for some of the constitutive formulations in use. For example in the methods described in References 15, 16 and 17, the effective-stress formula is a modification of the von Mises function for isotropic metals. The von Mises yield surface when plotted in principal stress space is a cylinder of circular cross-section with center-line coinciding with the hydrostatic axis. References 16 and 17 accommodate orthotropy by using Hill's (Reference 18) orthotropic yield function which, for the case where principal stresses coincide with the principal material axes, may be visualized in principal-stress space as a cylinder of elliptical cross-section with centerline coinciding with the hydrostatic axis. The associated flow rule is used in References 16 and 17, and results, when combined with the cylindrical yield surface, in the restriction that plastic flow occurs at constant volume. As Merkle (Reference 20) points out, plastic volume changes can be obtained only if the yield surfaces are not parallel to the hydrostatic stress axis.

A somewhat different approach is taken in Reference 15, where the total strain is treated directly and related to stresses by the generalized Hooke's law using "elastic" constants whose magnitudes depend on the value of an effective-stress function. This effective-stress function is also a modification of the von Mises function. In contrast to Reference 16 and 17, the equations used result generally in a non-cylindrical yield surface and do imply some plastic volume change. However as pointed out in Reference 15 itself, the constitutive formulation was selected arbitrarily "without justification' except for the fact that it reduces to the von Mises formulation for isotropic materials.

Experimental work, including that described in References 3, 26 and 27, shows that the constitutive formulations in References 15, 16 and 17 do not adequately describe the observed behavior of ATJ-S graphite. Among the observed phenomena not properly accounted for analytically are inelastic volume changes in uniaxial tension and compression, the "biaxial softening" effect in biaxial tension, inelastic volume change under equitriaxial compression, non-linear stress-strain response on unloading, differences in behavior between uniaxial tension and uniaxial compression, and the effects of pore pressure.

The existence of these "non-classical" effects is not especially surprising in view of the complex microstructure of polycrystalline graphite. Probably the most important factor, mechanistically, is the existence of pores (about 18 percent of the volume of ATJ-S). That is, the volume changes and related anomalies (biaxial softening, hydrostatic compaction, etc.) are probably due largely to stress-induced changes in the pore volume.

A mechanistic derivation of new constitutive relations for graphite based on a stress-analysis of a porous solid that includes stress concentrations, etc., around the voids appears attractive in principle. An example of this type of approach, an analysis of the effects of hydrostatic pressure on elasto-plastic solids containing closed spherical voids, is provided in Reference 22. However, extension of this type of analysis to the case of general multiaxial stress-states appears prohibitively difficult, at first glance. Another sort of difficulty relates to correctly modeling stress-induced generation of new pores, or cracks, which is probably relevant to the deformation of graphite.

A more easily implemented approach, probably, is to treat graphite as a continuum within the framework of usual plasticity theory, retaining the concepts of a yield (or effective-stress) function, a generalized effective-stress/ effective-strain relationship, and a flow rule, but modifying their mathematical description to give better correspondence between analytical predictions and observed behavior. Two such approaches are described by Merkle (Reference 20) and Weng (Reference 23).

Merkle develops equations using the incremental approach. He retains all the concepts of classical plasticity, including isotropic strain hardening and the associated flow rule, and accommodates plastic volume changes by modifying the effective-stress function. The effective-stress function he recommends for polycrystalline graphite may be represented as a set of ellipsoidal yield surfaces in stress space. Weng also uses an ellipsoidal effective-stress formula. However, he abandons the distinction between elastic and plastic strains, treating the total strain directly, and replaces the associated flow rule with a new flow rule. Weng's flow rule is simply that the ratios of principal strains do not change during proportional (constant stress ratio) loading; in other words, the strain ratios are equal to the initial elastic strain ratios. Weng's flow rule is "non-associated" in that the plastic strain vector is no longer parallel to (or associated with) the normal to the yield surface. As may be inferred from the nature of his flow rule, Weng restricts his approach to deformation theory; also, in his equations, Weng further restricts the analysis to stress states such that principal stresses are aligned with principal material axes.

Differences between tensile and compressive behavior (described in References 3, 26 and 27) are not addressed by Weng's or Merkle's approaches. However, these differences are believed small relative to the discrepancies between the actual behavior of graphite and the von Mises-based constitutive laws currently in use. Neither are the potential effects of pore pressurization in the presence of fluid pressures included in the mentioned approaches. Some effects of pore pressure have been measured on ATJ-S graphite (e.g., the hydrostatic pressure studies of Reference 3). For many applications, those which do not involve exposure of the graphite to fluid pressures greater than about 1000 psi, pore pressure effects are probably small. Although this tentative conclusion needs verification over a range of stress-states, it appears appropriate at the present time to concentrate first on the other aspects of the constitutive problem.

In both Merkle's and Weng's approaches, the yield surface is taken to be a surface of constant work. In a simplified sense, the major differences between their approaches (aside from the obvious differences arising from the

76

adoption of incremental derivations by Merkle and deformation theory by Weng)
are in the flow rules and in the definitions of plastic strain.

In the context of the preceding discussion, the motivations for the experimental work conducted in this program were to help

A. define the shape of surfaces of constant plastic work, thereby
    shedding some light on the appropriate form of the yield function;

B. determine whether the associated flow rule, or some other flow
    rule such as Weng's, best describes the behavior of ATJ-S; and

C. determine some of the consequences of treating total strain
    directly rather than splitting it into "elastic" and "plastic"
    components.

5.2 EXPERIMENTAL APPROACH

Available experimental capabilities include proportional loading and unloading,
and non-proportional loading and unloading in the uniaxial, biaxial, and
triaxial tests described in References 1, 2 and 3.

The most convenient sort of test for the study of stress-strain response is
one in which the stress-state and the strain-state can be continuously and
completely monitored. This means that all three principal strains be
measured and all three principal stresses be deducible from the imposed
loads. A uniaxial test conforms to these requirements; however, tests on
hollow cylindrical specimens (such as the biaxial tube) do not because the
radial strain in the specimen wall cannot be measured with presently available
techniques. Fortunately some of the triaxial test techniques developed under
a previous program (Reference 3) do permit multiaxial tests with complete
strain measurement. For example, a solid rod loaded axially and pressurized
externally can be instrumented with axial and transverse strain gages to
measure all three principal strains during loading. The stress states
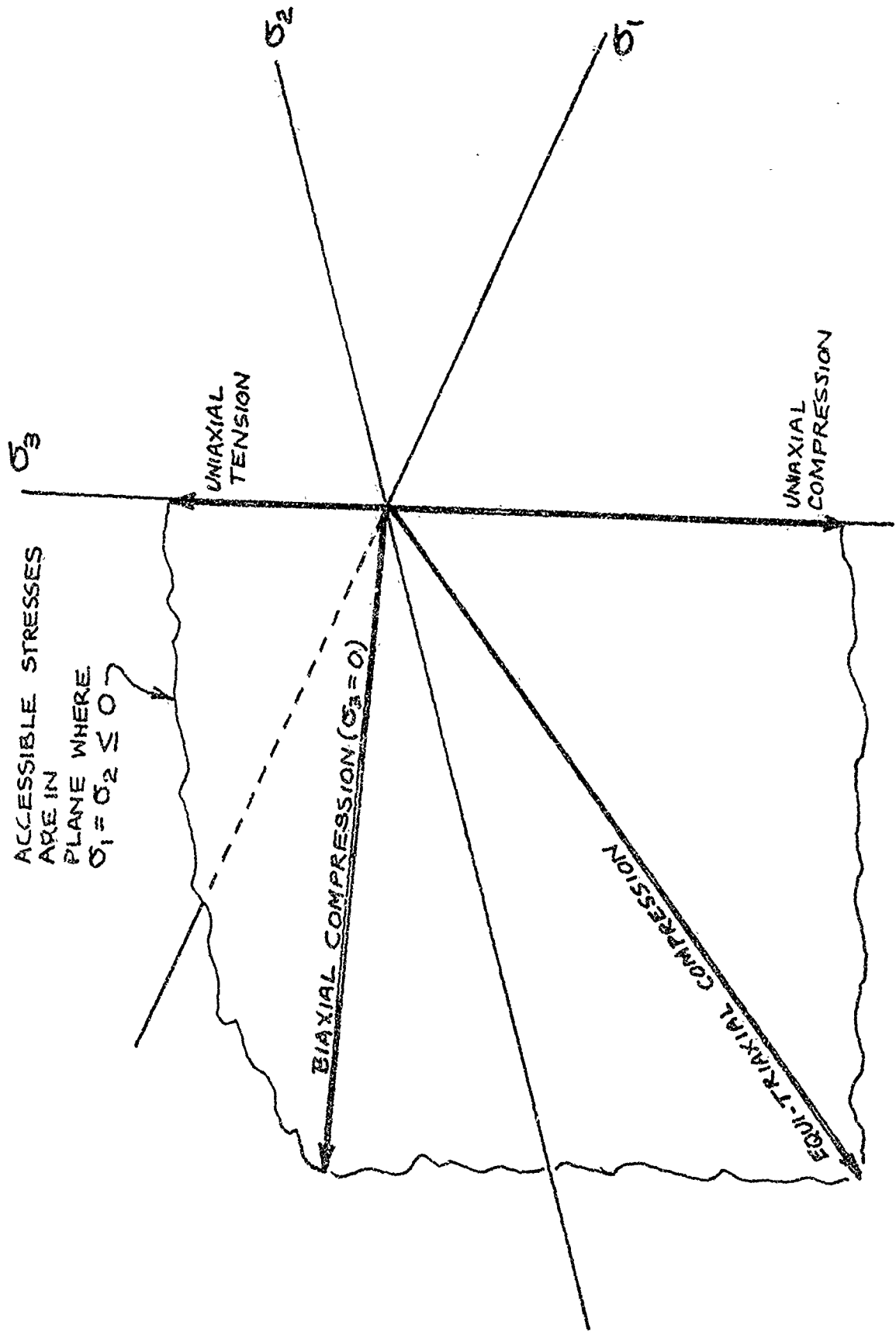attainable with such rod specimens are schematically illustrated in Figure 36.

77

Figure 36. Schematic Showing Stress States Accessible with Triaxial Rod Specimens

78

The tests actually conducted were on specimens with load axis (σ_3-direction in Figure 36) parallel to the across grain direction. That is, the load paths were in the "symmetry plane" ($\sigma_a = \sigma_b$) of on-axis principal stress space for ATJ-S graphite. Table VII lists the specimens tested (where specimen numbers refer to positions within the billet shown in Figure 2) and the stress-states achieved.

The plan was to analyze the proportional loading data as follows:

A. prepare stress-strain plots for each principal direction

B. decompose the strains into elastic and plastic components

C. integrate curves of stress vs. plastic strain to obtain plastic work as a function of stress level in each stress state

D. plot curves of equal plastic work in the symmetry plane of principal stress space; these curves represent the inter-section of the experimental yield surfaces with the symmetry plane

E. construct graphically, as in Figure 37, the curves that are normal to the plastic strain trajectories.

If the curves defined in steps (D) and (E) can be made to coincide (by adopting appropriate assumptions regarding the division of strain into elastic and plastic components) then the results would support the use of the associated flow rule. If not, the results would imply incompatibility between the associated flow rule and a work-related effective stress function.

The added tests conducted under non-proportional loading conditions (see Table VII) were exploratory in nature with no specific analytical motivation.

5.3 DESCRIPTION OF EXPERIMENTS

The triaxial test techniques have been described in Reference 3. The specimen concept, the specimen dimensions, and the loading fixture are shown in

TABLE VII

TRIAXIAL TEST MATRIX

TEST TYPE	NOMINAL STRESS-STATE RATIO $\sigma_a : \sigma_b : \sigma_c$	SPECIMEN NUMBER*	REMARKS
Proportional Loading (Results in Section 5.4)	0 : 0 : 1	73, 70	Uniaxial tension; load only.
	-1 : -1 : 2.54	81	Load and pressure applied sequentially in small increments.
	-1 : -1 : 0.99	77	
	-1 : -1 : 0.31	83	
	-1 : -1 : 0.04	79	
	-1 : -1 : -0.38	85	
	-1 : -1 : -1	71	Triaxial compression; pressure only.
	0 : 0 : -1	A1**	Uniaxial compression; load only.
	-1 : 0 : 0	W1**	
Non-proportional Loading (Results in Section 5.5)	-1 : -1 : -1	75	Load and pressure applied sequentially in small increments.
	Complex Load Path	80	Both specimens end up in same stress state after different stress histories.
	Complex Load Path	87	

* Specimen numbers refer to locations in Billet 12S1-3 (Figure 2).
** A1 and W1 are "standard" uniaxial compression specimens of 0.5-inch diameter gage section. All other specimens are triaxial rods (Figure 39).
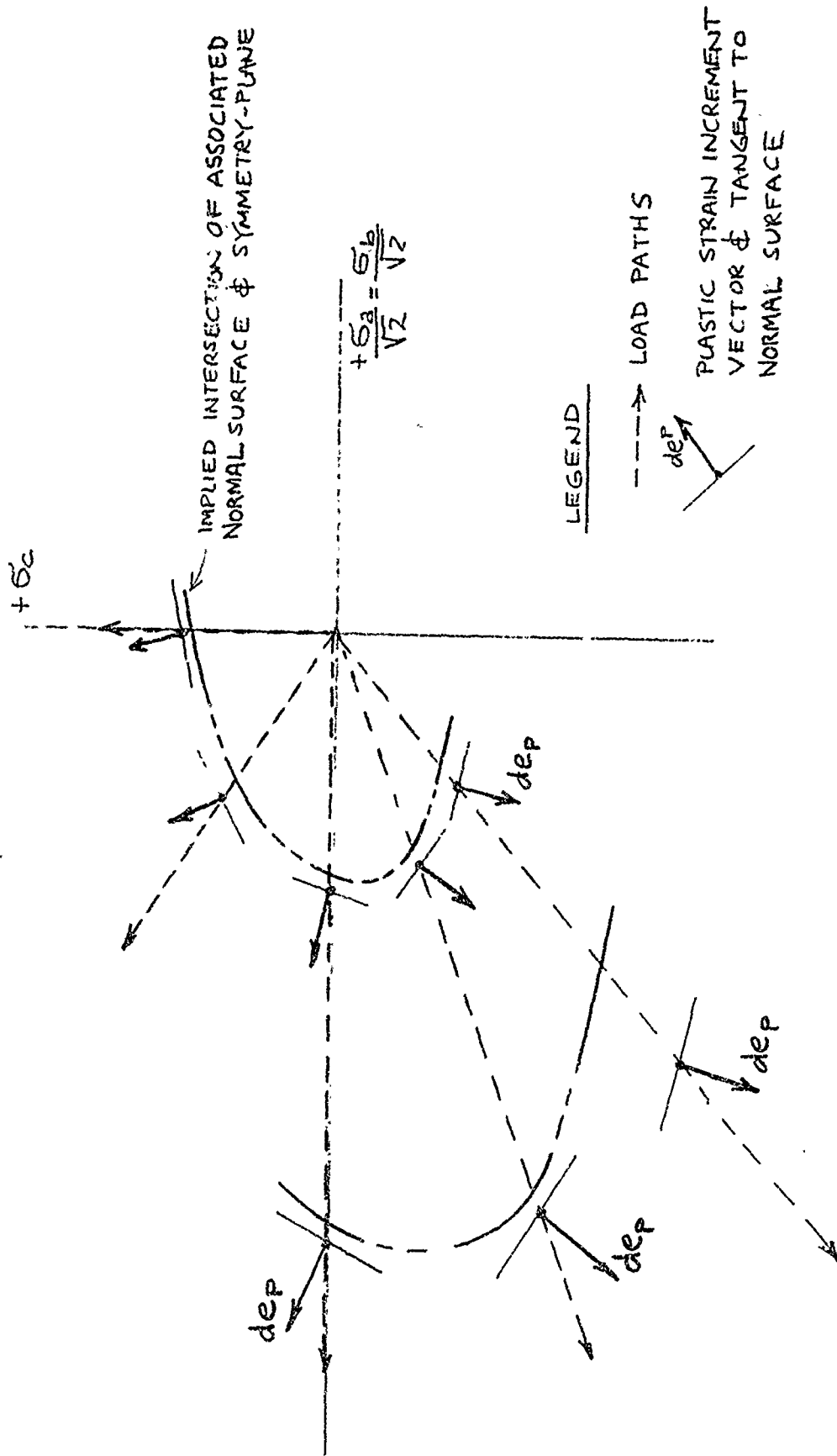
Figure 37. Schematic Showing Method of Defining Associated Normal Surface

Figure 38, 39 and 40, respectively. After being strain-gaged, the specimens were coated with a rubber compound to prevent penetration of the pressurizing fluid into the pores of the graphite. One axially-oriented and one hoop-oriented strain-gage were applied with Eastman 910 cement at the middle of the gage section of each specimen.

Pressure and axial loads were applied in the triaxial test facility at Pennsylvania State University (Figure 41). Because the facility is manually operated, with the pressure supply and load ram independently controlled, proportional loading could only be approximated (Figure 42). Load, pressure, and strain-gage outputs were recorded on Sanborn strip-chart recorders. The tests were usually terminated after the greatest measured strain exceeded 0.005 inches per inch. The test matrix has been outlined in Table VII. The data was reduced using the equations:

$$\sigma_c = \frac{L}{A} - P$$

$$\sigma_a = \sigma_b = -P$$

$$e_c = e'_c - K_t e'_a$$

$$e_a = e_b = e'_a - K_t e'_c$$

where

e' is the strain indicated by the straingage and K_t is the transverse sensitivity of the straingage.

Because of the deviations from proportional loading, the strain data was taken only from those points closest to the desired stress-state (Figure 42).
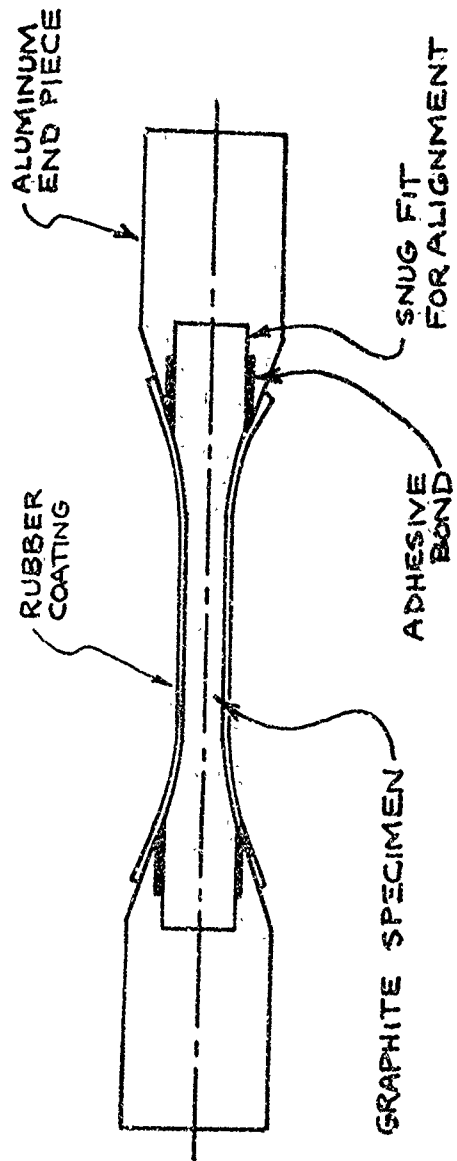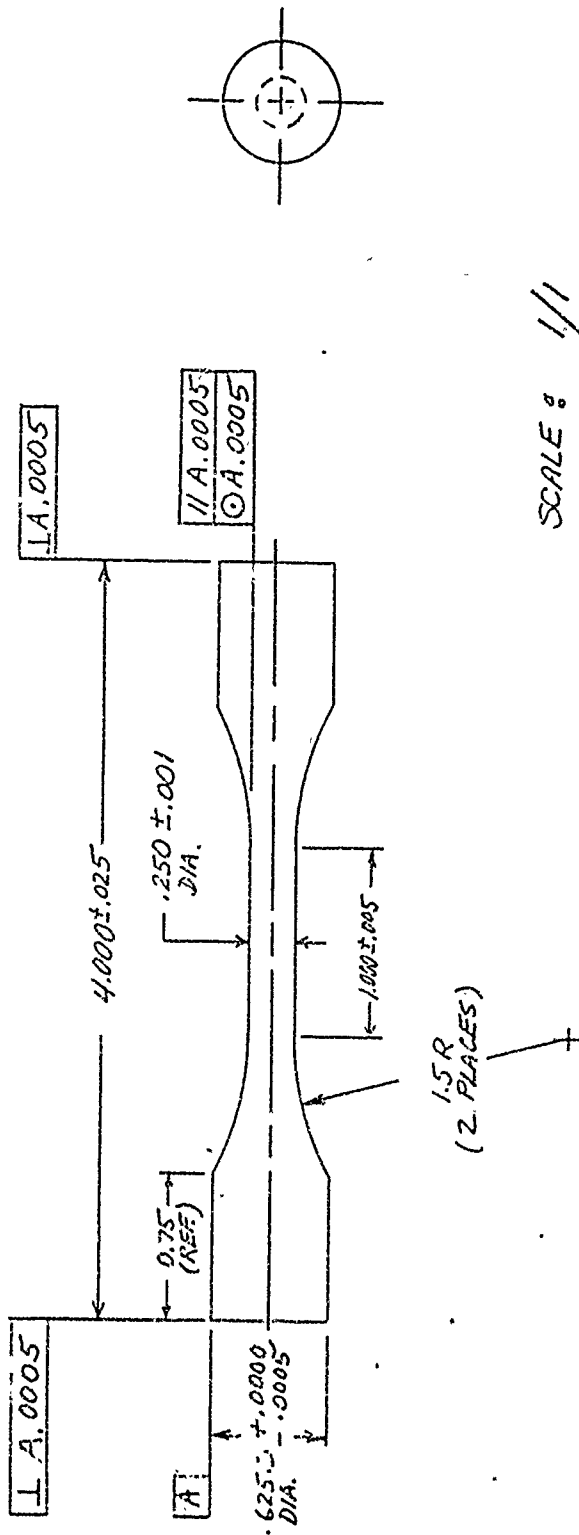
82

Figure 38. Schematic of Triaxial Rod Specimens

83

SCALE : 1/1

NOTES :

1. MATERIAL ~ ATJ-S GRAPHITE

2. ALL SURFACES MACHINED TO $\sqrt{16}$ ROUGHNESS, OR BETTER

3. NO MISMATCH PERMITTED AT TANGENT POINTS WHERE 1.5" RADIUS BLENDS TO .250" DIA.
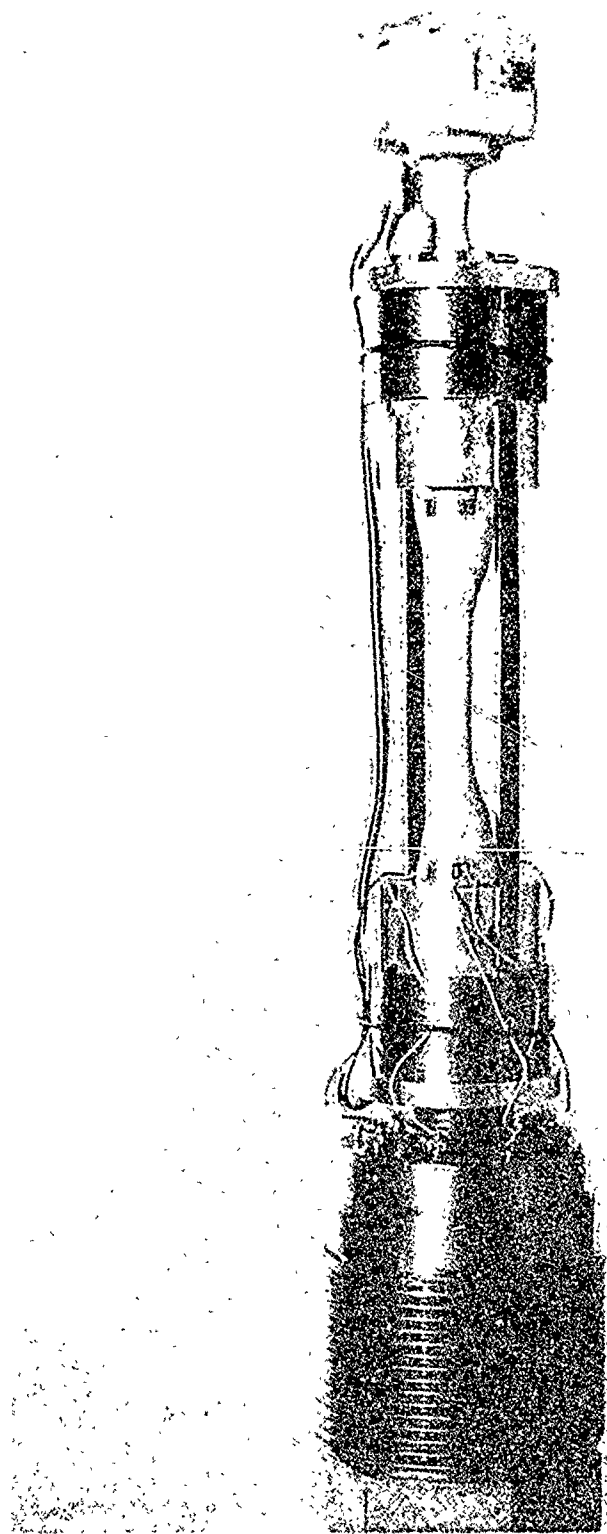
Figure 39. Triaxial Specimen Details

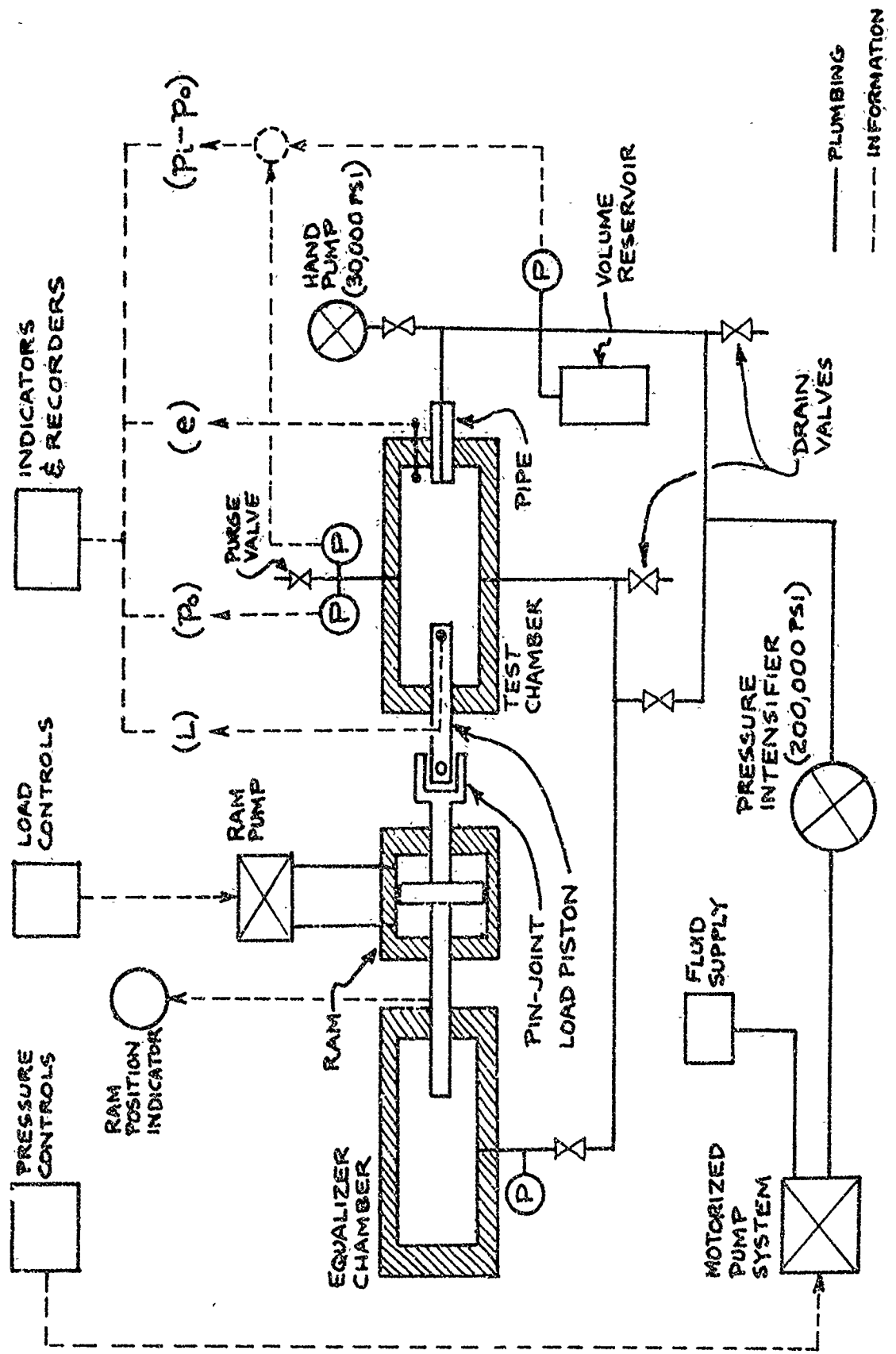Figure 40. Triaxial Specimen Assembly Mounted on PSU Seal Plug
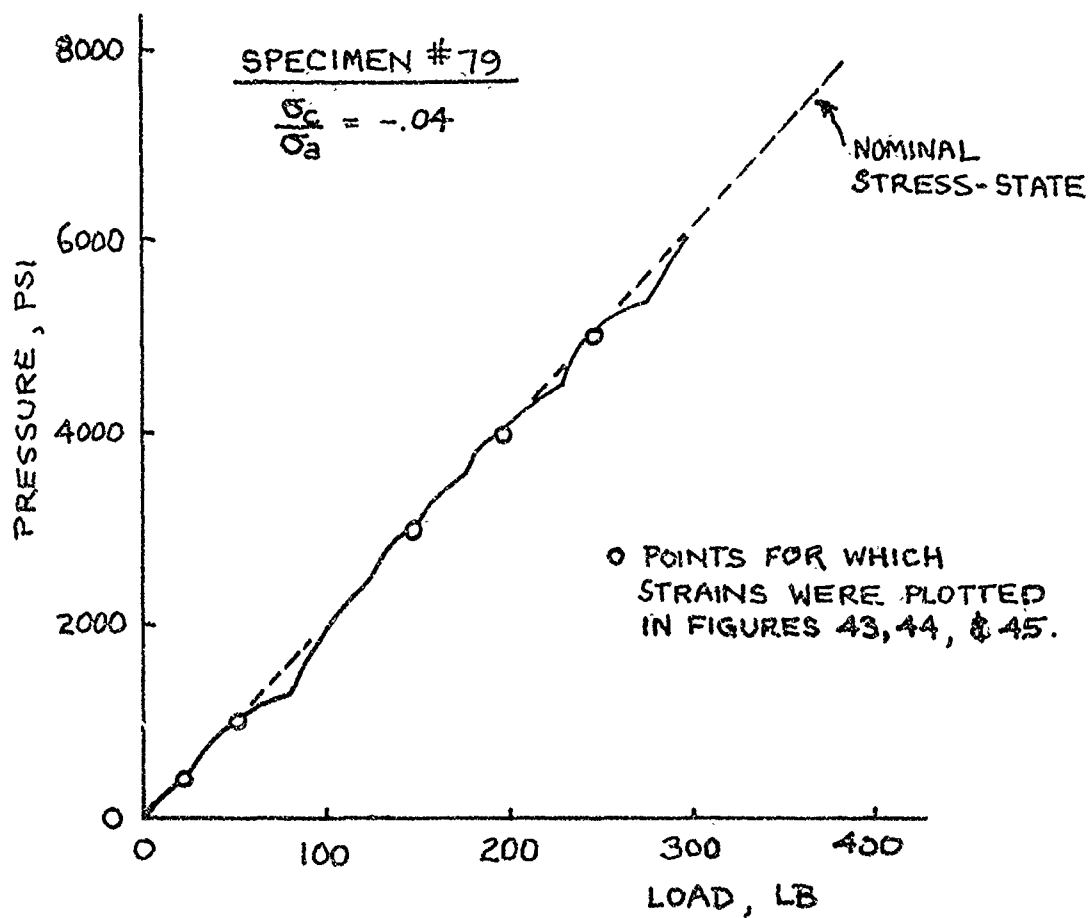
Figure 41. Schematic of Triaxial Facility at PSU

Figure 42. Typical Load-Path for "Proportional" Loading Triaxial Tests

5.4 RESULTS OF PROPORTIONAL-LOADING TESTS

The stress-strain measurements, from the proportionally loaded specimens listed in Table VII, are summarized in Figure 43 and 44. The measured strain trajectories are shown in Figure 45. Predictions of the strain ratios based on linear elastic theory were made using the following elastic constants:

$$E_c = 1.2 \times 10^6 \text{ psi}$$

$$E_a = 1.8 \times 10^6 \text{ psi}$$

$$\nu_{ca} = 0.1$$

$$\nu_{ab} = 0.1$$

These values were estimated from uniaxial test data. The resulting predicted strain ratios are shown in Figure 46 together with the average measured total strain ratios from Figure 45. The good agreement between predicted and measured ratios indicates that the plastic strain trajectories are in approximately the same directions as the total strain trajectories. This result tends to support Weng's assumption of constant strain ratios.

The work given by:

$$W = \int \sigma_c de_c + 2 \int \sigma_a de_a$$

was obtained by numerical integration of the stress-strain graphs. The elastic work W^E was calculated as a function of stress level using the elastic constants listed above:

$$W^E = \sigma_a e_a^E + 1/2 \; \sigma_c e_c^E$$

The plastic work was estimated by:

$$W^P = W - W^E$$

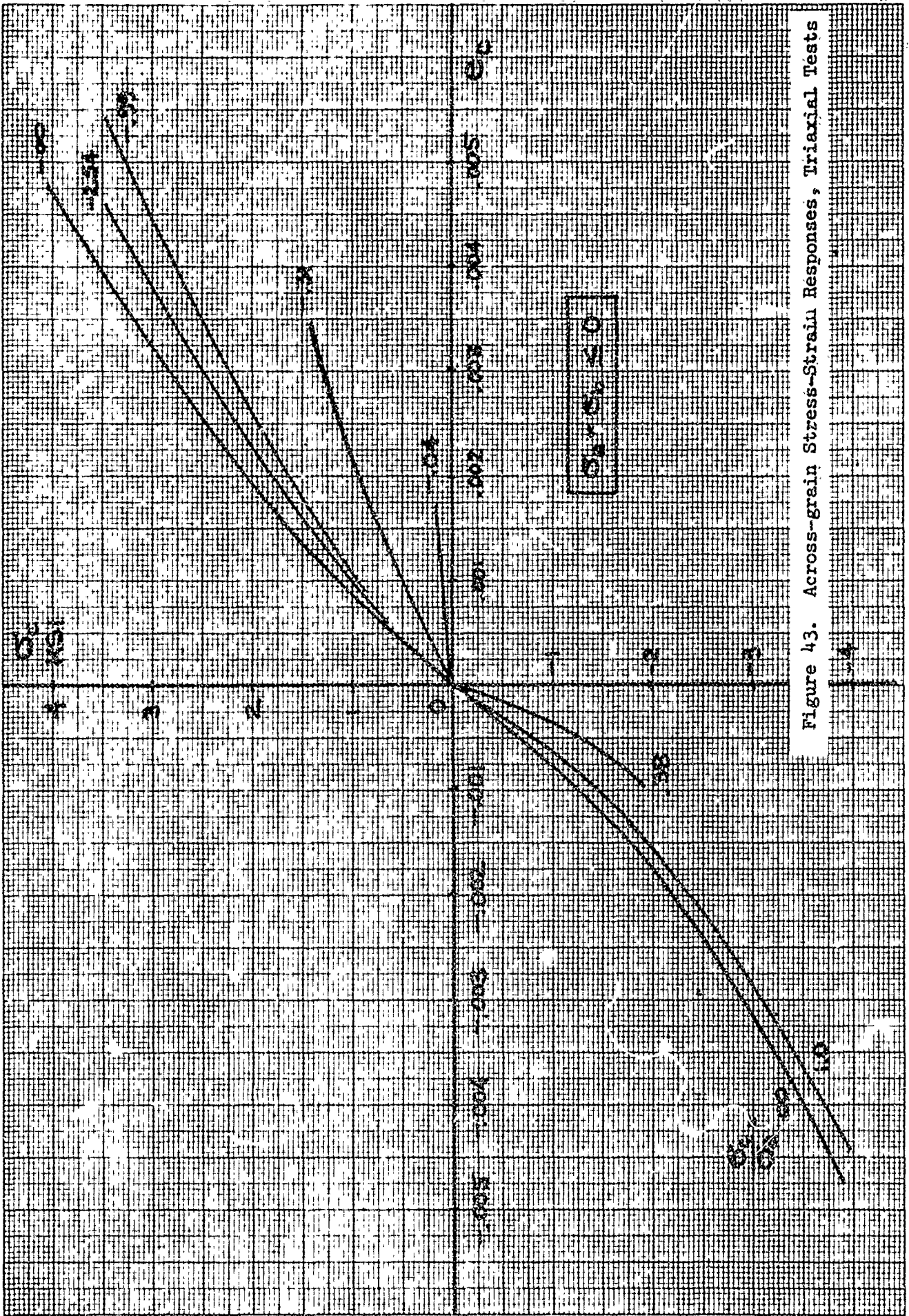The results of these work estimates are shown in Figures 47, 48 and 49.

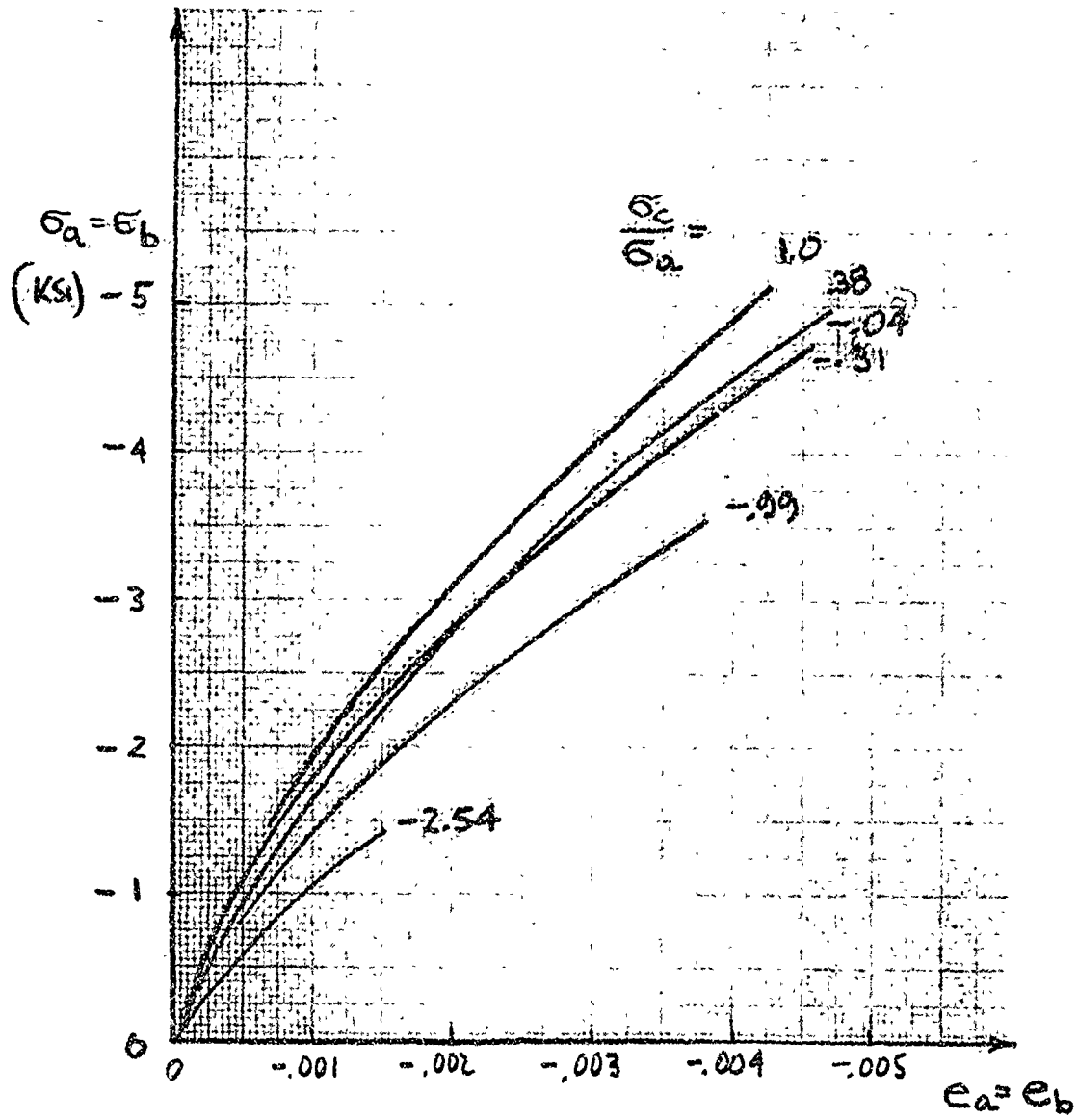Figure 43. Across-grain Stress-Strain Responses, Triaxial Tests

Figure 44. With-grain Stress-Strain Responses, Triaxial Tests
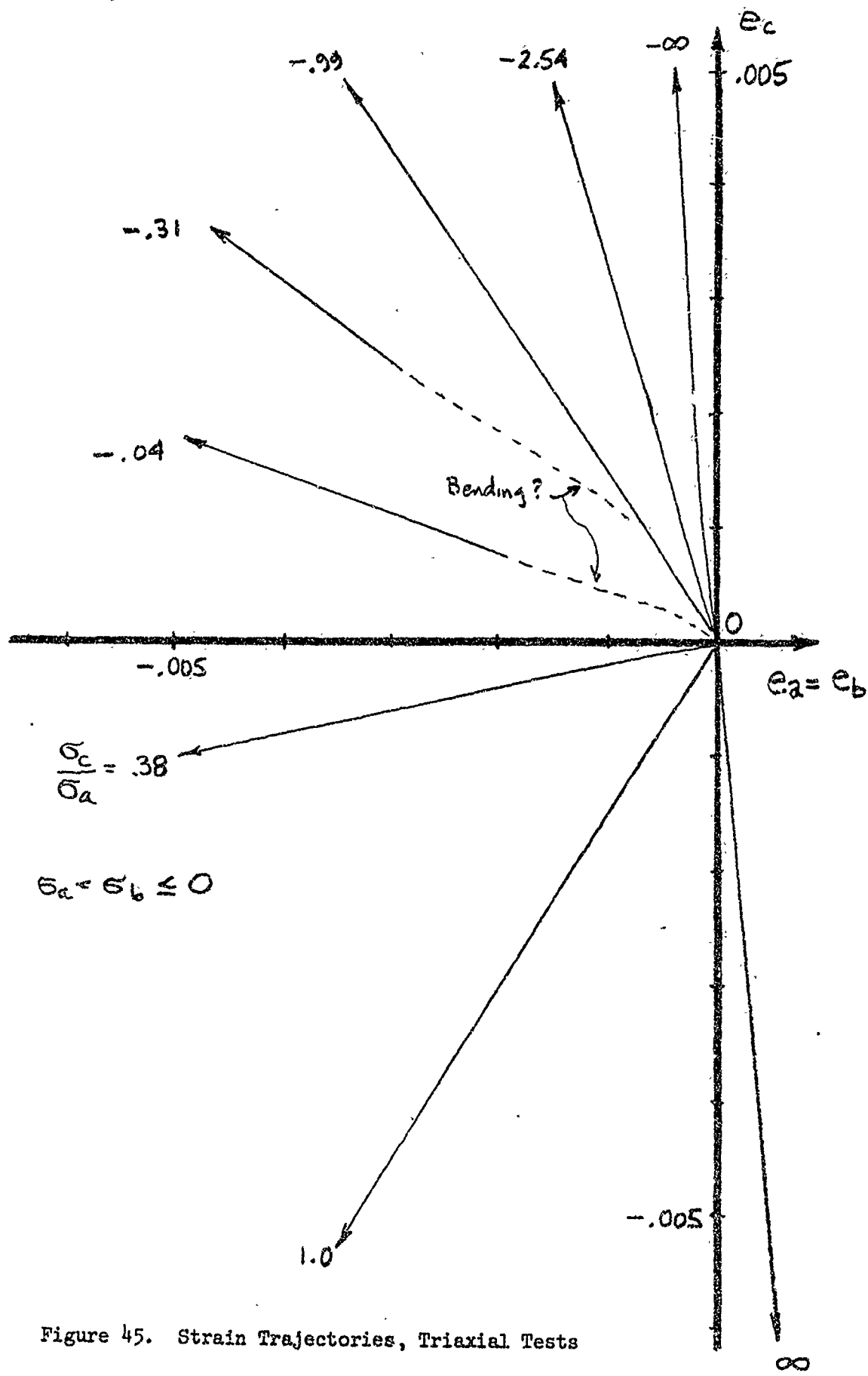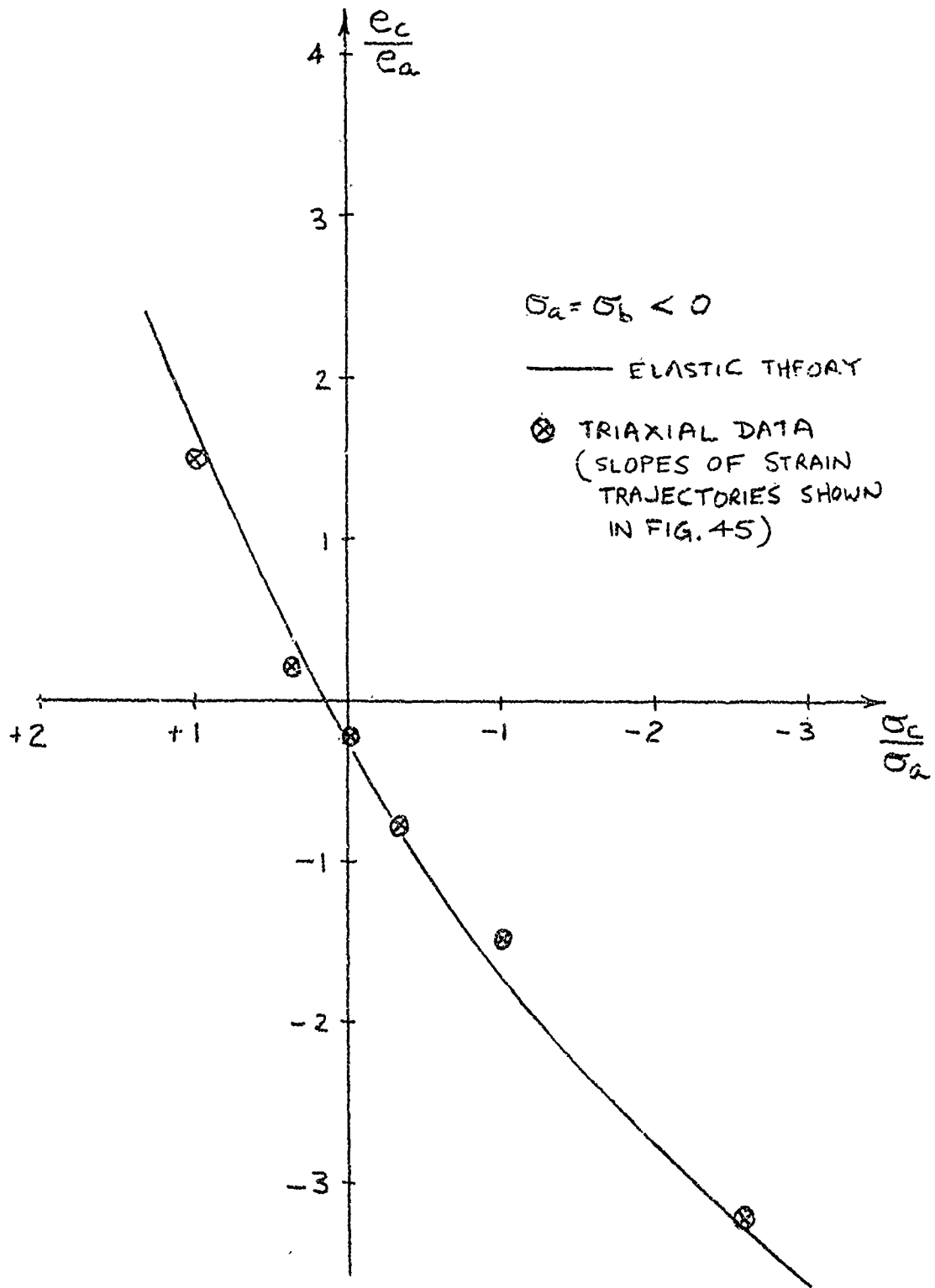
90

Figure 45. Strain Trajectories, Triaxial Tests
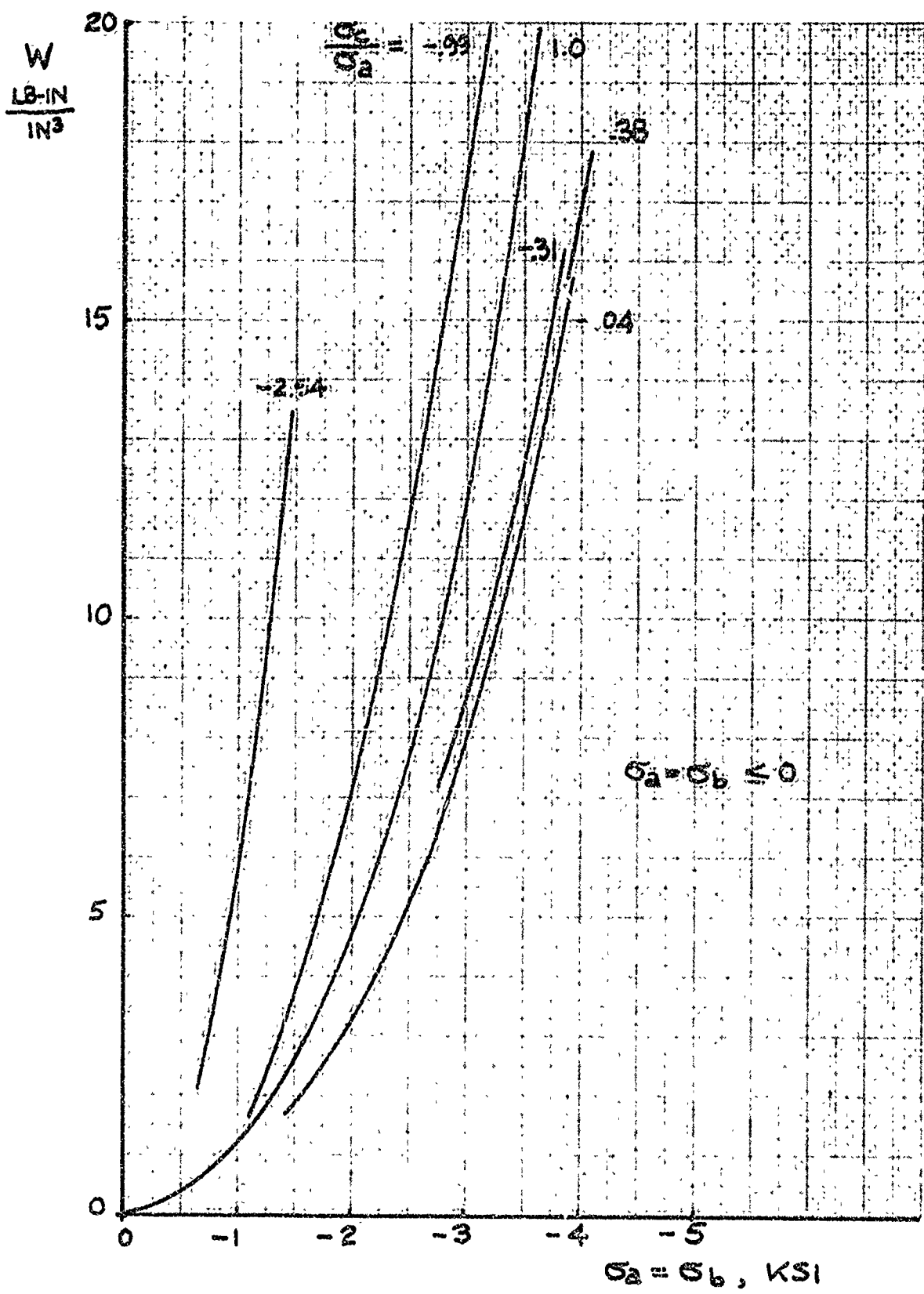
Figure 46. Strain-ratio Prediction (Elastic)

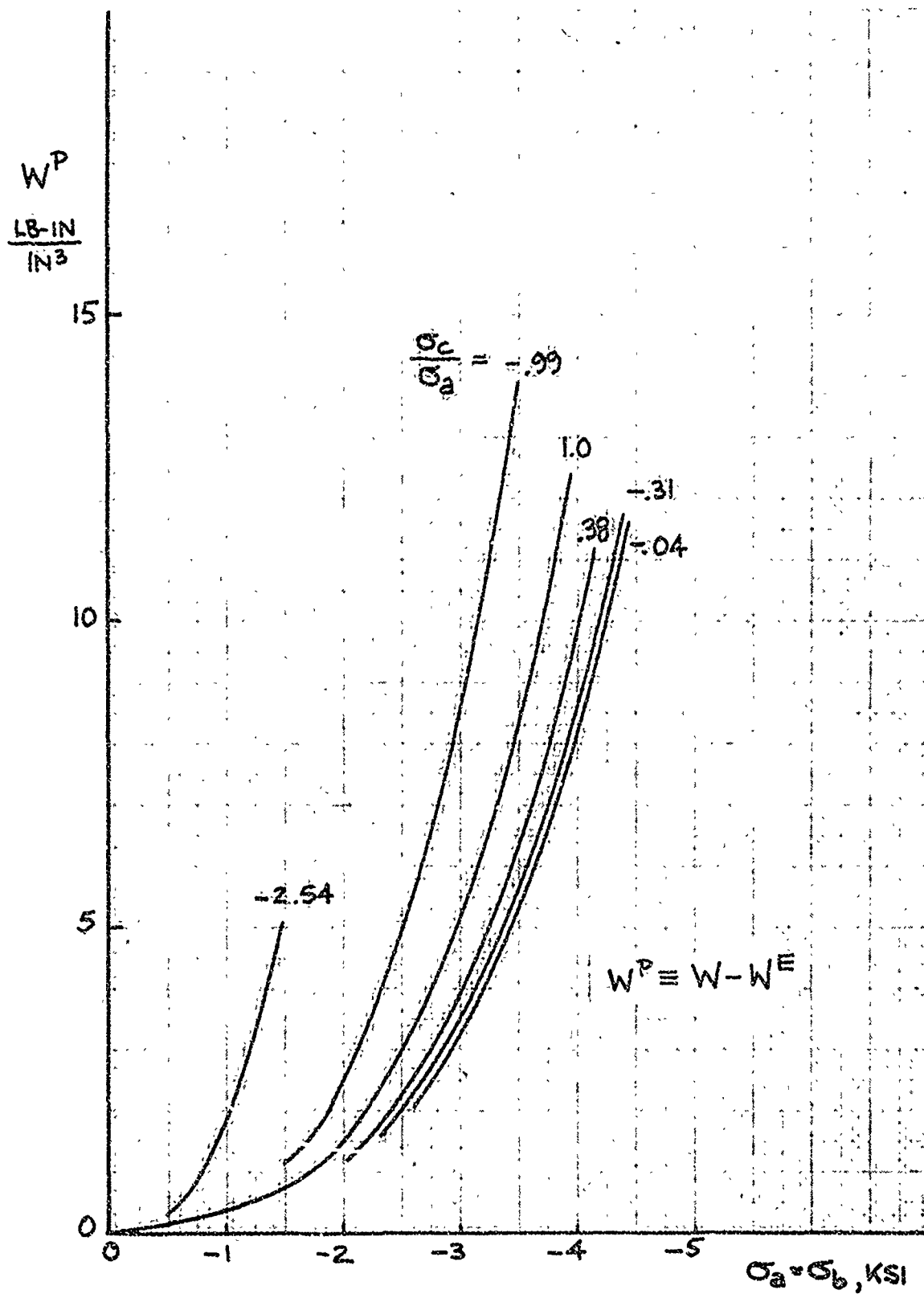Figure 47. Measured Total Work, Triaxial Tests

93

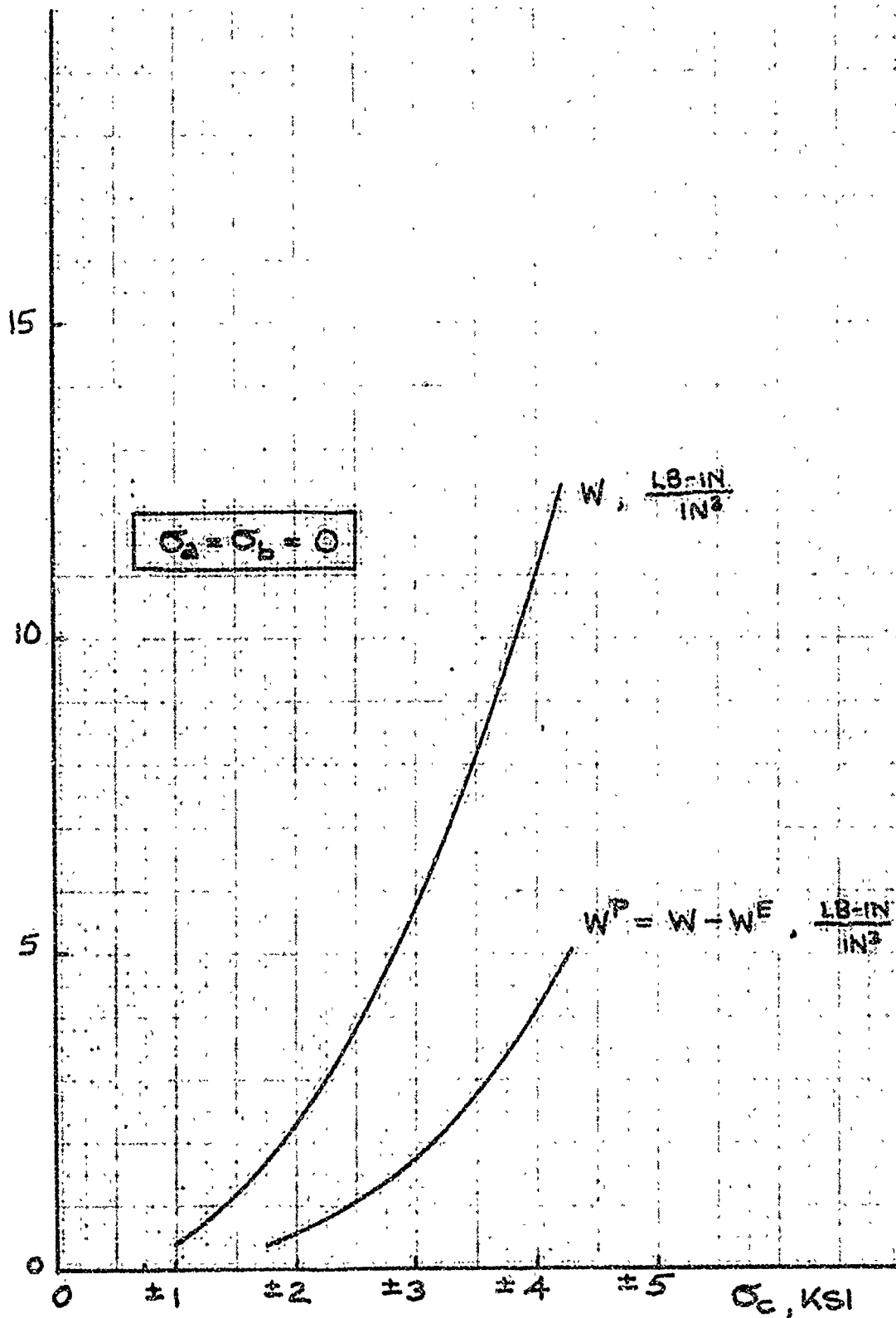Figure 48. Estimated Plastic Work, Triaxial Tests

Figure 49.   Measured Total Work and Estimated Plastic Work in Across-
grain Uniaxial Tension and Uniaxial Compression

The experimentally determined curves of constant total work, W, are shown in stress space in Figure 50. Estimated curves of constant plastic work, W^P, are shown in Figure 51. The shape defined by these curves is not greatly affected by the use of total work rather than plastic work (Figure 52). This result implies that the division of strains into elastic and plastic components may not be necessary in formulating a constitutive law and therefore further tends to support Weng's analysis. Also, the nested nearly concentric appearance of the constant-work curves (Figures 50 and 51) is in agreement with the concept of isotropic strain hardening.

Weng's effective stress function is given by:

$$\bar{\sigma} = \left[a_{aa} \left(\sigma_a^2 + \sigma_b^2 \right) + a_{cc}\sigma_c^2 + 2a_{ab}\sigma_a\sigma_b + 2a_{ac} \left(\sigma_a\sigma_c + \sigma_b\sigma_c \right) \right]^{1/2}$$

where the a_{ij} are proportional to the elastic compliances. Weng's function, at constant $\bar{\sigma}$, defines an ellipsoid in stress space which, when plotted as in Figure 53, agrees remarkably well with the shape of the constant total work locus which was obtained experimentally.

The strain trajectories may be used, as in Figure 54, to define a surface in stress space to which each strain trajectory is normal. The shape of this associated normal surface is in poor agreement with the constant work surface implied by the triaxial data. As changing the assumption of how much of the total strain is plastic strain does not greatly affect the shape of the constant-plastic-work surfaces, it seems that the discrepancy between associated-normal and constant-work surfaces (Figure 54) cannot readily be remedied. It appears therefore that the associated flow rule does not properly describe the behavior of ATJ-S graphite.

These results, although they seem to point clearly to the use of a "non-associated" flow rule and an ellipsoid-like yield surface, must be viewed with some caution because of the step-wise loading employed instead of proportional loading, and because the range of stress-states investigated
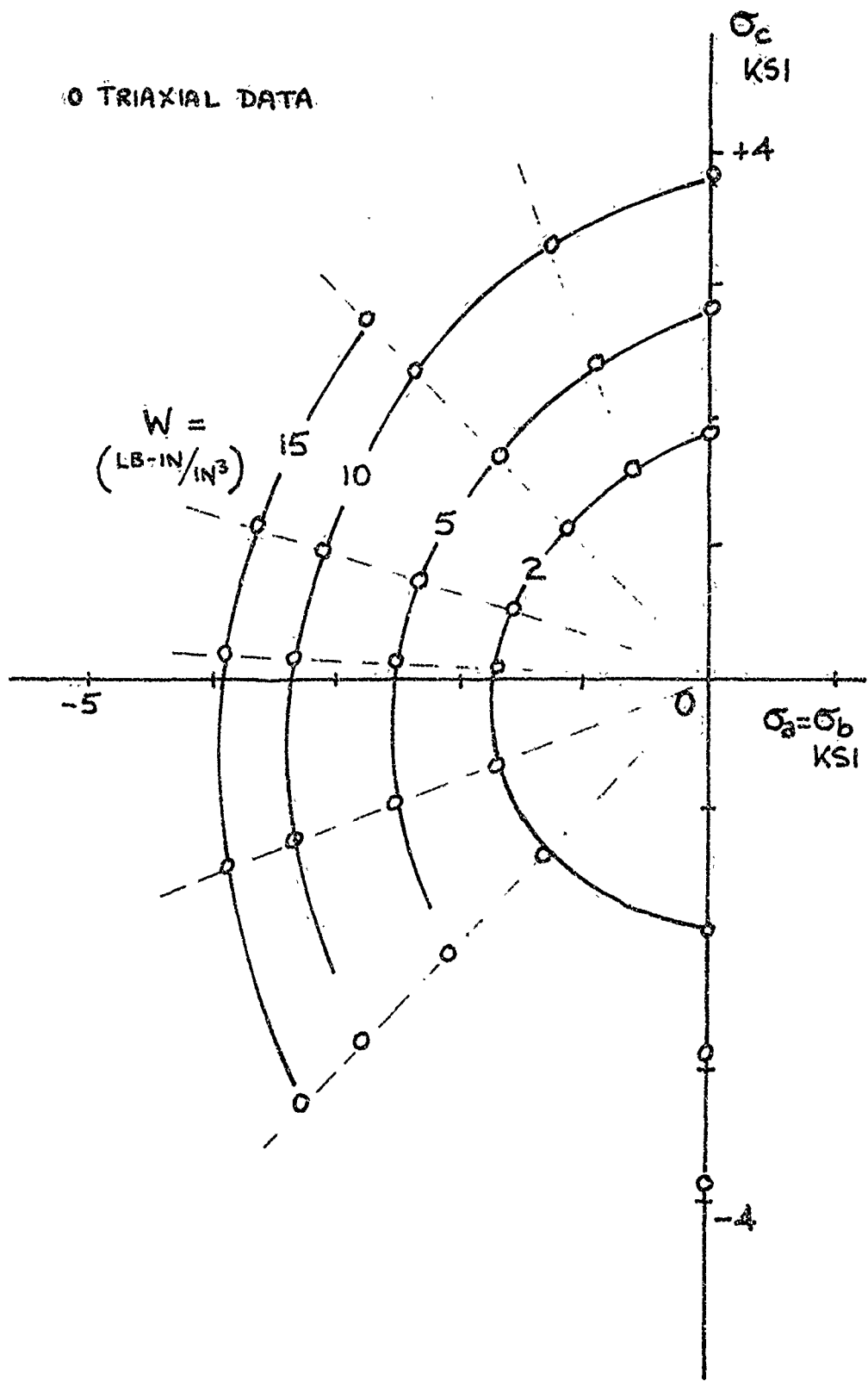
Figure 50.   Loci of Constant Total Work, From Triaxial Tests
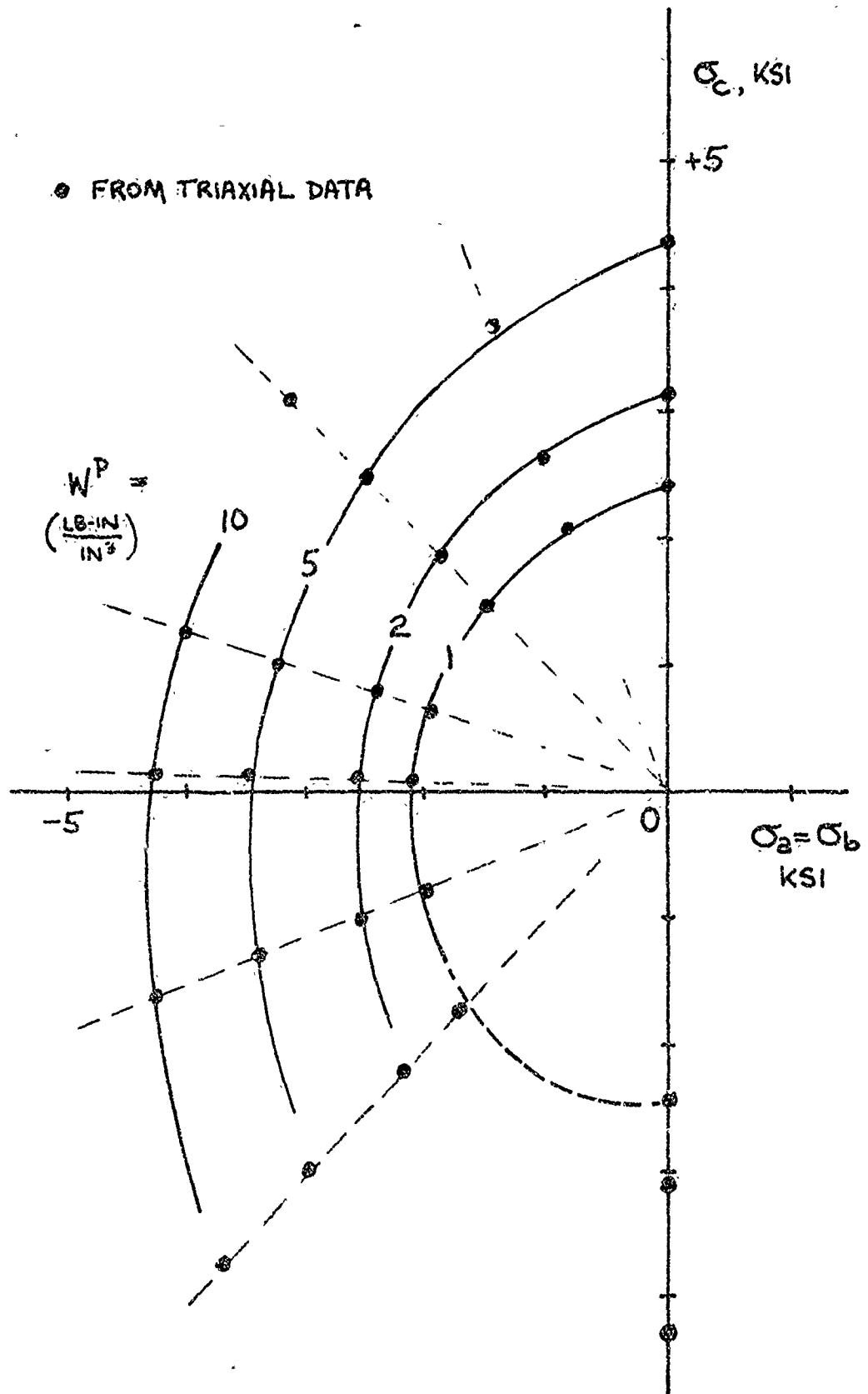
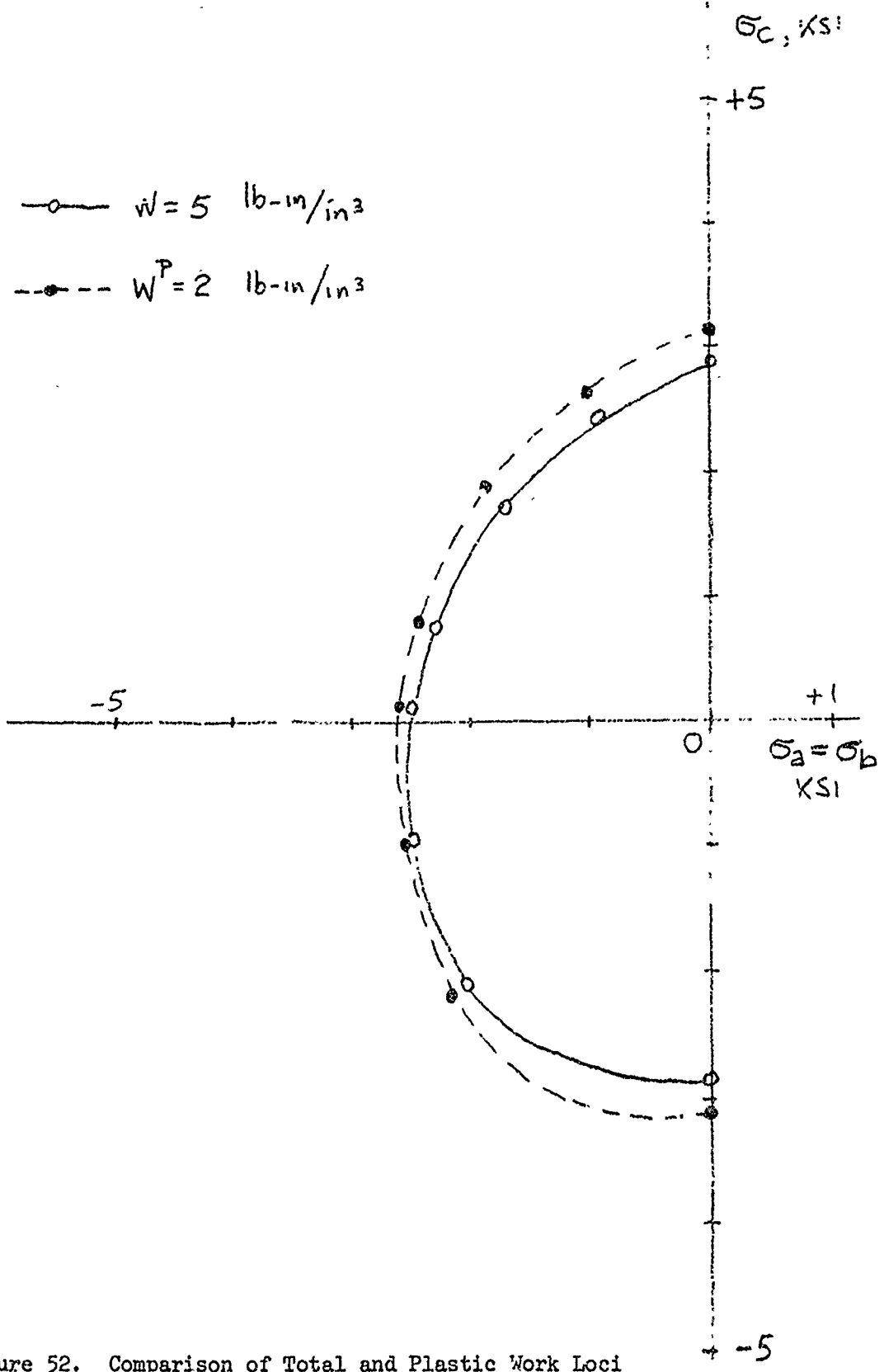Figure 51. Loci of Constant Plastic Work, Triaxial Tests

98

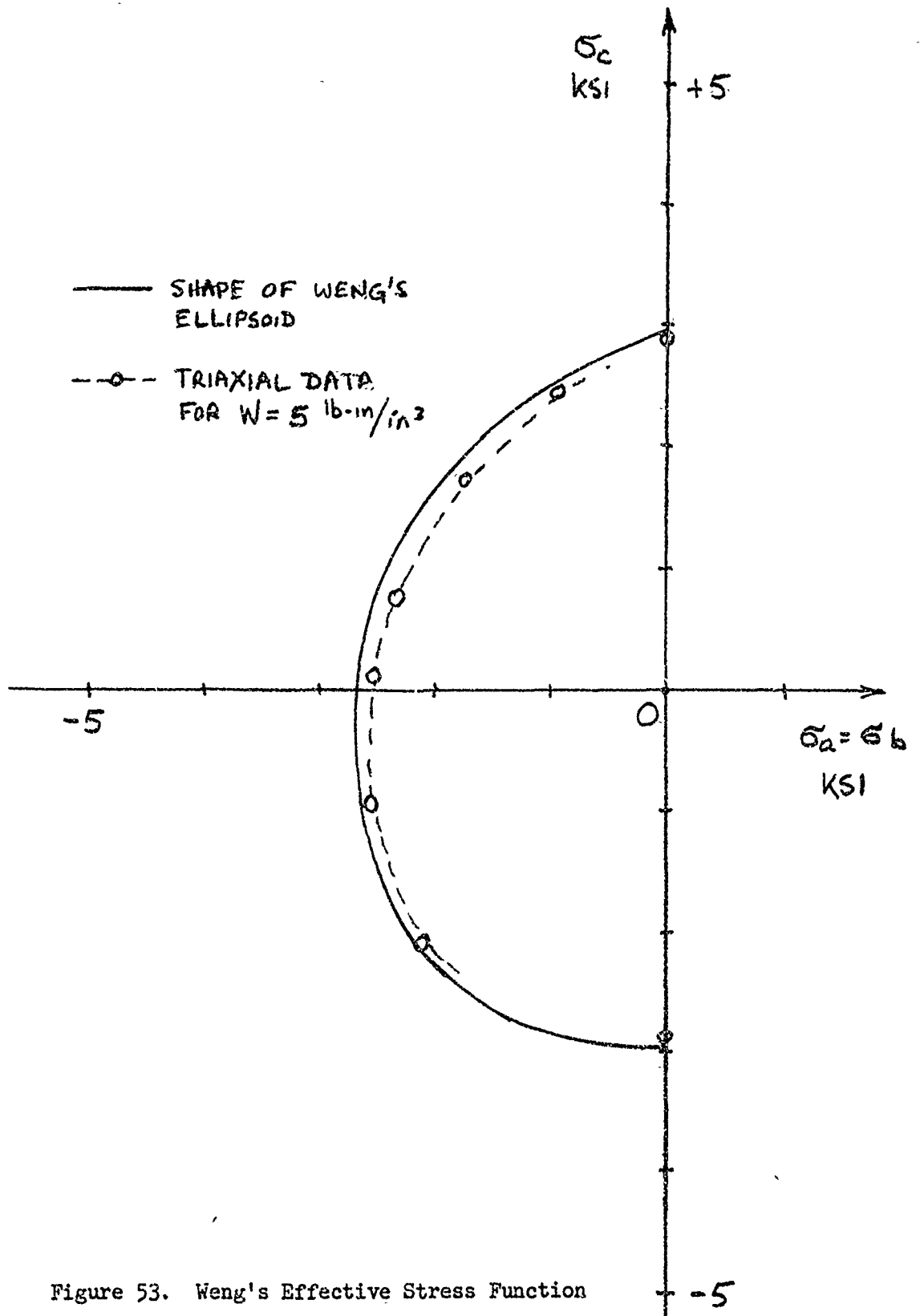Figure 52. Comparison of Total and Plastic Work Loci

99

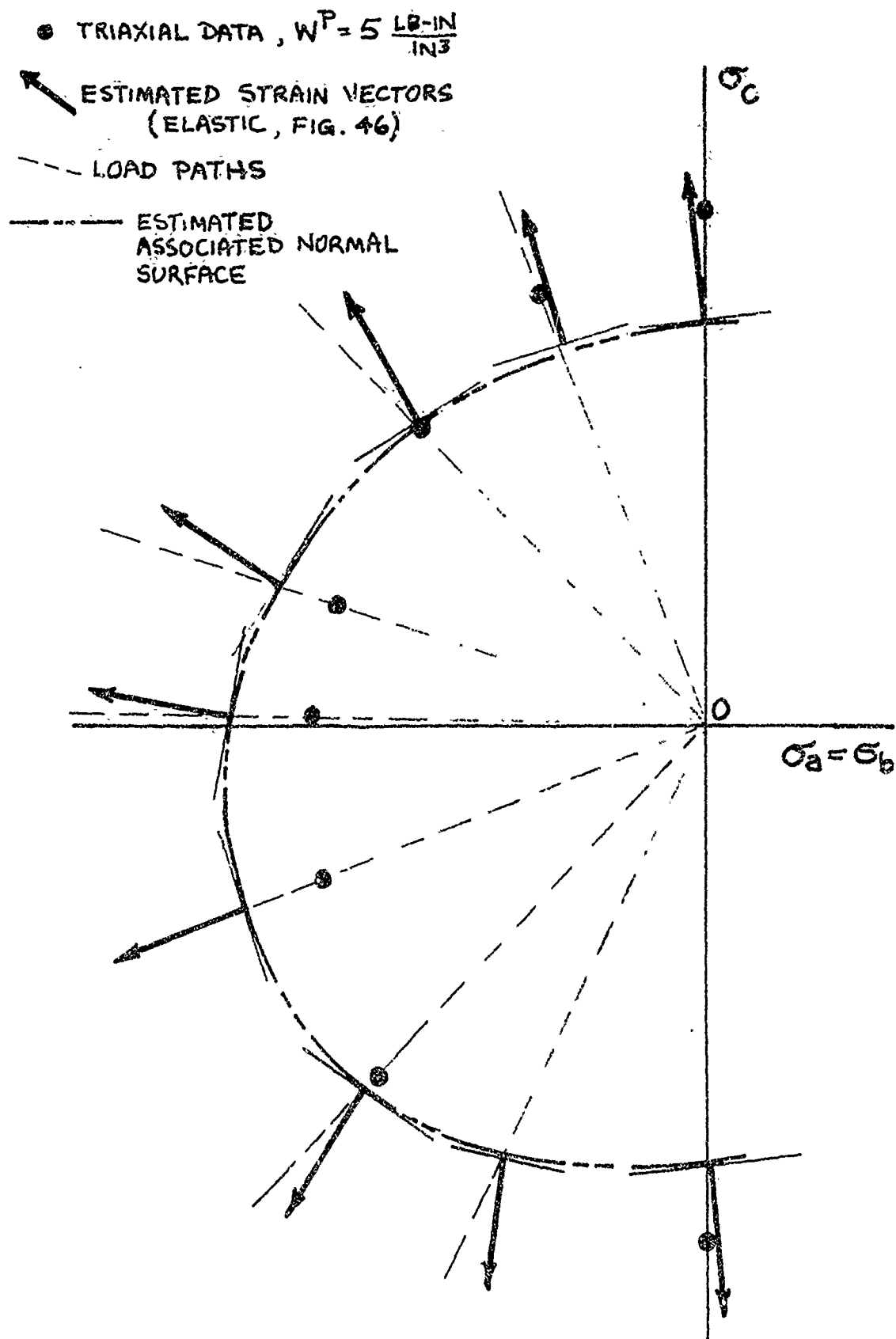Figure 53. Weng's Effective Stress Function

Figure 54. Graphical Definition of Associated Normal Surface

was limited to only one plane in on-axis stress space. The deformation-theory assumptions underlying the concepts employed in analyzing the data do not apply to step-wise loading. It is expected that the results do not depart significantly from true proportional loading because of the relatively small size of the load and pressure steps; however, the possibility of error accumulation must be entertained. The experiments described in Section 5.5 show some of the large effects that load-path can have on strain.

5.5 LOAD-PATH EFFECTS

Some additional triaxial tests were conducted, using the same set-up described in the preceding sections, to explore the effect that loading sequence might have on strains.

The first test was an attempt to show that the step-wise loading used to approximate proportional loading does not appreciably affect strains. Specimen 75 was loaded step-wise, as shown in Figure 55, to simulate hydrostatic pressurization. The rather erratic appearance of the "steps" in the loading of specimen 75 is the result of interactions between load and pressure in the test facility. The stress-strain responses are compared in Figure 56 to those of specimen 71 which was loaded by pressure only. The two curves differ somewhat, implying either some effect of step-wise loading, or some scatter in specimen-to-specimen properties and/or measurements.

The second set of tests is outlined in Figure 57. Two specimens (numbers 80 and 87) were tested, each initially on a different load path, so that the load paths coincided during the last leg of loading. Figure 58 shows the stress-paths followed by the two specimens; also shown are the intersecting stress paths of three specimens tested in "proportional" loading.

Figures 59 and 60 show the strain data for specimens 80 and 87 respectively. Figure 61 compares the stress-strain responses of the two specimens during increasing axial stress at a constant hoop stress of -4000 psi. Not only are the strain values generally different at equal stress-states but so also are the slopes of the axial-stress/axial-strain curves.
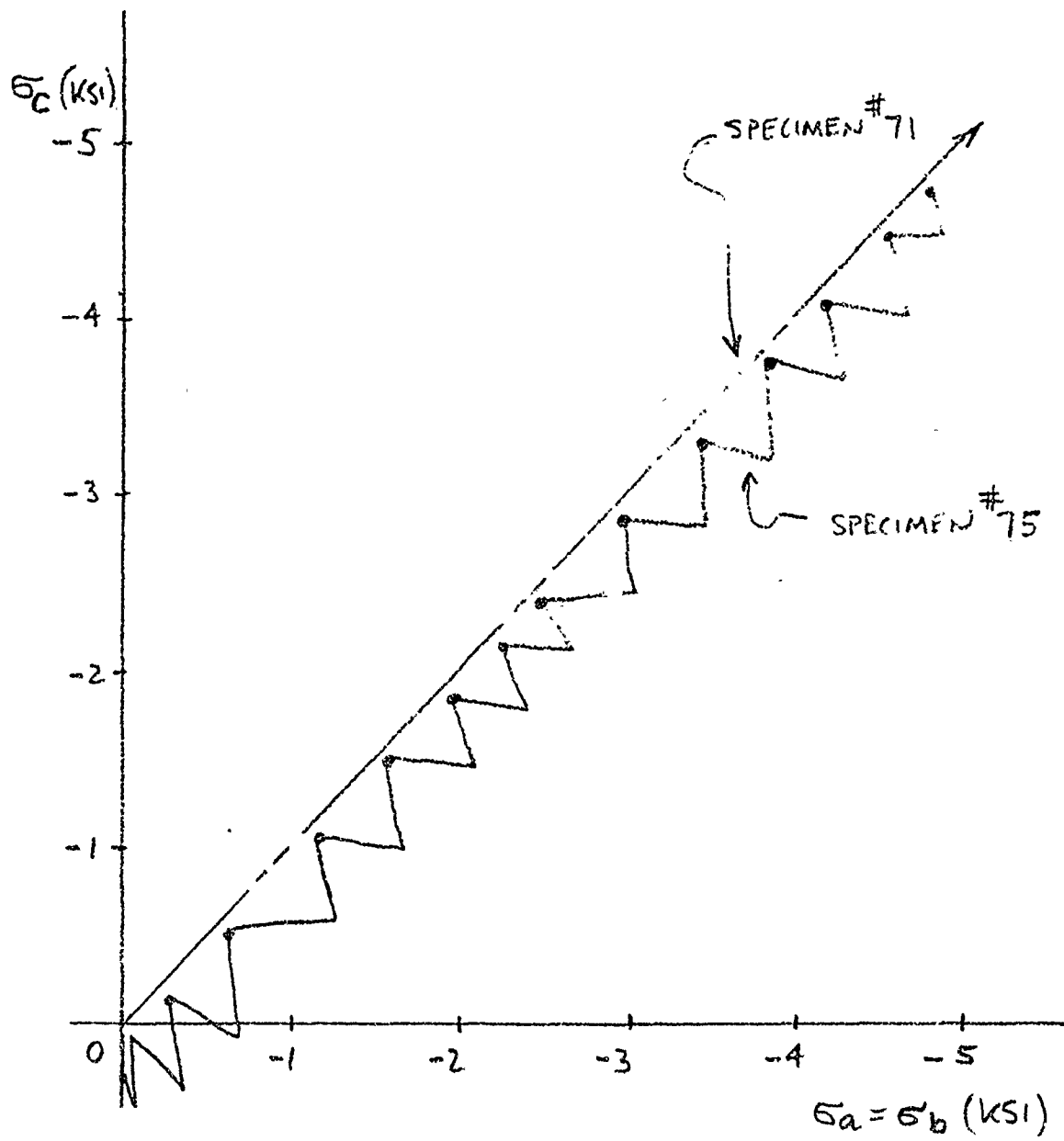
Figure 55. Step-wise Simulation of Hydrostatic Loading

103
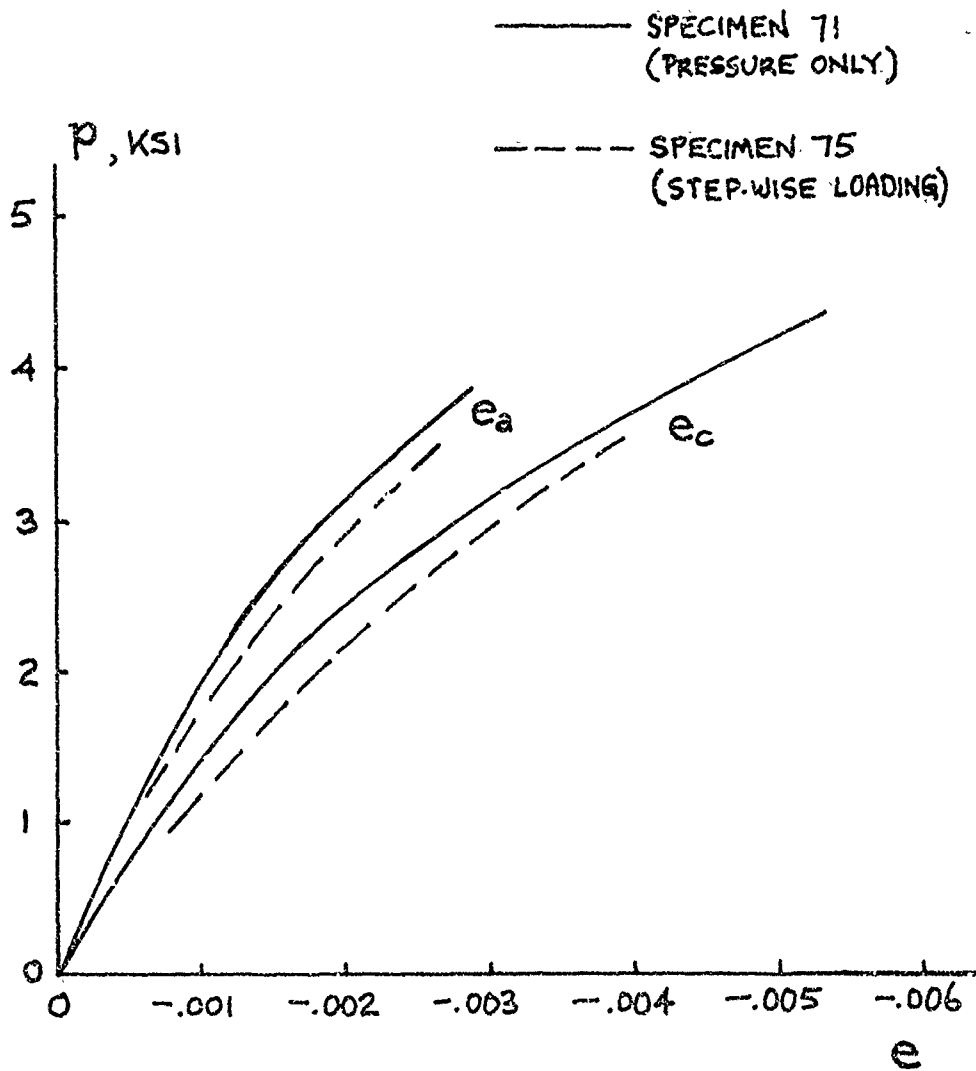
Figure 56. Comparison of Pressure-Strain Data, Stepwise vs. True
Hydrostatic Loading

Figure 57. Load-Paths Followed in Non-proportional Tests

Figure 58.   Stress-Paths Followed in Non-proportional Tests

106

Figure 59. Strain History for Specimen 80

Figure 60. Strain History for Specimen 87

107
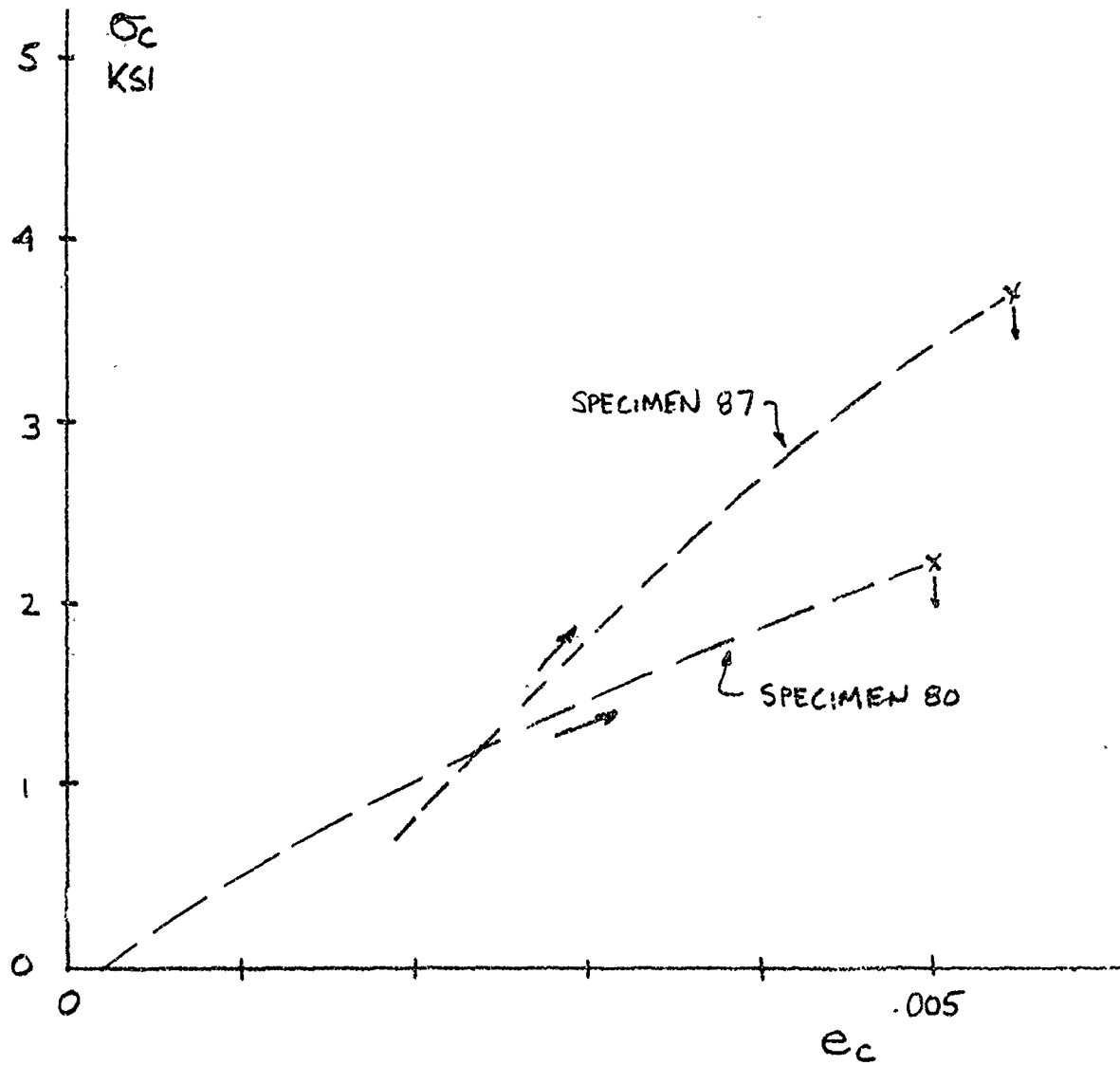
Figure 61. Comparison of Strain Responses to Across-grain Stressing at Constant $\sigma_a = \sigma_b = -4000$ psi After Two Different Stress Histories

108

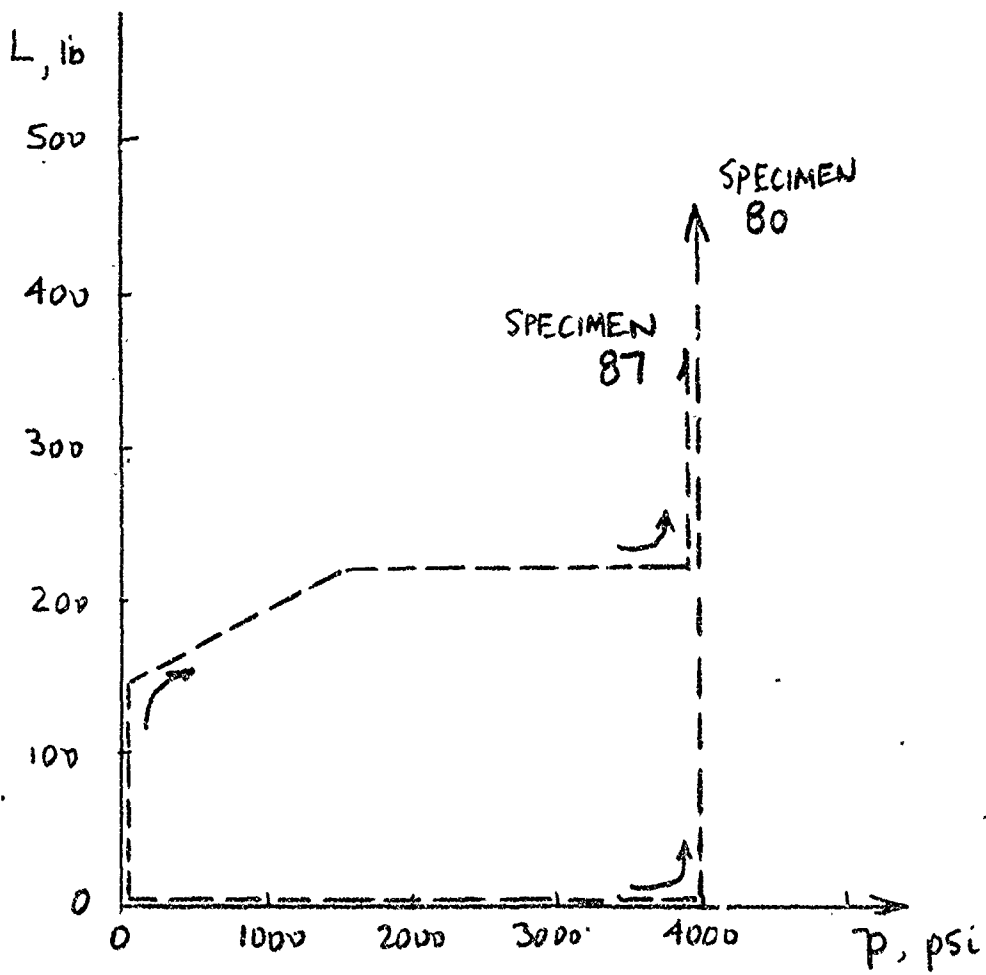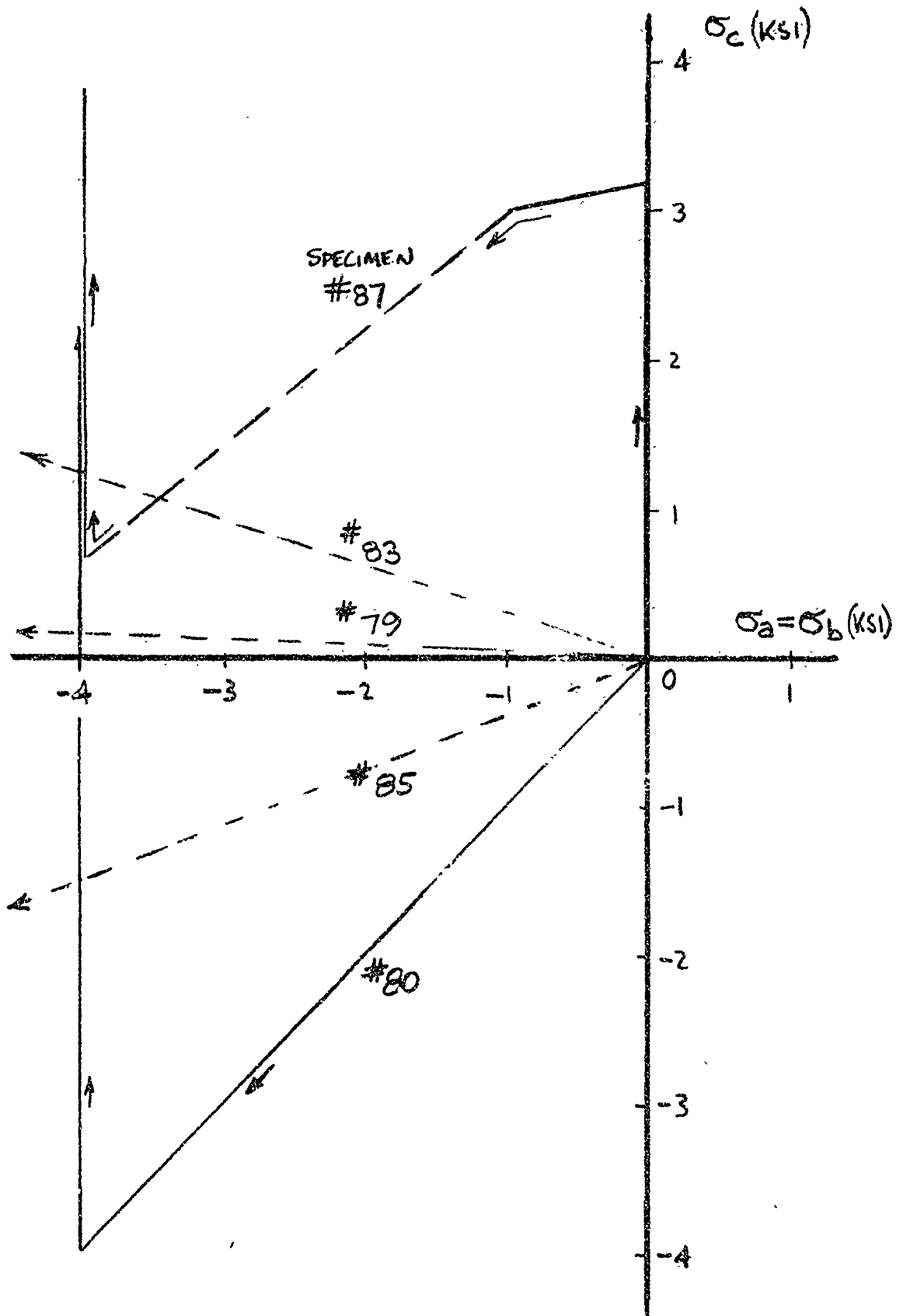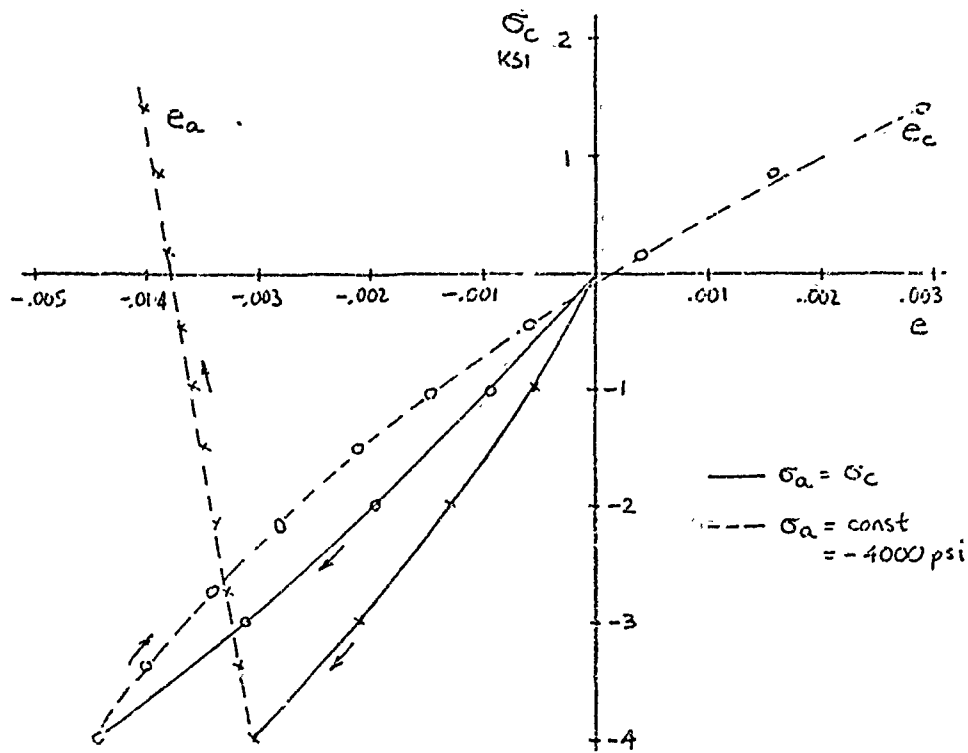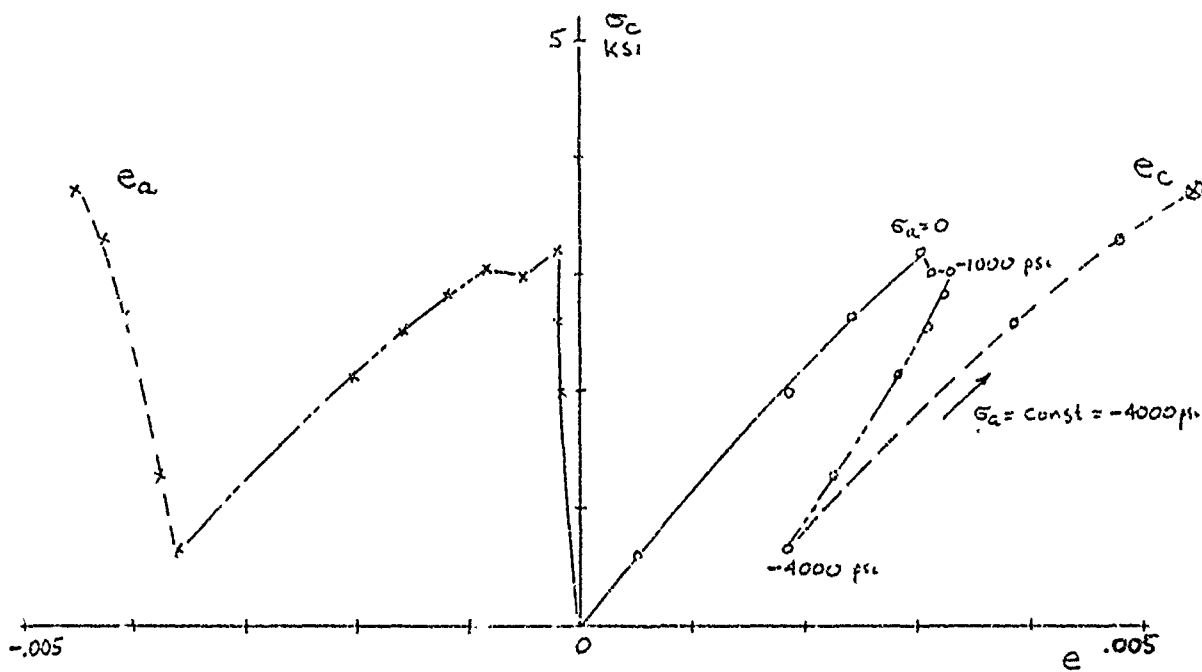Table VIII compares the strains at equal stress-states, arrived at via different load paths, for the specimens indicated in Figure 58.

The results prevent one from taking too much comfort in having defined, tentatively, in the preceding section, a yield function form and a flow rule for proportional loading of ATJ-S.

The load paths of specimens 80 and 87 involved reversals of effective stress in that the stress path re-entered the yield surface. Load reversals generally do result in load-path effects on current strain in most materials. It might be of interest to measure the effect of non-reentrant load paths (Figure 62) on strain. The interested reader is referred to the work of Greenstreet and Phillips (Reference 28) for an approach to modeling load-path changes in graphite.

It appears that the triaxial test can be a versatile tool for experimentally studying both deformational and incremental constitutive laws. Further test work in an improved facility, capable of precise (automated) proportional load-path control, would undoubtedly provide useful results.

TABLE VIII

LOAD-PATH EFFECTS ON STRAIN AT $\sigma_a = \sigma_b = -4000$ PSI

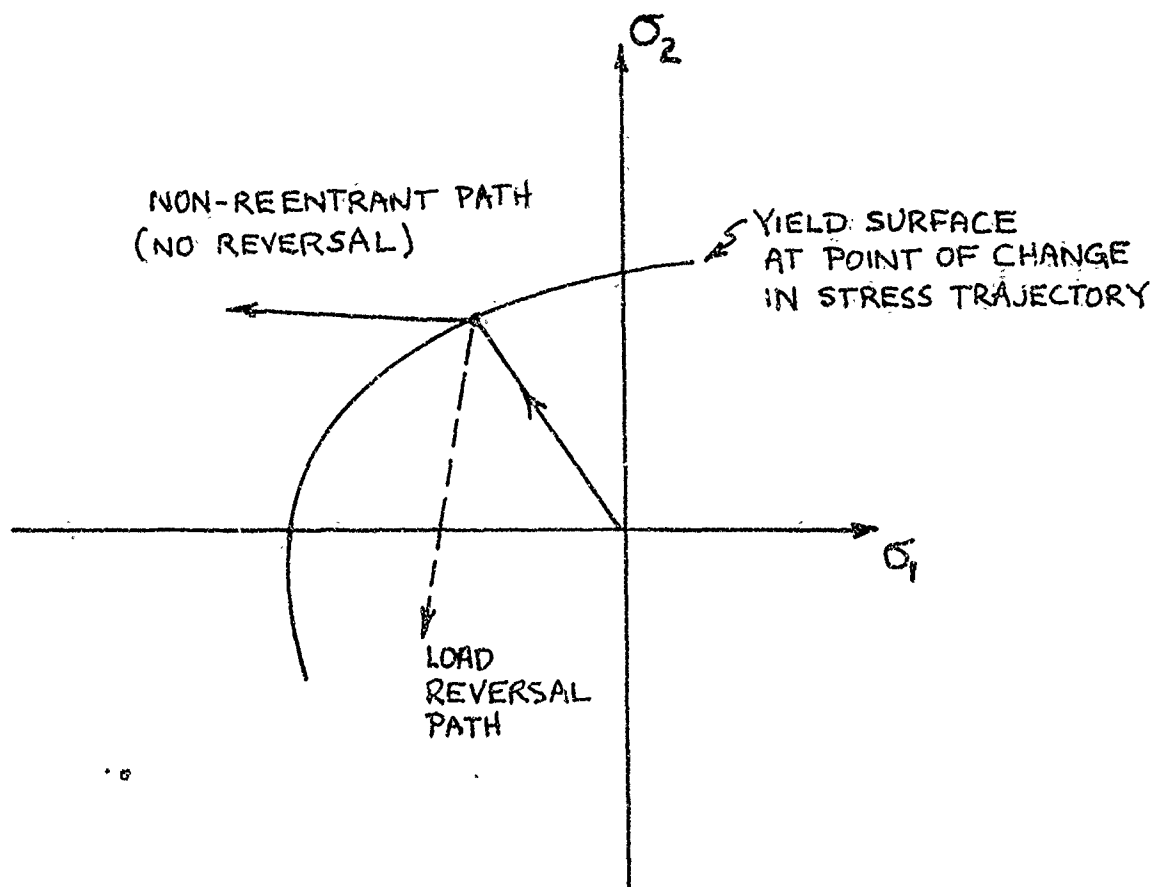| SPECIMEN	LOAD PATH	σ_c PSI	e_c	e_c	DATA FOR SPECIMEN 80* (LOAD-REVERSAL) e_a	e_c
85	Proportional	-1500	-0.0006	-0.0032	-0.0021	-0.0035
79	Proportional	130	0.0012	-0.0032	0.0004	-0.0038
87	Complex	640	0.0018	-0.0036	0.0013	-0.0039
		1220	0.0024	-0.0038	0.0026	-0.0040
83	Proportional	1220	0.0027	-0.0034	0.0026	-0.0040

*At tabulated value of σ_c

110

Figure 62.   Nomenclature for Load Reversal

111

Section 6
BIAXIAL-SOFTENING EXPERIMENTS

"Biaxial softening" is the name given (Reference 1) to the phenomenon that principal strains in ATJ-S at a given principal-stress level tend to be larger in biaxial tension than in uniaxial tension. This trend runs counter to the expectation that Poisson's ratio would result in smaller strains in biaxial tension. Figure 63 schematically illustrates the biaxial softening effect. The data on biaxial softening obtained so far (Reference 1, 2 and 3) was taken under proportional loading conditions.

To further explore biaxial softening, three biaxial specimens of standard design (Figure 4) were excised from billet 12S1-3 and tested along three different load paths as illustrated in Figure 64. The biaxial tensile stress state ($\sigma_{Am}/\sigma_{Hm} = 0.48$) of point "x", where all three load paths coverage, is obtained by simple pressurization of the biaxial specimen assembly. The three specimens were very close in dimensions; the wall thickness ranged from 0.0499 for specimen 87 to 0.0503 for specimen 85. The leg bx, for specimen 87 in Figure 64, was obtained by simultaneously increasing pressure and decreasing the load; control over this process was automatic (using a servo loop) and the smooth line shown in Figure 64 represents the actual stress path. The same servo control was used to maintain the ratio of load to pressure along leg oa for specimen 85.

The specimens were each equipped with one axial strain-gage and one hoop strain-gage at the outer surface of the gage section. Tracings of the strain records taken on X-Y recorders during tests are shown in Figure 65.

The strain results in Figure 65 reveal the following:

A.   The hoop strain at "x" for specimen 77 is greater than at "a" for specimen 85, thus corroborating the softening effect illustrated in Figure 63.

Preceding page blank
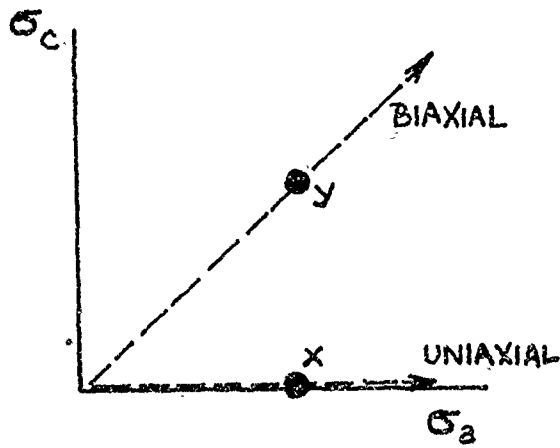
STRESS PATHS   STRAIN TRAJECTORIES
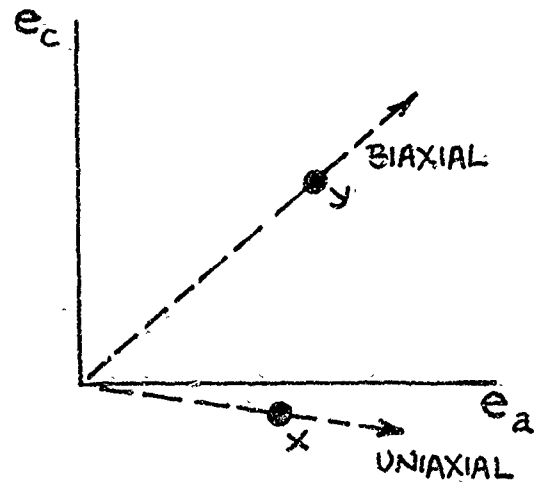
STRESS-STRAIN RESPONSES
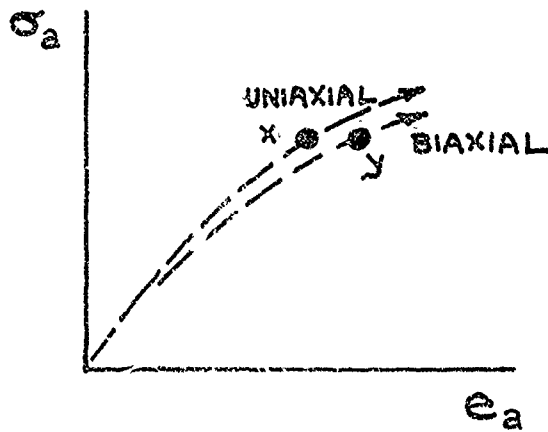
SOFTENING IN BIAXIAL TENSION :   AT x AND y

$$\sigma_{ay} = \sigma_{ax}$$

$$e_{ay} > e_{ax}$$

Figure 63.   Schematics Illustrating Biaxial Softening

114

Figure 64. Stress Trajectories for Biaxial Softening Tests

APPLIED LOAD AND PRESSURE		
Point	L, lbs	p, psi
a	-292	372
b (upper)	+295	0
x_{87}	+5	370
x_{77}	0	372
x_{85}	0	372

115
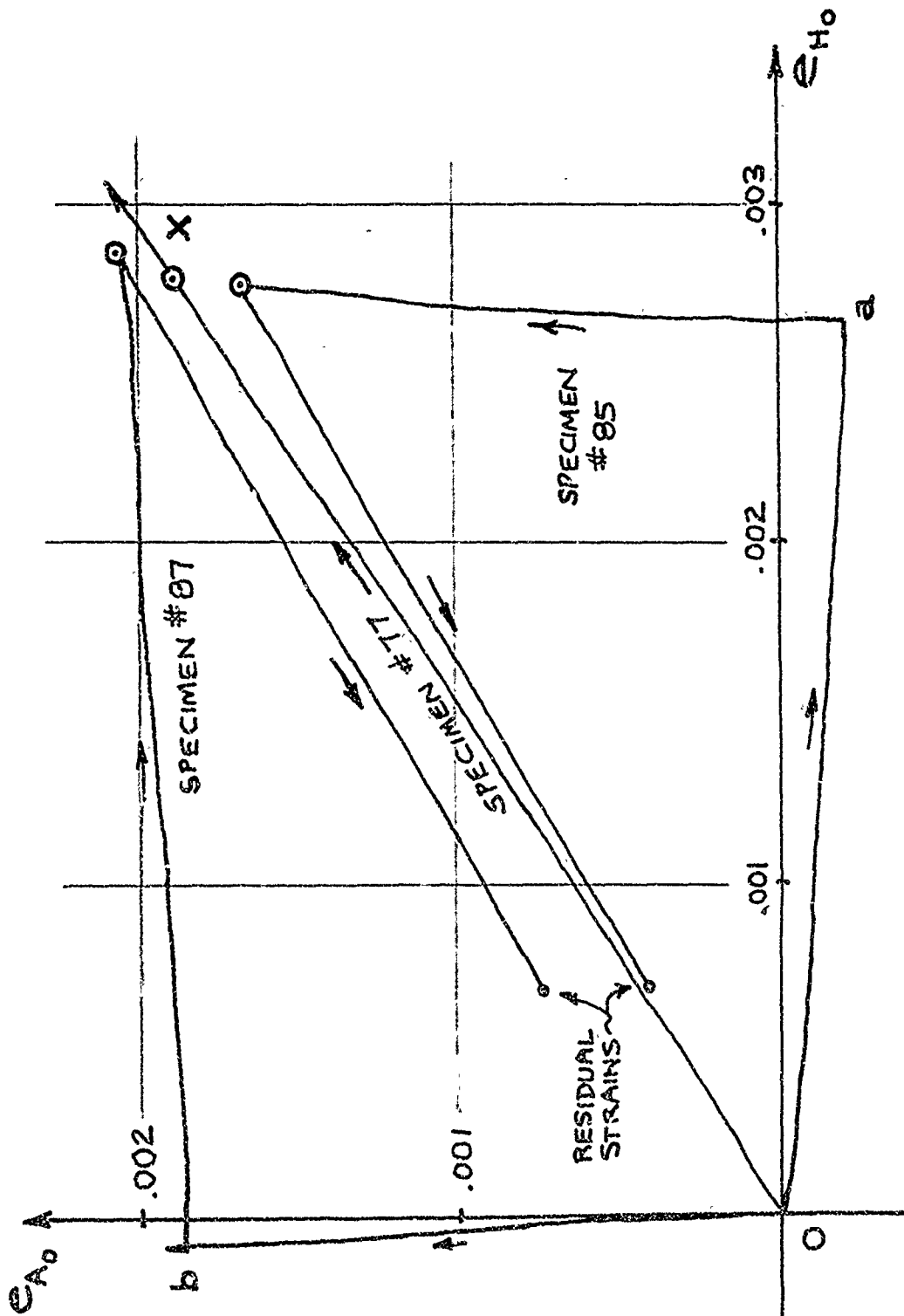
Figure 65. Tracings of Strain Records of Biaxial Softening Tests

116

B. The axial strain at "x" for specimen 77 is the same as that at
    "b" for specimen 87. This suggests that biaxial softening occurs
    also for across-grain (axial) strains because one would expect
    the axial strain at "x" for specimen 77 to be smaller based on
    normal Poisson's effects. The lesser magnitude of softening in
    the axial direction may be due simply to the lower axial stress
    level.

C. In legs bx and ax, specimens 87 and 85 respectively exhibit
    "negative incremental Poisson's ratios" which are another
    indicator of the softening phenomenon.

D. The load path selected affects the values of strain at
   stress-state "x".

Does biaxial softening also occur in biaxial compression? Some of the data
from the triaxial tests described in Section 5 is relevent to this question.
Figure 66 shows with-grain stress-strain responses measured under uniaxial,
biaxial, and triaxial compression on specimens from Billet 12S1-3. The
measured compressive strain response of the specimen exposed to biaxial com-
pression is softer than that of the uniaxial specimen. The measured triaxial
response, however, is stiffer. Thus the evidence seems inconclusive
especially when it is recalled that the compressive biaxial test was performed
under pseudo-proportional loading (Figure 42) and that some scatter in the
strain data may result from that cause or other causes (as suggested by
Figures 56 and 20). Thus there appears to be a need to conduct further tests
under better load-path control.

It would be interesting to explore the compressive behavior further because,
insofar as tensile deformations depend on the formation of new pores or
cracks within the graphite, the mechanisms of tensile and compressive
behavior may be different. Further testing of biaxial tube specimens that
have undergone various load paths in biaxial tension (such as those in
Figure 64) to discover how their post-test behavior differs from virgin
specimens, and how between-test annealing might influence such behavior,
would also be of interest because it might shed some light on the mechanisms
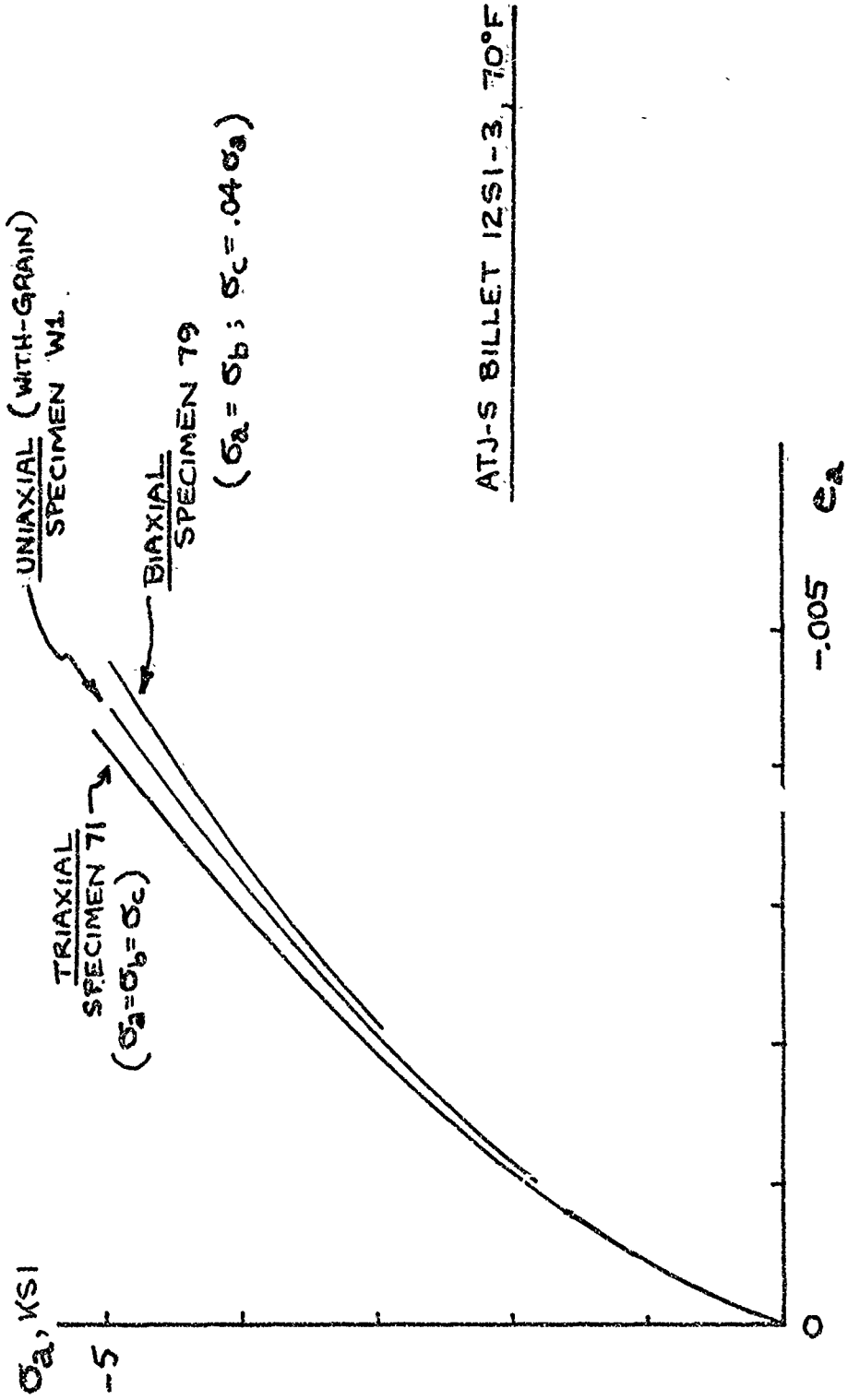of deformation in biaxial tension.

117

Figure 66. Stress-Strain Responses Under Uniaxial and Multiaxial Compression

Section 7
SUMMARY

With respect to the objectives stated in the Introduction (Section 1), the following results have been obtained in this program:

A.   Additional biaxial fracture results have been obtained at 2000°F (Section 4). The data shows a greater degradation in strength as a result of biaxiality in tension than did the 70°F biaxial data summarized in Reference 3 and in Section 3.5. The significance of the 2000°F strength data is clouded by the finding of an anomalous inclusion at the fracture origin of one of the lower strength specimens. Attempts to reconstruct other low strength specimens to view the fracture origins were not successful. It is possible that the 2000°F data may simply represent a "bad" billet. However, until additional information is obtained, caution must be exercised in using 70°F biaxial strength trends in designing for elevated temperature use.

B.   An analytical evaluation of the biaxial test technique has been carried out (Section 3). The prime motivation was to explain the low uniaxial strengths reported for biaxial specimens. It was found that part of the discrepancy between uniaxial and biaxial specimen strengths may be attributed to the larger stress gradients in the biaxial specimen and the fact that mean rather than maximum stresses were reported in References 1, 2 and 3. However, some of the discrepancy is attributed to less easily quantifiable influences such as differences in volume, surface area, minimum gage dimension, potential for damage during fabrication or handling, test complexity, etc. These factors/effects are statistical in nature and might be expected to change the histogram of strengths as well as the mean strength. Insofar as biaxial strength trends

119

depend on the statistics of, say, flaw orientations and sizes, the biaxial strength envelope might also be affected. An analysis based on fracture mechanics considerations suggests that free-surface stress-intensity magnification factors may play a significant role in the statistics of graphite fracture. If so, then tests on specimens with appreciable surface-area-to-volume ratios may give pessimistic strength criteria if the expected region of fracture in a structural component is completely internal to the component, as is the case for an externally-heated thermally-stressed solid body.

C. Additional deformation data under biaxial and triaxial stress-states has been obtained at room temperature:

1. A limited set of triaxial experiments (Section 5) suggests that an effective-stress formulation, or yield function, which is ellipsoidal in shape (when described in stress space) can be applied to ATJ-S graphite within the restrictions of deformation theory. However the associated flow rule of classical plasticity is not descriptive of measured behavior. Instead the rule of "constant strain ratios" suggested by Weng (Reference 23) appears to represent the behavior of ATJ-S in proportional loading tests fairly well.

    Further testing is recommended to extend the empirical definition of yield surfaces and flow rule to other multiaxial stress states and to off-axis loading conditions.

2. Triaxial experiments show the effects of load-path (stress history) on strains at a given stress state to be significant (Section 5.5).

3. Additional biaxial tension tests, using non-proportional load paths, corroborate the existence of biaxial softening and show that incremental Poisson's ratios can be negative for ATJ-S graphite (Section 6).

120

4. Limited evidence (Section 6) suggests that biaxial softening phenomena may also occur in compression. Further testing under better controlled loading conditions is recommended.

REFERENCES

1. J. Jortner, Biaxial Mechanical Properties of ATJ-S Graphite, Final Report under AF Contract F04701-068-C-0288, Change Order 15, McDonnell Douglas Report No. MDC G2072, December 1970.

2. J. Jortner, Multiaxial Behavior of ATJ-S Graphite, Interim Report, AFML-TR-71-160, July 1971.

3. J. Jortner, Multiaxial Behavior of ATJ-S Graphite, Final Report, AFML-TR-71-253, December 1971.

4. J. Jortner, Uniaxial and Biaxial Stress-Strain Data for ATJ-S Graphite at Room Temperature, McDonnell Douglas Report No. MDC G3564, June 1972.

5. H. S. Starrett, Mechanical Properties of Two Billets of ATJ-S (WS) Graphite, U.S. Air Force Report AFML-TR-73-14, Vol. II, May 1973.

6. J. Jortner, et al, "Biaxial Testing", Section 3.1.2 of SAMSO-TR-70-248, Vol. II, Part A, Final Report-Hardening Composites, Refractories, and Transpiration Cooling (RESEP II), by Fred Clayton, et al, August 1970.

7. C. D. Pears and H. Stuart Starrett, An Experimental Study of the Weibull Volume Theory, U.S. Air Force Report AFML-TR-66-228, June 1966.

8. C. D. Pears, personal conversation, November 1972.

9. H. Stuart Starrett and C. D. Pears, A Study of Notches in Brittle Materials by Relating Stress Intensification and Volume, U.S. Air Force Report AFML-TR-67-254, November 1967.

10. J. D. Buch, "The Mechanical Properties of Graphites and Their Relations to a Physically-Based Statistical Theory of Fracture," in Proceedings of the Conference on Continuum Aspects of Graphite Design, USAEC Publication CONF-701105, February 1972.

11. G. T. Yahr and R. S. Valachovic, "Geometrical Parameters Affecting the Fracture Toughness of Graphite," in Proceedings of the Conference on Continuum Aspects of Graphite Design, USAEC Publication CONF-701105, February 1972.

12. G. T. Yahr, "An Examination of the Fracture Behavior of Graphite Through the Use of Splitting Tensile Tests," pp 29-47 in Proceedings of the Conference on Graphite Structures for Nuclear Reactors, London, March 7-9, 1972.

13. C. D. Pears, "Macrostructure-Property Relationships of Polygraphites," Plenary Lecture at the Eleventh Biennial Conference on Carbon, Gatlinburg, Tennessee, June 6, 1973.

14. J. G. Merkle, A Review of Some of the Existing Stress Intensity Factor Solutions for Part-Through Surface Cracks, Oak Ridge National Laboratory, Report No. ORNL-TM-3983, January 1973.

Preceding page blank

15. R. M. Jones and J. G. Crose, SAAS-II-Finite Element Analysis of Axisymmetric Solids, Air Force Report No. SAMSO-TR-68-455, September 1968.

16. K. R. King, et al, Thermal Stress Behavior of Polycrystalline Graphite, U.S. Air Force Report AFML-TR-71-152, Part 1, July 1971.

17. F. C. Weiler and D. A. Rodriguez, Advanced Methods of Anisotropic, Elastic-Plastic Thermal Stress Analysis for Bodies of Revolution, Chapter III of U.S. Air Force Report AFML-TR-70-133, Part I, August 1970.

18. R. Hill, The Mathematical Theory of Plasticity, Oxford, 1950.

19. I. S. Sokolnikoff, Mathematical Theory of Elasticity, 2nd Edition, McGraw-Hill, 1956.

20. J. G. Merkle, An Ellipsoidal Yield Function for Materials that Can Both Dilate and Compact Inelastically, Nuclear Engineering and Design, Vol. 12, pp. 425-451, 1970.

21. F. A. McClintock, "Relations Between Stress and Plastic Strain," Chapter 7 in Mechanical Behavior of Materials, edited by McClintock and Argon, Addison-Wesley, 1966.

22. T. Chu, Plastic Behavior of Composites and Porous Materials Under Isotropic Stresses, PhD Thesis, University of Pennsylvania, 1967.

23. T. Weng, "Stress-Strain Properties of ATJ Graphite Under Combined Stresses," in Proceedings of the Conference on Continuum Aspects of Graphite Design, USAEC Technical Information Center Publication CONF-701105, February 1972.

24. C. D. Pears, Personal conversation, June 1973.

25. U.S. Air Force Report, SAMSO-TR-73-144, Section V, Graphite Proof Strain Program, Philco-Ford, February 1973.

26. E. J. Seldin, Stress-Strain Properties of Polycrystalline Graphites in Tension and Compression at Room Temperature, Carbon, Vol 4, pages 177-191, 1966.

27. W. L. Greenstreet, et al, The Mechanical Behavior of Artificial Graphites as Portrayed by Uniaxial Tests, Carbon, Vol 8, pages 649-663, 1970.

28. W. L. Greenstreet and A. Phillips, A Theory of an Elastic-Plastic Continuum with Special Emphasis to Artificial Graphite, Acta Mechanica, Vol. 16, pp. 143-156 (1973).

29. R. E. Peterson, Stress Concentration Design Factors, J. Wiley & Sons, 1953.